TIN HALIDE PEROVSKITES: COMPUTATIONAL MODELING OF STRUCTURAL, ELECTRONIC AND THERMODYNAMIC PROPERTIES TOWARDS SOLAR CELL APPLICATIONS

Catherine Paschal

A Dissertation Submitted in Partial Fulfillment of the Requirements for the Degree of Doctor of Philosophy in Materials Science and Engineering of the Nelson Mandela African Institution of Science and Technology

Arusha, Tanzania

July, 2021

ABSTRACT

In the photovoltaic field, significant attention has been drawn to lead organo-halide perovskite materials because of their higher ability to convert sun energy to electricity and relatively simple process of fabrication as compared to silicon materials. Among the issues which hinder the lead perovskites solar cells (PSCs) application, are lead toxicity and instability of the PSCs in presence of moisture and light. The tin perovskites are thought over as the foremost fitting substitute due to their comparable chemical nature and high-power conversion efficiency. In this work, the methylammonium tin iodide $CH_3NH_3SnI_3$ ($MASnI_3$) and guanidinium tin halides $C(NH_2)_3SnX_3$ ($GUASnX_3$), X = Cl, Br, I, are considered; the electronic, structural as well as thermodynamic properties of the perovskites' orthorhombic phase (O-phase) have been investigated using various theoretical DFT approaches. For the $MASnI_3$, a direct band gap has been proved; in gamma symmetrical point of the band structure, the band gap value E_g is computed using three different exchange-correlation (XC) functionals: LDA 0.46 eV, PBEsol 0.98 eV and for PBE 1.12 eV; the best result has been obtained with the PBE which follows from the comparison of the computed E_g and lattice parameters with available experimental data. The enthalpy of the decomposition reaction of the $MASnI_3$ into the solid-state materials, SnI_2 and CH_3NH_3I, with reaction enthalpy, $\Delta_r H°(0\ K) = 37$ kJ mol^{-1}, and enthalpy of formation $\Delta_f H°(CH_3NH_3SnI_3, 0\ K) = -390$ kJ mol^{-1}, have been evaluated showing the stability of the O-phase perovskite at low temperature. For the guanidinium-tin perovskites $GUASnX_3$, the lattice parameters are optimized using the GGA-PBE functional. Computations of the materials' band structures was carried out, and band gaps at the gamma symmetry points were obtained: 3.00, 2.47 and 1.78 eV for the $C(NH_2)_3SnCl_3$, $C(NH_2)_3SnBr_3$ and $C(NH_2)_3SnI_3$, respectively. The projected state densities are visualized, and the s-and p-states contribution of the halogens and tin to valence and conduction bands of the perovskites assessed. For the $GUASnX_3$ compounds, the thermodynamic stability to different decomposition routes is examined, the standard enthalpies of formation are obtained: –673 ($GUASnCl_3$), –541 ($GUASnBr_3$), and –401 kJ mol^{-1} ($GUASnI_3$). The interface between the hole transport material Cu_2O and perovskite $MASnI_3$ has been built and analyzed; the predicted binding energy shows strong binding between the two layers.

Keywords: Tin perovskite, orthorhombic, Brillouin zone, Quantum Espresso, k-points, LDA, PBE, PBEsol, Enthalpy of formation, Guanidinium, lead-free, density of states, band gap, interface, binding energy.

DECLARATION

I, Catherine Paschal do hereby declare to the Senate of The Nelson Mandela African Institution of Science and Technology that this dissertation is my original work and that it has neither been submitted nor being concurrently submitted for degree award in any other institution.

Catherine Paschal

Name and Signature of candidate

30.07.2021

Date

The above declaration is confirmed by

Prof. Alexander M. Pogrebnoi

Name and Signature of supervisor 1

30.07.2021

Date

Prof. Tatiana Pogrebnaya

Name and Signature of supervisor 2

30.07.2021

Date

COPYRIGHT

CERTIFICATION

The undersigned certify that they have read and hereby recommend for examination by The Nelson Mandela African Institution of Science and Technology a dissertation/thesis entitled: Tin Halide Perovskites: Computational Modeling of Structural, Electronic and Thermodynamic Properties Towards Solar Cell Applications, in (partial) fulfilment of the requirements for the degree of Doctor of Philosophy in Materials Science and Engineering (Energy Materials) of The Nelson Mandela African Institution of Science and Technology.

Prof. Alexander M. Pogrebnoi

30.07.2021

Name and Signature of supervisor 1

Date

Prof. Tatiana Pogrebnaya

30.07.2021

Name and Signature of supervisor 2

Date

ACKNOWLEDGEMENTS

I would like to express my appreciation for the unlimited support of my supervisors, namely, Prof. Alexander Pogrebnoi and Prof. Tatiana Pogrebnaya. Special thanks to my course instructors: Prof. Tatiana Pogrebnaya, Prof. Alexander Pogrebnoi, Prof. Askwar Hilonga, Dr. Thomas Kivevele and others for laying the foundations of my research work, although it was difficult, this heavy weighted burden was never abandoned. I would also like to outspread my sincere thanks to the academic staff in the Department of Materials, Energy Science and Engineering and my classmates. May Almighty God, with his eyes of love, always look at you.

I extend my sincere appreciation to Mwenge Catholic University for giving me a three years study leave, the African Development Bank (AfDB) for funding my studies, and the Nelson Mandela African Institution of Science and Technology (NM-AIST) for hosting me and offering me a room throughout my studies to use whatever resources available. I am also grateful to Prof. Revocatus Machunda, the Dean of MEWES, who did not hesitate to support me on matters relating to the approval of funds that were required to complete my study.

DEDICATION

This work is dedicated to my:

Family

Friends

TABLE OF CONTENTS

LIST OF TABLES

LIST OF FIGURES

LIST OF APPENDICES

LIST OF ABBREVIATIONS AND SYMBOLS

CB	Conduction Band
CIGS	Copper Indium Gallium Selenide
CIPDF	Cycle-Induced Perovskite Device Fatigue
CuSCN	Copper (I) thiocyanate
CdTe	Cadmium Telluride
DFT	Density Functional Theory
DSSCs	Dye Sensitized Solar Cells
EIA	U.S. Energy Information Administration
ESPRESSO	opEn Source Package for Research in Electronic Structure, Simulation and Optimization
ETL	Electron Transport Layer
ETM	Electron Transport Material
FAI	Formamidinium Iodide
GGA	Generalized Gradient Approximation
GUA	Guanidinium
HTL	Hole Transport Layer
HTM	Hole Transport Material
LDA	Local Density Aproximation
MAI	Methylammonium Iodide
MD	Molecular Dynamics
NREL	National Renewable Energy Laboratory
PBE	Perdew, Burke and Ernzerhof
PBEsol	Perdew-Burke-Ernzerhof revised for solids
PCE	Power Conversion Efficiency
PDOS	Projected Density of States
PSC	Perovskite Solar Cell
PTAA	poly(triarylamine) or Poly[bis(4-phenyl)(2,4,6-trimethylphenyl) amine
PV	Photo-Voltaic
spiro-MeOTAD	2,2′,7,7′-tetrakis(N,N′-di-p-methoxyphenylamine)-9,9′-spirobifluorene
UV	Ultra Violet

VB	Valence Band
XCrySDen	X-window CRYstalline Structures and DENsities
k	wavevector in the first Brillouin zone
q	general wavevector [q = k+G]
$E_{xc}(n)$	exchange-correlation energy in Kohn-Sham theory
$V_{xc}(r)$	exchange-correlation potential in Kohn-Sham theory
$V_{xc}^{\sigma}(r)$	exchange-correlation potential for spin σ
$V_{eff}^{\sigma}(r)$	effective potential for spin σ
$\varepsilon_i^{\sigma}(r)$	independent particle eigenvalue for spin σ
$\psi_i^{\sigma}(r)$	independent particle wavefunction for spin σ
f_i^{σ}	the occupation of state *i* for spin σ
n(r)	density of electrons
$n^{\sigma}(r)$	density of electrons for spin σ

CHAPTER ONE

INTRODUCTION

1.1 Background of the problem

Population growth has always been a challenge to meet sufficient energy production. With the ongoing concerns about global warming and climate change due to the high emission of greenhouse gases like methane and carbon dioxide, the need to shift from the current energy sources to the cleaner ones is of most choice. Renewable energy sources development is expected to satisfy the concerns raised. The production of energy using renewable resources is growing very fast to address the environmental pollution issues. However, the market share is still dominated by the use of non-renewable resources especially fossil fuels due to the prohibitive costs of renewables (U.S. Energy Information Administration [EIA], 2020). The generation of electricity from fossil fuels and renewables are competitive due to lower fossil fuels prices and declining costs of renewable capacity. The energy from the sun among all the available energy resources seems to be the only viable source for supplying all the energy required by the growing population in the coming years (EIA, 2020). The contribution of PV in reducing the global CO_2 emissions is 2.2% of the energy-related emissions and about 5.3% of those related to electricity (Bowen *et al.*, 2020; IEA, 2020). Fig. 1 summarizes the renewable energy projection to 2050 which is expected to reach 38%, as a twice increase from the renewables developed in 2019 (19%).

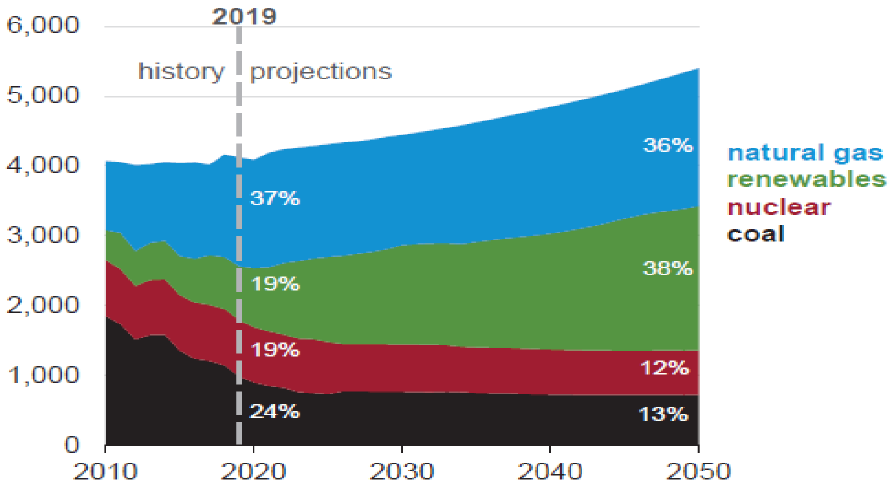

Figure 1: Projection of electricity generation from selected fuels in billion kilowatt-hours (EIA, 2020)

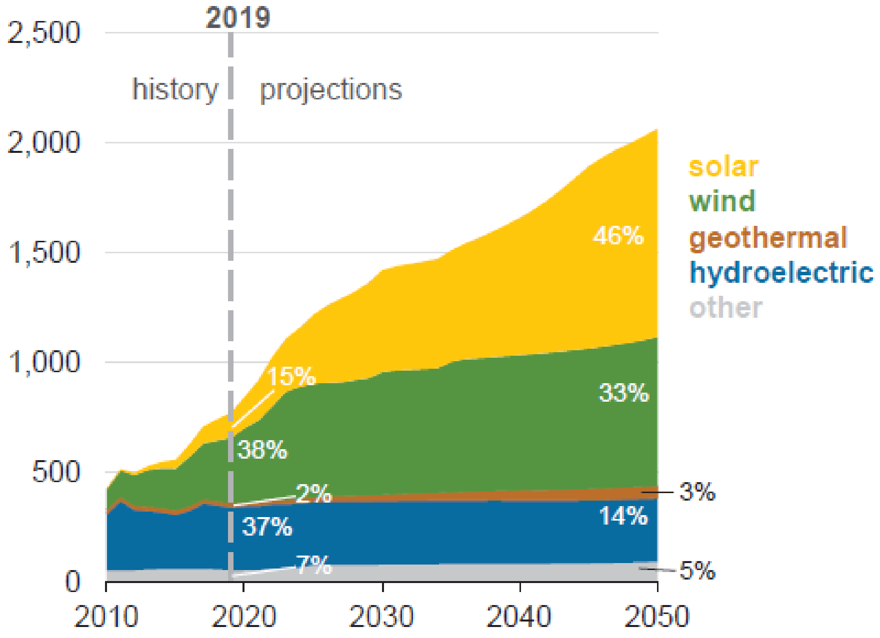

Figure 2: Projection of renewable electricity generation, including end-use in kilowatt-hours (EIA, 2020)

According to the international energy, agency PV contributes about 3.0% of the total electricity demand worldwide (IEA, 2020). As it is illustrated in Fig. 2, the prediction shows that by 2050 solar energy will lead the other renewables in electricity generation. The PV market is mostly dominated by silicon solar cells (monocrystalline and polycrystalline) as well as the CdTe and CIGS (thin films). These two technologies of solar cells suffer from high cost and scarcity of materials for the cells production and maintenance as the materials have been extracted from their ores since 1900 (Jean *et al.*, 2015). Highly light-absorbing and more abundant materials may alleviate the problems associated with cost and availability. The third generation solar cells like the emerging dye sensitized and hybrid perovskites have been widely investigated. Several dyes have been investigated for use as absorber materials (Costa *et al.*, 2021; Makoye *et al.*, 2019; Madili *et al.*, 2018; Deogratias *et al.*, 2019). The power conversion efficiency (PCE) of DSSC have reached 13% in 2020 (NREL, 2020). The perovskites have been found to achieve a high PCE of more than 25% (NREL, 2020), they are cheap to produce and simple to maintain (Korshunova *et al.*, 2016).

1.1.1 Perovskite Materials

Perovskite is the appropriate name of the inorganic mineral calcium titanate $CaTiO_3$ which was identified by Gustav Rose for the first time in 1839 and then coined after Russian mineralogist Lev Alekseyevich Perovski (Navrotsky & Weidner, 1989; Rose, 1839). It should also be noted that in the photovoltaic community, perovskites emerged at first as sensitizers in replacing the liquid dyes in DSSCs and managed to have 15–20 times higher absorption coefficient (Kojima *et al.*, 2009). Perovskite or perovskite-related structures can be found in a wide range of materials, hence the term generally indicates crystals with a typical structure.

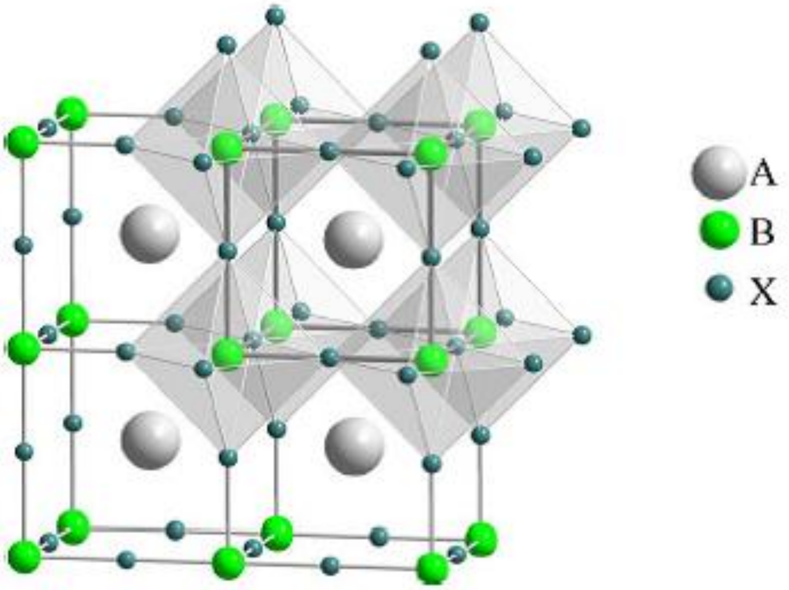

Figure 3: Typical example of a perovskite material crystal structure (Borriello *et al.*, 2008)

In the crystal structure of a perovskite (Fig. 3), X is a halide anion such as Cl, Br and I; A and B are cations of different types; B refers to a metal cation with a coordination number of 6 such as Pb, Sn, Ge and A can be Cs, MA, FA, GUA or other molecules greater than B. The volume which can be occupied by the A ion in the structure is determined by the size as well as the electronegativity of the X and B ions. The perovskite structure can be found mostly in the oxide form, although different types of ternary compounds, like halides, or more complicated species also contain these structures in which, one or more ions are substituted by ligands or molecular cations (Shi *et al.*, 2017). The oxide perovskites have widely been investigated due to many thrilling properties like superconductivity, magnetoresistance and ferroelectricity (Tejuca & Fierro, 1992) while the halide perovskites have been investigated mostly for applications in the photovoltaic field.

However, there are two important factors necessary to determine the ability of a material to form a perovskite as presented by Equations 1 and 2, where r_A, r_B and r_X are the radii of the ions, A, B, and X forming the perovskite. Firstly, the Goldschmidt tolerance factor t is considered which is defined as the ratio between the distance of the A and X ions to that of B and X ions (Goldschmidt, 1927; Park, 2015). The factor *t* should be in the range from 0.8 to 1.0 for the formation of a well-established perovskite structure. The lower range results in a distorted perovskite structure due to the BX_6 octahedral tilting and symmetry lowering hence the formation of other structures (Mitzi *et al.*, 2001; Travis *et al.*, 2016).

$$t = \frac{r_A + \mathrm{r}_X}{\sqrt{2(r_B + r_X)}} \tag{1}$$

Secondly, the octahedral factor μ is also considered and can be defined as the ratio between the ionic radius of the B and X ions (Li *et al.*, 2008; Park, 2015) as follows:

$$\mu = \frac{\mathrm{r}_B}{\mathrm{r}_X} \tag{2}$$

A perovskite solar cell seems to work better than silicon cells and this can be the solution to high-efficiency solar power (Navrotsky & Weidner, 1989). The high ability of perovskite solar cells to absorb light across almost all visible wavelengths has made them the new star of the PV industry (Shi *et al.*, 2017). Also, these cells have exceptional PCEs and the comparatively simple process of fabrication; they are cheap, somehow easy to produce as well as very flexible in their applications. Methylammonium (MA) lead iodide has been the most interesting among the organo-halides. It has been found to have high carrier mobility, low exciton binding energy, high carrier diffusion length (~100 nm), a large absorption coefficient of 10^4–10^5 cm^{-1} at 600 nm (Laban & Etgar, 2013), and a direct band gap of approximately 1.6 eV (Ogomi *et al.*, 2014; Stoumpos *et al.*, 2013). It has a negative enthalpy of formation as predicted by DFT calculations (Buin *et al.*, 2015; Zhang *et al.*, 2018). The perovskite solar cell efficiency at converting light into electricity has grown faster than that of any other material; from under 4% in 2009 to over 22.7% in 2017 (Hoefler *et al.*, 2017; Jiang et al., 2018; Ono & Qi, 2018).

There is a number of obstacles that are still prevailing to the perovskites before they can turn out to be a viable substitute for conventional PV technologies. Among these is the tendency of the lifetime of perovskite solar cells to depreciate quickly in presence of moisture and light (Baranwal *et al.*, 2017). Whereas a silicon cell lasts for 25 years, a typical high-efficiency perovskite solar cell, when not encapsulated, can last for a few months. Another drawback is the lead toxicity of the methylammonium lead halides. Alternatives to Pb, like Sb, Bi, Cu, Ge, and Sn, have been studied and they have lower efficiencies (Jiang *et al.*, 2018; Zhao *et* *al.*, 2017). Moreover, the instability issue of the separately deposited layers, typically the HTMs like the Spiro-MeOTAD is another challenge on the efforts to the commercialization of PSCs (Berhe *et al.*, 2016).

1.2 Statement of the Problem

Hybrid perovskite solar cells have grown in efficiency dramatically since their inception (Kojima *et al.*, 2009; NREL, 2020). While efficiency could be improved further, there are numerous concerns about the stability of these solar cells and the toxicity of lead (Korshunova *et al.*, 2016; Slavney *et al.*, 2017) that must be addressed before they can be commercialized. This is directly related to device physics, because the routes to the decomposition of the perovskites can limit their PCE as the defects can act as sites for environmental elements to diffuse and react with the perovskite, causing severe degradation. Many theoretical methods have also been devoted to the study of $CH_3NH_3SnI_3$ perovskite, and the mechanism of energy conversion in perovskite-based solar cells has been partially explained (Agiorgousis *et al.*, 2014; Frost *et al.*, 2014; Lang *et al.*, 2014; Mosconi *et al.*, 2013; Umari *et al.*, 2014). Consulting the literature, for methylammonium or guanidinium perovskites, no experimental or theoretical data on related reactions are known to the best of our knowledge. There are, however, very few papers on the $CH_3NH_3SnI_3$ perovskite/HTM interface theoretical research (Haider *et al.*, 2020; Jayan & Sebastian, 2021; Lazemi *et al.*, 2018; Obila *et al.*, 2021).

This study examines the structural, electronic and thermodynamic properties of methylammonium and guanidinium tin halide perovskites for the sake of replacing lead and proposing a new material for solar cells. The study also explores the interface of the methylammonium tin iodide with Cu_2O as a hole transport material for efficient generation of charges, charge extraction, and transport of charges with minimal interlayer recombination as a means of replacing lead metal and enhancing perovskite stability.

1.3 Rationale of the Study

The majority of solar cells currently are produced using silicon that has maintained efficiency of less than 15% for over 20 years. However, crystalline silicon is expensive in terms of its processing costs. So, there is a need to find new materials to enhance the performance of solar cells. Perovskites exhibit a promising solution but the challenges of degradation should be solved and replacement of the toxic lead should be suggested. Tin has shown good characteristics similar to lead which suggests its ability to replace lead and solve the toxicity problem.

1.4 Research Objectives

1.4.1 General Objective

To design and characterize the structure, performance and stability of tin halide perovskite materials by using a quantum chemical approach.

1.4.2 Specific Objectives

(i) To determine the structural, electronic and thermodynamic properties of methylammonium tin iodide perovskite.

(ii) To study the interfacial interactions between the perovskite materials and transport materials to enhance their performance.

(iii) Engineering of the $MASnX_3$ (X = Cl, Br, I) through the replacement of the MA-cation with GUA-cation and determination of the electronic, structural, and thermodynamic properties.

1.5 Research Questions

(i) What are the structural, electronic and thermodynamic properties of $MASnI_3$ as compared to $MAPbI_3$?

(ii) How are the properties of $MASnI_3$ affected at the interface? How is the binding energy affected when a HTM material interacts with the $MASnI_3$ perovskite?

(iii) How are the electronic, structural, and thermodynamic properties affected by the substitution of the MA-cation with GUA-cation?

1.6 Significance of the Study

The sun provides more than enough energy to meet the whole world’s energy needs. If good absorber materials like the perovskites can be manufactured and commercialized, they can absorb this energy and convert it to electricity, a way forward to solve the problem of power. No greenhouse gas emissions are released into the atmosphere when you use solar panels to create electricity. Once the toxic lead has been replaced, the environment and people health can be safe. When compared to other forms of power generation, the operational costs of solar panels are quite low after they have been installed. Since no fuel is needed, solar power can generate large quantities of electricity without incurring additional costs after installation, as opposed to fossil fuels.

1.7 Delineation of the Study

This study is about tin halide perovskites and focuses on the tin as the main replacement of lead in lead perovskite solar cells; the structural, electronic and thermodynamic properties are investigated. Another replacement is done on the MA-cation with GUA-cation to understand the effectiveness of a larger organic-inorganic cation to the tin perovskite as a way to enhance the solar cell PCE as well as stability. The interface characteristics of the perovskites with their transport materials have also been explored by considering their binding energy variations.

CHAPTER TWO

LITERATURE REVIEW

2.1 Perovskite Structure

Research findings show that perovskite materials tend to have different phases (crystal structures) depending on temperature. At temperatures lower than 100 K, the perovskite material has been found to display an orthorhombic (γ) phase which is stable. When the temperature increases to 160 K, there is the appearance of a tetragonal (β) phase which tends to replace the previous orthorhombic (γ) phase. When the temperature keeps increasing further to about 330 K and above, the tetragonal (β) phase starts to be replaced by a more stable cubic (∝) phase (Shi & Jayatissa, 2018). The geometry of the three phases of the hybrid organic-metal perovskite is illustrated in Fig. 4.

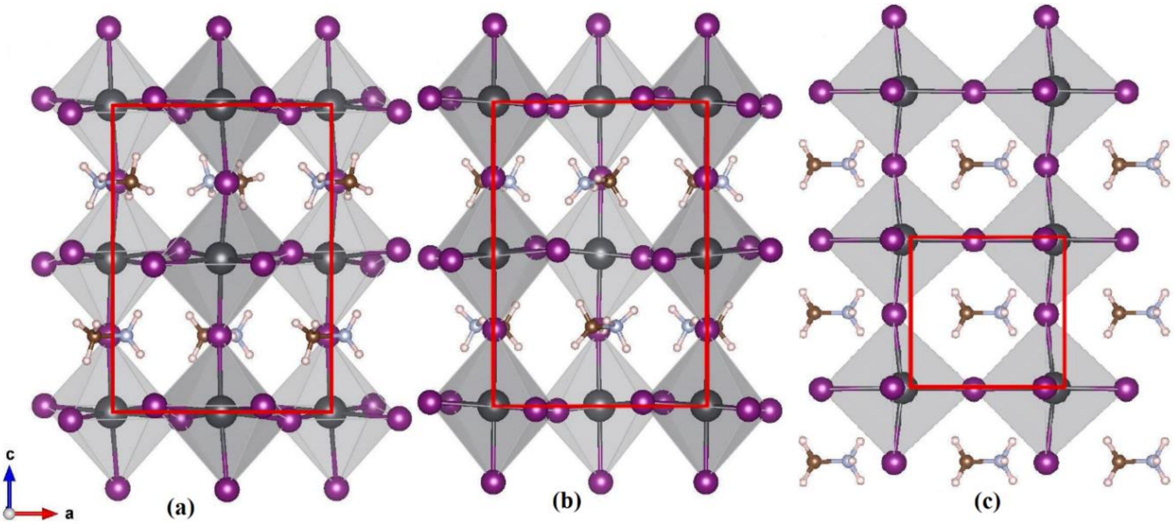

Figure 4: Three perovskite phases: (a) orthorhombic, (b) tetragonal and (c) cubic (Korshunova *et al.*, 2016)

2.2 Classification of Perovskite Solar Cells

Perovskite solar cells have been classified based on electrical properties (conducting or non-conducting), charge carriers (p- or n-type) and morphology (mesoporous or flat thin films) which offer the perovskites a wider variety than any other category of solar cells (Fakharuddin *et al.*, 2016). Figure 5 illustrates the classification of the perovskite solar cells' architectures. Under all these designs perovskite solar cells can be produced as; the normal or regular p-n type and the planar type; the latter is either conventional planar (n-i-p) as illustrated in Fig. 5 (b) or inverted planar (p-i-n) cell in Fig. 5 (c). The first type, conventional planar structured perovskite device can also be divided into two; the mesoporous and meso-superstructure as seen in Fig. 5 (a) and (d) (Mali & Hong, 2016). The mesoscopic n-type TiO_2 film can be deposited on a conductive glass coated with a compact TiO_2 layer forming a hybrid perovskite with high power conversion efficiency. The TiO_2 acts as an electron transport layer (ETL) forming about 100-200 nm porous thick film which helps in blocking the holes. A perovskite absorber layer accounts for about 200-250 nm layer above the ETL. Another thin layer of hole transport material (HTM) like Spiro-MeOTAD, CuSCN, PTAA or Cu_2O is then deposited above the perovskite to block the electrons and provide selectivity for the holes.

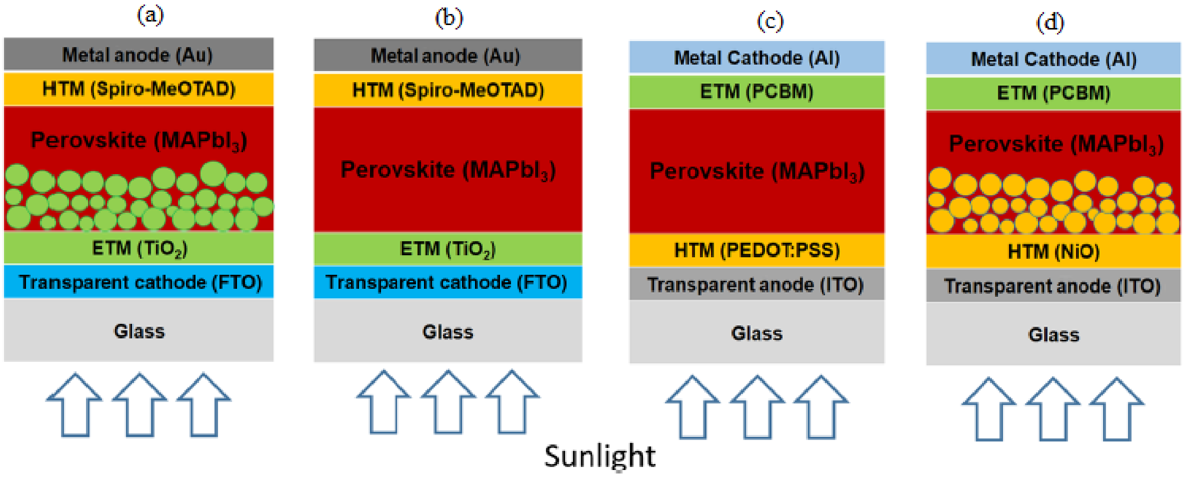

Figure 5: Perovskite solar cells device architectures: (a) n-i-p mesoscopic, (b) n-i-p planar, (c) p-i-n planar, and (d) p-i-n mesoscopic (Mali & Hong, 2016)

2.3 Components of a Perovskite Solar Cell

2.3.1 The Blocking Layer

This is usually a metal oxide directly deposited onto the conducting glass substrate forming a compact continuous n-type contact serving the purpose of providing electron selectivity to slow down the recombination between the holes in the perovskite and the electrons deposited on the conductive oxide layer. The TiO_2 is mostly chosen as a blocking layer which is usually deposited by aerosol spray pyrolysis, through spin-coated precursor sintering or atomic layer deposition method (Kavan *et al.*, 2014; Ke *et al.*, 2015; Wu *et al.*, 2014). This layer is also known as the ETL. Another blocking layer is SnO_2 which has shown excellent results with open-circuit voltages over 1200 mV and appreciable power conversion efficiency above 21% (Anaraki *et al.*, 2016; Baena *et al.*, 2015). In Fig. 6 (a) and (b), the blocking layer is that containing compact TiO_2 as shown in light-grey colour.

2.3.2 The Mesoscopic Scaffold

This is a thin layer deposited on top of the blocking layer and is usually made of nanoparticles of metal oxide. It provides a high contact area for the injection of electrons before the recombination. The material which has been used historically as a mesoporous substrate is TiO_2 semiconductor with a band gap of 3.2 eV which gives an ability to absorb only in the ultraviolet region of the spectrum (O'Regan & Grätzel, 1991). In Fig. 6 (a), the mesoscopic scaffold is represented by the mesoporous TiO_2 layer. Titanium oxide is non-toxic as well as cheap compared to other materials of the same characteristics like ZrO_2. The anatase phase of TiO_2 is mostly preferred in perovskites because it performs better than the other phases by allowing higher power conversion efficiencies (Kavan *et al.*, 2014).

2.3.3 The Absorber Layer

The perovskite itself acts as the absorber layer responsible for photons absorption and the generation of free charges, it is usually photo-active in the visible region of the solar spectrum. The perovskite material acts as the absorber layer in all designs of perovskite solar cells. As it is seen in Fig. 6 (a) and (b), the layer with the perovskite is the absorber layer. There are other two outer layers in the perovskite solar cell architecture, the metal-electrode (in this case Au) and FTO layers. The Au electrode plays part in collecting the holes that have been transferred to the HTM, and the FTO is a conductive layer that receives the electrons generated by light irradiated on the perovskite absorbing material. The two outer layers are connected and current flows in the outer circuit.

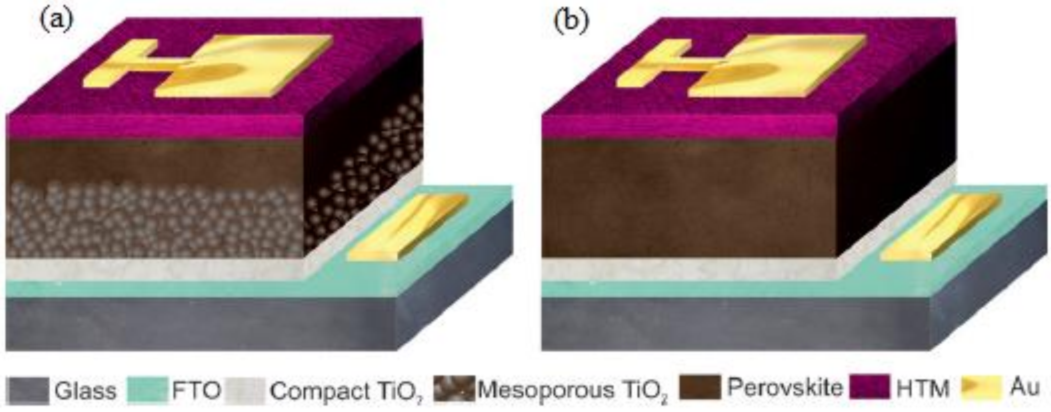

Figure 6: The architecture of heterojunction perovskite solar cells: (a) mesoscopic and (b) planar (Calio *et al.*, 2016)

2.4 Transport Materials for Perovskite Solar Cells

The PSCs durability can be governed by several factors one being the charge transport materials, ETMs and HTMs. Some transport materials are not good under certain conditions of exposure to UV light, moisture, or temperature as their stability is directly affected and can later affect the durability of the cell. The necessities for ideal charge transport materials suitable for solar cells involve a low surface recombination rate, a suitable energy level and high conductivity (Wang *et al.*, 2020). However, the stability of the PSC is strongly influenced by the choice of the ETM and HTM (Divitini *et al.*, 2016; Ono & Qi, 2018).

2.4.1 Electron Transport Materials

The electron transport layer in PSCs plays an important role in extracting and transporting the electrons generated by sunlight on the perovskite layer to the cathode of the cell to prevent recombination at the interface of the ETL and absorber layer. Many ternary metal oxides have attunable electrical and optical properties which is a potential for ETLs especially in planar PSCs (Thambidurai *et al.*, 2020). Titanium oxide is among the widely utilized ETM for PSCs which can be affected by UV light irradiation by creating oxygen vacancies which reduce the stability of the material (Leijtens *et al.*, 2013). The PSCs with TiO_2 as ETM perform very well in terms of PCE but the big problem is its effects when exposed to UV light as well as poor electron mobility that is why other ETMs have been developed to replace it without weakening the high performance (Dong *et al.*, 2014; Liang *et al.*, 2017; Liu *et al.*, 2018; Shin *et al.*, 2015; Zhu *et al.*, 2016). Other oxides like Al_2O_3, ZnO, $SrTiO_3$, SnO_2, Zn_2SnO_4, ZrO_2, $BaSnO_3$ have been used as ETMs for PSCs (Bera *et al.*, 2014; Bi *et al.*, 2013; Carnie *et al.*, 2013; Jiang *et al.*, 2018; Mali *et al.*, 2015; Oh *et al.*, 2014; Shin *et al.*, 2015; Zhang *et al.*, 2009). The efficiency of PSCs increased from 6.6% to 7.5% when Al_2O_3 was used to passivate TiO_2 (Ogomi *et al.*, 2014). With the use of Cs_2CO_3 for surface modification, the PSCs efficiency increased to 14.2% which minimized back recombination in the cells (Dong *et al.*, 2014). The SnO_2 has shown a high PCE of more than 20% when used as ETM in PSCs due to its high charge mobility (electron mobility) as high as 412 $cm^2\ V^{-1}\ S^{-1}$ (1 $cm^2\ V^{-1}\ S^{-1}$ for TiO_2) as well as possession of a proper band gap with good alignment to the perovskite (Jia *et al.*, 2020; Zhu *et al.*, 2020).

2.4.2 Hole Transport Materials

Hole transport materials are responsible for the transportation of charge and improving the stability of PSCs due to the possession of proper energy levels and having high charge carrier mobility. There are two common classes of hole transport materials in PSCs; organic and inorganic. The inorganic HTMs have become more common than organic because of their low cost and stability.

Spiro-MeOTAD (2,2',7,7'-tetrakis-(N, N-di-4-methoxyphenylamino)-9,9'-spirobifluorene) has frequently been used as HTM for testing PSCs due to its simplistic implementation with high performance. Similarly, Spiro-MeOTAD has been used in other applications besides solar cells due to its desirable properties. However, Spiro-MeOTAD is under debate regarding its cost-performance, long-term stability, temperature degradation issues, the quality of the film, coating technologies compatibility, and hysteresis (see section 2.5.3) (Hawash *et al.*, 2018). Currently, there are more than 30 HTMs that have been investigated to be incorporated in perovskite materials for solar cells in order to replace the Spiro-MeOTAD (Hawash *et al.*, 2018). Examples of the HTMs that have been developed to replace Spiro-MeOTAD include CrO_x, CoO_x, NiO_x, CuSCN, Cu_2O, CuO_x, CuO, PTAA, P3HT, PEDOT:PSS, MoO_x, VO_x and their composites (Hawash *et al.*, 2018; Kung *et al.*, 2018). Table 1 lists the HTMs that have been tested in perovskite solar cells with their respective power conversion efficiencies. The organic and inorganic HTMs are competing in performance where the NiO, MoS_2 and CuO_x HTMs have shown a remarkable performance when compared to the well-known Spiro-MeOTAD HTM, a step forward to its replacement.

Table 1: Hole transport materials for PSCs with their PCE

HTM	Perovskite material	PCE, %	Ref.
Spiro-OMeTAD	$CH_3NH_3PbI_3$	19.71	Ahn *et al.* (2015)
PBDTT-FTTE	$CH_3NH_3PbI_3$	11.6	Gaml *et al.* (2017)
FDT	$FAPbI_3/MAPbBr_3$	20.2	Saliba *et al.* (2016)
P3HT	$CH_3NH_3PbI_3$	15.3	Habisreutinger *et al.* (2014)
PTAA	$(FAPbI_3)_{1-x}(MAPbBr_3)_x$	20.2	Yang *et al.* (2015)
PEDOT:PSS	$CH_3NH_3PbI_3$	18.1	Heo *et al.* (2015)
NiO_x	$CH_3NH_3PbI_3$	17.3	Park *et al.* (2015)
CuSCN	$(FAPbI_3)_{0.85}(MAPbBr_3)_{0.15}$	18	Jung *et al.* (2016)
Cu_2O	$CH_3NH_3PbI_3$	11.03	Yu *et al.* (2016)
CuO_x	$CH_3NH_3PbI_{3-x}Cl_x$	19	Rao *et al.* (2016)
CuO	$CH_3NH_3PbI_3$	12.16	Zuo and Ding (2015)
FBT-Th4/CuO_x	$CH_3NH_3PbI_3$	18.85	Guo *et al.* (2018)
CuS NPs	$CH_3NH_3PbI_3$	>16	Rao *et al.* (2016)
$CuGaO_2$	$CH_3NH_3PbI_{3-x}Cl_x$	18.51	Zhang *et al.* (2017)
MoS_2	$CH_3NH_3PbI_3$	20.43	Kohnehpoushi *et al.* (2018)
NiO	$CH_3NH_3PbI_{3-x}Cl_x$	22	Zhao *et al.* (2018)

2.5 Perovskite Solar Cell Challenges

2.5.1 Lifetime and Instability of Perovskite Solar Cells

Although there is an enormous improvement in the power conversion efficiency of perovskite solar cells, they are still facing issues of stability and lifetime. However, it has been reported that when TiO_2 is employed as an electron transport material there is the emergence of oxygen vacancies in the TiO_2 when there is an exposure of the perovskite device under UV light which is among the causes of instability (Leijtens *et al.*, 2015; Leijtens *et al.*, 2013). The $BaSnO_3$ has recently shown better characteristics over TiO_2 as an electron transport material for PSCs to minimize the issue of stability under UV light (Shin *et al.*, 2017).

Moisture and higher temperature have also been obstacles to the stability of PSCs. Practical applications of solar cells and other devices occur at a temperature up to 80 °C when exposed to light while most studies on long term stability of PSCs are carried out at room temperature.

It has been found that the organic species of the PSCs are affected by moisture where they react with water to produce the halide of hydrogen and the organic-inorganic compound (Pathak *et al.*, 2014; Weerasinghe *et al.*, 2015). Metal oxide transport materials like ZnO as ETL and NiO_x as HTM have shown improved stability under water exposure as compared to the organic transport materials (Fu *et al.*, 2020). However, numerous investigations have concentrated on encapsulation techniques to anticipate UV exposure, oxygen introduction, and moisture entrance (Pathak *et al.*, 2014; Weerasinghe *et al.*, 2015). Every technique has given an incremental change of the stability of the sun-powered cells, some with promising strong qualities of over a year of task (Grancini *et al.*, 2017).

Another obstacle to the PSCs is the continuous dark/light cycle-induced perovskite device fatigue (CIPDF) which induces performance loss whereby the device performance is reduced to less than 50% of its initial efficiency in an open circuit after dark ageing (Fu *et al.*, 2020; Huang *et al.*, 2016). The ionic vacancies, as well as lattice interstitials, are caused by the defects in the PSC layer as a result of the cyclic charge carrier movement. However, studies have shown that the initial efficiency of the PSCs can be recovered or even increased after dark ageing (Anaraki *et al.*, 2016) although the mechanisms of how the dark/light cycle affects their performance and stability are still not yet clear (Fu *et al.*, 2020).

2.5.2 Lead Toxicity and its Replacement

The impressive performance of the PSCs which has attracted the attention of researchers has been achieved by the lead halide perovskites. Human beings and the ecosystem, in general, can be harmed due to the environmental pollution caused by the toxic solution formed when lead compounds dissolves in water. The toxicity issue of lead is well known and has been addressed by several publications (Hailegnaw *et al.*, 2015; Shahbazi & Wang, 2016), and an increasing number of researchers have attempted to find a suitable replacement of lead in PSCs (Hao *et al.*, 2014). The tin (Sn-based) perovskite can be viewed as the most suitable lead replacement due to its similar chemical nature as group 14 metal and has a higher PCE as compared to other replacements. Still, the stability issue of Sn with self-doping has limited the development of Sn-based perovskites (Koh *et al.*, 2015). This calls for the need to study the interfacial characteristic of the lead-free perovskites (Sn-based in particular) in order to develop materials that may replace the toxic lead and still maintain the attractive properties played by the lead perovskites such as producing solar cells with high efficiency.

2.5.3 Hysteresis

Hysteresis of PSCs has received much attention and is related to the processes of interfacial charge transfer. The origin of PSCs hysteresis activity is thought to be a high density of traps at the window/perovskite interface caused by non-radiative recombination (Shao *et al.*, 2014; Snaith *et al.*, 2014). However, the reversible canvassing behaviour found in PSCs cannot be explained by the trap mechanism. Other processes, such as ionic motion, have been suggested by researchers for the cause of hysteresis (Leijtens *et al.*, 2015). Planar perovskite devices have shown higher hysteresis behaviour than the mesoporous one; and also those based on metal oxide transport materials have higher hysteresis compared to those using organic transport materials (Stranks & Snaith, 2015). When considering the inverted PSCs made of organic charge transport materials, hysteresis issue is less common (Heo *et al.*, 2015) and also decreased in the mixed halide PSCs (Zhang *et al.*, 2016). The ion diffusion, defect concentration along self-healing ability of the PSCs are largely affected by the stoichiometric ratios of the materials which lead to hysteresis in the PSCs. Additionally, the morphology of the perovskite material can affect the interface together with the grain boundaries of the perovskite films (Frost & Walsh, 2016). Moreover, the ionic motion inside the PSCs, the ferroelectric polarization and also the bias-dependent traps occurring at the PSCs interfaces have also been considered as hysteresis causing behaviours (Ono & Qi, 2016). The phenomena related to the hysteresis problem has been widely investigated to include ferroelectricity (Fan *et al.*, 2015; Leijtens *et al.*, 2015), ion migration (Miyano *et al.*, 2016) and charge build-up (Tress *et al.*, 2015) although there are no practical guidelines on set to test the PSC devices in order to handle the hysteresis phenomena (Fu *et al.*, 2020). Therefore, it is important to shed light on the structural and electronic properties of perovskite/HTM interfaces to suppress recombination of the interfacial carriers, fasting separation of the carriers and efficient extraction of charges.

2.5.4 Area and Flexibility

In order to obtain PSCs which are flexible and suitable for large areas, materials with low energies of formation in deposition are needed for large-volume manufacturing techniques with low capital expenditure and low production costs (Ye *et al.*, 2016). Photovoltaic devices with a large area can be affected by nonradiative recombination losses which occur at the interior and on the interface as a result of bulk, surface and interfacial defects caused by the introduction of recombination centres resulting in the reduction of the fill factor, short circuit current in addition to open-circuit voltage (Fu *et al.*, 2020). Different fabrication procedures have been developed to address the challenges of large area and flexible devices to include the printing and doctor-blading, spray coating, direct contact intercalation and the electrodeposition method (Williams *et al.*, 2016; Yang *et al.*, 2015).

2.5.5 The Perovskite Solar Cells Interface

Several factors influence the efficiency of PSCs including optical losses, contact energy offsets, recombination of charge carriers together with nonideal transport layers which reduce the open-circuit voltage and the fill factor of the cell (Sha *et al.*, 2015; Sherkar *et al.*, 2017). The surface of a perovskite absorber layer in PSCs is usually covered with the two charge transport layers ETL and the HTL forming an interface. The interface barriers between the electrode, absorber and transport layers are usually treated as secondary problems in PSCs whereas the generation and preservation of charge carriers in the absorber is the primary concern (Zhou *et al.*, 2014). At the interface, there is the so-called nonradiative recombination which severely impacts the performance of the PSCs regarding not only the efficiency but also the hysteresis and stability (Baena *et al.*, 2015; Habisreutinger *et al.*, 2014; Shao *et al.*, 2014; Sherkar *et al.*, 2017).

In open-circuit conditions, losses due to energy-level mismatch, un-intimate contact, or interfacial defects cause high charge accumulation, resulting in a drop in perovskite material performance (Chen *et al.*, 2014). A number of ways have been used to improve the quality of the perovskite interfacial layers to include; compositional engineering (Jeon *et al.*, 2015), interface passivation (Abate *et al.*, 2014), and through other processing methods such as gas-phase coupled with vacuum-assisted deposition but the performance is still low (Hwang *et al.*, 2015). From these observations, there is a need to study the perovskite/HTM interface and do some device engineering such as replacing MA-cation with other cations to improve the performance of lead-free perovskites.

2.6 Theoretical approaches used in crystals’ simulations

2.6.1 Density Functional Theory

The DFT is a quantum mechanical technique used for the determination of atomic and molecular structures and electronic features. It is a phenomenally efficient way to find solutions to a fundamental Schrödinger equation that explains the quantum behaviour of atoms and molecules. For the study of different material properties, DFT uses the electron density of atoms. Since the main chemical features of a material depend on the valence electrons in the external shell, DFT concentrates on the electrons in the external shell. For defining internal and external electron density, DFT uses various functionals (Sholl & Steckel, 2011). In quantum mechanics, the particle's state is defined by its wave function. The Schrödinger equation is a partial differential equation that is used to find the wave function and a particle's energy by solving the time-independent Schrödinger equation.

Two basic math theorems proved by Kohn and Hohenberg and Kohn and Sham deriving from a number of equations in the mid-1960s provide the whole field of density functional theory. The first theorem of Hohenberg and Kohn states that the ground state energy of the system is a special electron density functional. This theorem notes that the mapping of the ground-state wave function and ground-state energy is one to one, as E can be represented by ground-state density E [*n*(r)], in which *n*(r) is an electron density. The time independent equation of Schrödinger is given by:

$$H\Psi = E\Psi \tag{3}$$

With H being the Hamiltonian operator, Ψ stands for the wave function of the system and E is the eigenvalue energy of the stationary state Ψ. Here, the Hamiltonian operator can be expanded as:

$$H = -\frac{\hbar^2}{2m_e}\sum_{i=1}^{N} \nabla_i^2 + \sum_{i=1}^{N} V\,(r_i) + \sum_{i=1}^{N}\sum_{j<i} U(r_i r_j) \tag{4}$$

Equation 4 has three terms with the first term representing the total kinetic energy of all electrons in the system, the second term is the system's potential energy as a result of Coulomb interaction, and the last term defines the interaction energy between one electron and another. The term *V*(r) represents the external potential responsible for the electron-nuclei interaction, m_e stands for the electron's mass.

The electronic density *n*(r) at the ground state wavefunction is also a function of the external potential since the wavefunction is decided by *V*(r) considering the expression:

$$n(r) = \int \Pi_{i=2}^{N} dr_i |\Psi(r, r_2, \ldots, r_N|^2 \tag{5}$$

The external potential and the Hamiltonian can be affected by the ground-state electron density and in this manner, all the ground state system's properties can be obtained. The *n*(r) and *V*(r) functions are obtained self consistently since they are interdependent. Unfortunately, although the first theorem by Hohenberg-Kohn strictly shows that the Schrödinger equation has a functional electron density, the theorem does not tell anything about what is actually functional. The second theorem of Hohenberg-Kohn describes an important functional: "the electron density that reduces the energy in the general functional is the actual electron density that corresponds to Schrödinger's equation complete solution" (Martin, 2020):

$$E[n(r)] > E_0[n_0(r)] \tag{6}$$

However, the energy function can be separated into two parts with one of the parts having a known value and the other unknown:

$$E[\psi_i] = E_{known}[\psi_i] + E_{xc}[\psi_i] \tag{7}$$

Here, the recognized term consists of four terms: electron kinetic energy, electron-electron Coulomb interaction, electron-nuclei Coulomb interaction, and nuclei-nuclei Coulomb interaction. The unknown term is the term for exchange-correlation, which requires and needs to be approximated by purely quantum mechanical effects.

In order to find the system's ground state energy from electron density, the establishment of functional exchange-correlation is needed. It is well known that the functional exits of exchange-correlation, but unfortunately, no one knows the exact functional exchange-correlation, so in order to get the results, different approximations have been established. The local density approximation is one of the simplest exchange-correlation functions (LDA). The local electron density is believed to be that of a homogeneous electron gas in LDA, which is known to describe the functional approximate exchange-correlation. In the case of generalized gradient approximation, both the local electron density and its gradient are known for approximation (GGA). Continuous research is underway so as to enhance this practical exchange-correlation in order to obtain accurate results.

Kohn and Sham provided a series of equations to solve the Schrödinger equation to basically use density functional theory in order to achieve the ground-state electron density in which only one electron is involved in each equation. The Kohn Sham scheme is provided in the form:

$$\left[\frac{-\hbar^2}{2m_e}\nabla_i^2 + V(r) + V_H(r) + V_{xc}(r)\right]\psi_i(r) = \varepsilon_i\psi_i(r) \tag{8}$$

The terms in Equation 8 are defined as the electron's kinetic energy, the external potential *V*(r) between the electron and nuclei, the Hartree potential (V_H), which includes the electron's Coulomb self-interaction with the density of the electrons. Here, the exchange-correlation potential is V_{xc}, which needs to be approximated by practical exchange-correlation.

A series of Kohn sham equations are solved by DFT using a self-consistent scheme. First, any estimated electron density (trial *n*(r)) is guessed, which is used to solve the Kohn sham series of equations in order to obtain a single electron wave function ψ_i(r). It recalculates the electron density, which is *n*(r), from the obtained single electron wave function. The self-consistency in any loop can be found when the "measured" electron density is near enough to the trial electron density and then one can obtain the density of the ground state. Both the structural and electronic properties of the system can be determined after the calculation of the ground-state electron density (Sholl & Steckel, 2011).

In Kohn-Sham DFT, all the exchange and correlation effects are integrated into the functional exchange-correlation $E_{xc}[n]$, which depends on the density *n*(r). The approximations for E_{xc} all require some approach to the use of knowledge extracted from some many-body system. The Generalized Kohn-Sham method offers a basis for theories that explain more than just the ground state. Within this approach, the values of the equations can be properly viewed as energy approximations for adding and removing electrons:

$$H = -\frac{\hbar^2}{2m_e}\sum_i \nabla_i^2 - \sum_{i,\ I}\frac{Z_I e^2}{|r_i - R_I|} + \frac{1}{2}\sum_{i\neq j}\frac{e^2}{|r_i - r_j|} - \sum_I \frac{\hbar^2}{2M_I}\nabla_I^2 + \frac{1}{2}\sum_{I\neq J}\frac{Z_I Z_J e^2}{|R_I - R_J|} \tag{9}$$

The Kohn-Sham solution to the complete interaction of many-body problems is to rewrite the Hohenberg-Kohn expression for ground-state energy functionality in the form:

$$E_{KS} = T_s[n] + \int dr V_{ext}(r)n(r) + E_{Hartree}[n] + E_{II} + E_{XC}\,[n] \tag{10}$$

where T_s is the independent-particle kinetic energy, V_{ext}(r) is the external potential due to the nuclei and other external fields, $E_{Hartree}$ is the Hartree energy, E_{II} is the interaction between the nuclei and E_{XC} is the exchange-correlation energy.

In the flow diagram in Fig. 7, the Kohn-Sham equations are summarized. They are a group of independent particle-equations, such as Schrodinger, which must be resolved if the effective potential $V_{eff}^{\sigma}(r)$ and density n(r,σ) are consistent. The explicit reference to spin is dropped unless necessary and V_{eff} and n are assumed to indicate space (r) and spin (σ) dependences. The true calculation uses a numerical method that adjusts V_{eff} and n successfully in order to reach the solution self-consistently. The computer-intensive step is the 'solve KS equation' for a certain V_{eff} potential. This phase is called a 'black box' that uniquely solves the equations in order to determine an output density n^{out} for a given input V, i.e., $V^{in} \rightarrow n^{out}$. Conversely, as seen in the second box, for a given form of the XC functional, any density n defines a possible V_{eff}. The problem arises as the input and output possibilities and densities do not agree, except for the exact solution. A new potential $n^{out} \rightarrow V^{new}$ is operationally specified to arrive at the solution, which can then start a new cycle with V^{new} as the new potential for input. The progression converges with the proper selection of the new potential in terms of the potential or density detected at the previous stage.

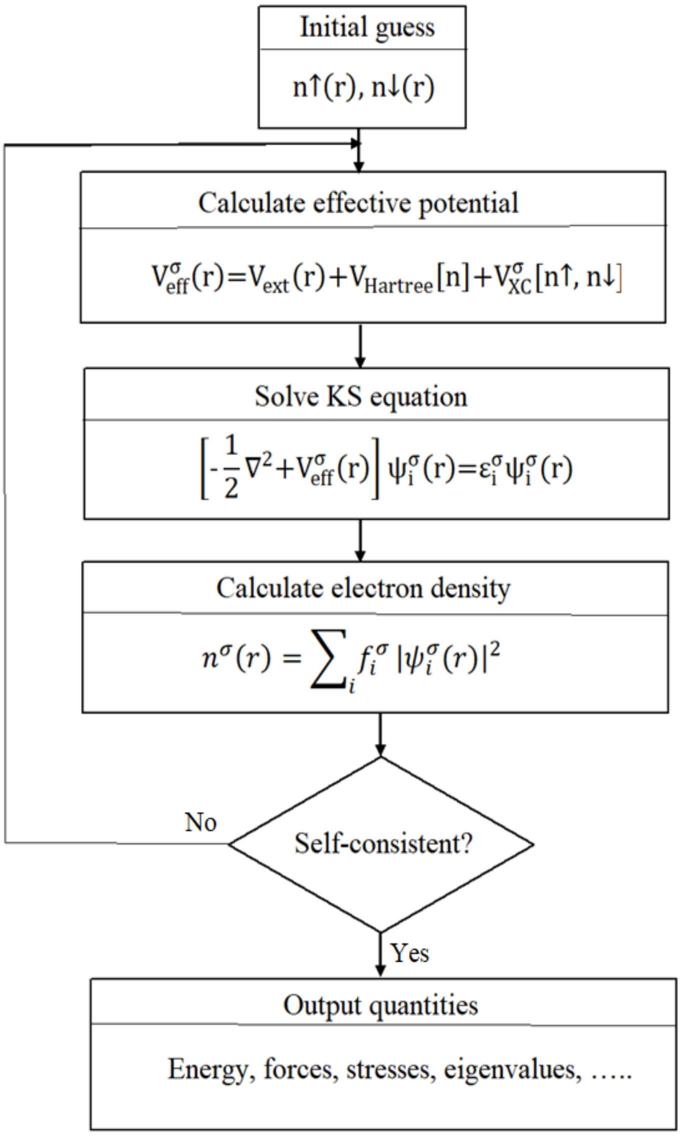

Figure 7: Schematic representation of the self-consistent loop for the solution of the Kohn-Sham equations (Martin, 2020)

2.6.2 Periodic Potentials

The Bravais lattice that forms a crystal is periodic in nature, which implies that the unit cell repeats in all directions in a regular array. This leads one to think that in neighbouring cells, the electrons that are prescribed to each atom should each encounter the same setting as their image. If V(r) is the potential of the system, then it can be described as V(r+R) = V(r) where R is the linear combination of the primitive lattice vectors. This also ensures that the ground state wave functions within each crystal are similar in each cell and obey the translational periodicity of the crystal (Kohanoff, 2006) since the potential defines the force acted upon by the electrons. This has major implications, leading to the theorem of Bloch.

2.6.3 The Bloch's Theorem

The macroscopic objects of a crystal can contain atoms in the order of 10^{23} repeated in all directions of the primitive lattice vectors. The relation between the properties of an electron in an infinite periodic system and those of the unit cell is what Bloch's theorem allows one to do (Kohanoff, 2006). The potential in a crystal lattice can be expected to differ from cell to cell periodically. Thus, the one-electron wavefunction can be written together with an imaginary phase factor (which manages the translational symmetry) (Ashcroft & Mermin, 1976) as the product of a function with an equal periodicity as the potential, so that it follows the boundary conditions of the Born-von Karman:

$\psi_k = e^{ik.r} U_k(r) \;\; with \;\; U_k(r) = U_k(r + a_i)$ whereby k is the reciprocal space crystal momentum vector. When the wavefunction is displaced with a unit vector R it produces:

$$\psi_k(r + R) = e^{ik.R} U_k(r) \tag{11}$$

which is valid for every R coming from the Bravais lattice. When one tries to find the probability distribution, the phase factor tends to drop out (Kohanoff, 2006):

$$\langle e^{ik.R} \psi_k(r) | e^{ik.R} \psi_k(r) \rangle = |\psi_k(r)|^2 \tag{12}$$

The phase factor must have the relationship expressed by Equation 13 as:

$$e^{ik.R} = e^{2\pi i} = 1 \quad \forall \;\, k \tag{13}$$

This limits the k values to the G reciprocal lattice vectors, thus further reducing the complexity of the solution technique. The reciprocal lattice is defined by its relation to the primitive vectors of the direct lattice (Ashcroft & Mermin, 1976):

$$b_1 = 2\pi \frac{a_2 \times a_3}{a_1.(a_2 \times a_3)} \qquad b_2 = 2\pi \frac{a_1 \times a_3}{a_1.(a_2 \times a_3)} \qquad b_3 = 2\pi \frac{a_1 \times a_2}{a_1.(a_2 \times a_3)}$$

2.6.4 Brillouin Zone Sampling and Irreducible Brillouin Zones

The Brillouin zones are volumes in reciprocal space separated by reciprocal lattice bisecting Bragg planes (Martin, 2020). With the first Brillouin zone described as the volume initiating from the origin and ending on the first Bragg plane, they are ordered by their distance from the origin. This particular Brillouin region, with a volume of $V_{BZ} = 2\pi/\Omega$, is synonymous with the Wigner-Seitz primitive cell in the reciprocal space, making it the smallest repeating unit developed from the k-points. The second Brillouin zone is the volume beyond the first Brillouin zone, which ends on the next Bragg planes it encounters, etc. (Ashcroft & Mermin, 1976). According to Bloch's theorem, it is necessary to evaluate only the electronic wave functions inside the unit cell, as only the phase factor can vary between the neighbouring cells (Kohanoff, 2006). However, for the computation of the all-electron wavefunction in the infinite solid, a finite number of electrons will be mapped to the wavefunction in the first Brillouin zone and will, in theory, require an infinite number of k-vectors.

In practice, this is only achieved in the first Brillouin zone using a finite number of k-points, although this value depends on different system features and desired properties (Kittel *et al.*, 1996; Kohanoff, 2006). The lattice structure’s symmetrical features allow for reductions in the number of k-points. Combinations of point symmetries (reflections, rotations and inversions) and translations leave the system unchanged and commune mostly with the Hamiltonian for periodic systems (Martin, 2020). The symmetric R_i and translational t_i operation on the wavefunction can be shown that are the Hamiltonian eigenfunctions producing the same $\varepsilon_i^{\boldsymbol{k}}$:

$$\psi_i^{R_i\boldsymbol{k}}(R_i r + t_i) = \psi_i^{\boldsymbol{k}}(r) \quad \psi_i^{{R_i}^{-1}\boldsymbol{k}}(r) = \psi_i^{\boldsymbol{k}}(R_i r + t_i) \tag{14}$$

This result enables us to identify what is known as the irreducible Brillouin zone (IBZ), which is the smallest portion of the Brillouin zone that contains all the information required for measuring the electronic structure. The use of IBZ can take drastic roles, which involve just a 1/48 of the entire Brillouin zone for high-symmetry cubic crystals to decrease the number of k-points to the sample (Kohanoff, 2006). Choosing k-points may also have a dramatic impact on the computation’s performance. In this study, BZ sampling employed the procedures suggested by Hinuma and coworkers (Hinuma *et al.*, 2017) and Setyawan and Curtarolo (Setyawan & Curtarolo, 2010) for orthorhombic systems. In k-points sampling, the framework developed by Monkhorst and Pack in 1976 (Martin, 2020) has been widely used in this research. For all symmetries, the Monkhorst-Pack-Grid is well known for metal systems, which need even finer sampling in order to monitor the Fermi surface shape. A set of k-points are generated by the general algorithm from a linear combination of the reciprocal lattice-vectors and coefficients determined by a set of natural numbers that end at q:

$$k = n_1 b_1 + n_2 b_2 + n_3 b_3 \quad n_i = \frac{2r - q - 1}{2q} \quad r = 1,2,3, \dots, q$$

2.7 Approximations used in the First Principal Calculations

2.7.1 Exchange-correlation Functional

The resulting energy from the potential for exchange-correlation constitutes just a small portion of the total energy, normally less than 10 per cent, but affects many properties of the studied materials. How the semi-local functionals underestimate the band differences, for example, is understood because the derivative discontinuity is wrong. The characteristics of the studied material must govern the selection and the construction of the potential. The potential can be decomposed into two parts in order to simplify this procedure: one for the pure exchange and the other for pure correlation functional:

$$E_{XC}[n] = E_X[n] + E_C[n] \tag{15}$$

The potential is, therefore, more versatile, and experimental data can also be used to suit it in the case of hybrid functionals. The most popular approaches to defining the E_{XC} in DFT are Local Density Approximation (LDA) and Generalized Gradient Approximation (GGA) which are both employed in this research.

2.7.2 The Local Density Approximation

The LDA is generated on the presumption that the density is constant locally and it is equal to the corresponding homogeneous electron gas:

$$E_{XC}^{LDA}[n(r')] = E_{XC}[n(r)|_{r=r'}] = \int dr E_{XC}\left(n(r)\right)(n(r)) \tag{16}$$

For the case of a homogeneous gas of electrons (Haynes, 1998), the term $E_{XC}(n(r))$ is the exchange-correlation single electron energy and can be evaluated using the Monte Carlo simulations. The technique was one of the firstly applied and can explain the behaviour of certain metallic materials accurately. The LDA XC functional was employed in this study to determine the structural, electronic and thermodynamic properties of $MASnI_3$ perovskites using the QE package, its detail is explained in the next sections.

2.7.3 The Generalized Gradient Approximation

If density variation is significant, as in the case of molecular systems, the system definition can be improved, taking into account the density gradient, and a similar claim can be applied to the higher-order derivatives:

$$E_{EX}^{GGA}[n(r')] = E_{XC}[n(r)|_{r=r'}\nabla n(r)|_{r=r'}; \dots, \nabla^{n} n(r)|_{r=r'}] \tag{17}$$

The function is defined with the GGA if the equation is truncated after the first derivative and it is called meta-GGA when the Laplacian (or other terms) are also considered. With respect to the kinetic energy density which includes the self consistently determined Kohn-Sham orbitals, this kind of functional can similarly be expressed and therefore take the name of the semi-local because a portion of the locality existing in the case of LDA and GGA is lost (Cramer, 2013).

The PBE (Perdew *et al.*, 1996) and PBEsol (Perdew *et al.*, 2008), developed by the Perdew group, are examples of GGA functionals. They do not provide adaptation to experimental data, but the ability to better explain different aspects of a system is provided by various functional expansions of the functional. The PBEsol, for example, is deduced from the PBE functional and it is designed to clearly replicate long-range interactions in the best way. This results in a better explanation of the equilibrium properties of solid-state materials, but at the expense of a more rough description of cohesive energy (Brivio, 2016). In this work, the two XC functionals, PBE and PBEsol, were employed to explore the structural, electronic as well as thermodynamic properties of $MASnI_3$. The PBE XC functional gave good results with the $MASnI_3$ compared to LDA and PBEsol, and it was later used in this study to determine the structural, electronic and thermodynamic properties of $GUAX_3$.

2.7.4 Hybrid Functionals

It has been found that most DFT problems emerge from the definition of the function of exchange-correlation. The LDA and GGA methods have been shown to be based on the local description of the electronic interactions, or semi-local. This implies that the energy correction depends on the electron density value at a particular point. Additionally, the exact energy exchange obtained via the Hartree-Fock method is not a local one, therefore, integrals on the entire space have to be taken into account to quantify it. The exchange-correlation feature must be replaced by a linear combination of either LDA or GGA functionals together with a HF exchange in order to incorporate a non-local energy correction within a DFT approach. Generally, the functionality obtained can be expressed as:

$$E_{XC} = (1-\propto)E_{XC}^{DFT} + \propto E_{X}^{HF} \tag{18}$$

It is possible to fit the linear combination parameter α with post-HF calculations or experimental data. The above equation can be extended to strengthen the functionality with the inclusion of extra terms. The B3LYP (Becke, 1997; Schmider & Becke, 1998) potential is a particularly effective example of the hybrid potential, which can be characterized as a linear combination of various contributions from various previous functions. The functional is widely utilized in molecular calculations. More recently, the PBE functional has emerged as a mother of the hybrid functionals such as PBE0 (Adamo & Barone, 1999; Adamo *et al.*, 1999) and HSE06 (Heyd *et al.*, 2003).

The PBE0 functional is expressed as:

$$E_{XC} = E_{X}^{GGA} + 0.25(E_{XC}^{HF} - E_{X}^{GGA}) \tag{19}$$

In addition, through the presence of a screening parameter that yields the GGA functional response at great distances, the HSE06 functional is extracted from the PBE0 as well as long-range corrections.

2.7.5 Many-Body Interaction

In the DFT method, the presence of exchange-correlation functionals defines electron-electron interaction as a means of solving the Schrödinger equation. An impossible or unrealistic system of equations is caused by the express treatment of the interactions between the particles. For instance, if an electron system is considered: one electron’s energy hinges on the positions of the other alternative electrons, but the positions and also the energy of all the other particles hinge on the electron itself at the same time. For this reason, the fraction of a particle’s energy which depends on the reaction of the system in relation to a particle itself is typically termed self-energy. The contribution of self-energy is absent within the DFT formalism. The multi-body effects are clearly approximated, and the functional exchange-correlation involves them. This method helps us to measure, with a good balance of cost and precision, the properties of extended materials.

If for example, electrons are strongly correlated or in excited-state energy ought to be considered for particular conditions and materials, accurate self-energy measurement is important to prevent anomalous effects. The self-energy is also measured using the Hartree-Fock method to urge the properties of the ground state, or through the Configuration Interaction (CI) to describe the excited state, or with a linear response strategy that describes a system's response to a little external disturbance. Typically, these methods are self-consistently solved, allowing us to achieve greater accuracy and to accurately explain various results, but these require a more rigorous computational cost. Another choice is the GW approximation that extends the multi-body portion of the interaction of the electron in terms of Green functions (G) by considering a screened Coulomb interaction (W). Within the GW approximation, the limitations for self-energy solving present within the DFT can be specifically determined. A single-particle view for the electronic structure is maintained by the GW formalism and depends on a perturbative approach.

If two-body interactions are especially important, the Bethe-Salpeter equations (BSE), of which the GW approach is also a special case, need to be resolved within the Green formalism. While computationally inexpensive in comparison to BSE resolution, the GW method is very demanding and calculations are built using different approximations and methods. These efforts are carried out because the GW techniques allow the implementation of a concept that defines electronic screening that is not present in HF, retaining local, non-local, and multi-body effects at the same time.

A starting ground state wavefunction is required since GW is a perturbation theory. It is typically sufficient to enhance the description of electronic bands, a function especially useful in the study of semiconductors, beginning with an LDA solution. Sadly, this is not a structured strategy with a predictable outcome. Different GW methods have been developed to enhance this aspect. These approaches include self-consistent enhancement strategies, not just the exchange-correlation aspect of the Hamiltonian ground-state, but also the potential for screening. The most common approach is the method of G0W0 (Hedin, 1965; Reining, 2018). The initial wave function is presumed to be the same as the LDA calculation in this approximation, and the first-order disturbances are the only to be taken into account for the self-energy correction. This correction is carried out with the application of a single measurement, i.e., without using the self-consistent scheme. With the quasi-particle GW, the G0W0 can be further improved.

2.7.6 Plane-wave Basis Sets

Electronic structure calculations are performed using a finite number of basis functions, which are preferably functions that imitate real orbitals (Jensen, 2017). When it comes to periodic systems, a good basis set is made up of a series of plane waves, since these systems are described by several attractive features. One concerns the solution of the condensed phase electronic structure, which means periodicity that it does not breach the Bloch theorem. In order to find the right solutions, the wave functions must have a periodic part and phase factor with frequencies relative to the vectors of the lattice (Martin, 2020). Plane waves conform naturally to this situation in the presence of constant external potential (Martin, 2020) and lead to a solution of the Schrödinger equation. However, the potential becomes drastically different as one moves closer to the nuclei, so a linear combination of increasing numbers of plane-waves is thus needed. Other reasons for this choice of basis are that plane-waves are mutually orthogonal, agree reasonably well with physics, are easily determined using fast Fourier transformations, and tend to converge with the addition of more basis functions (Kohanoff, 2006). These are all characteristics that follow the instructions provided by Jensen (Jensen, 2017). To see how plane-waves fit into this image is instructive. The functions' Fourier transform is written as:

$$u_k(r) = \int e^{ig.r}\, \bar{u}_k(g) dg \tag{20}$$

The values of g are restricted to the reciprocal of the lattice vector G by using Bloch's theorem which results in the general expression for the wavefunction as:

$$\psi_k(r) = \frac{e^{ik.r}}{\sqrt{\Omega}} \sum_{G=0}^{\infty} C_k\,(G) e^{iG.r} \tag{21}$$

with Ω representing the volume of the cell, the plane-wave basis set functions can be described as:

$$\phi_G(r) = \frac{1}{\sqrt{\Omega}} e^{iG.r} \tag{22}$$

followed by the orthogonalization and normalization procedures which gives:

$$\langle \phi_G | \phi'_G \rangle = \frac{1}{\Omega} \int_\Omega \; e^{(G-G').r} \, dg = \frac{1}{\Omega} \left(\Omega \delta_{G,G'} \right) = \delta_{G,G'} \tag{23}$$

which results in the wavefunction for different eigenstates j.

$$\psi_j^k(r) = e^{ik.r} \sum_{G=0}^{\infty} C_{jk} \, \phi_G(r) \tag{24}$$

2.7.7 Pseudopotentials

The pseudopotential principle dates back to Hans Hellman's 1935 work, whereby an effective potential for the valence electron scattering from metallic ion cores was developed. However, these pseudopotentials were too hard, and perturbation methods did not allow for accurate calculations at that time (Kohanoff, 2006). Shortly after that, Slater (1937) and Herring (1940) suggested the use of augmented plane-wave expansions with spherical solutions for the atomic problem, and the linear combination of the plane wave and core wave functions for valence states (Martin, 2020). The wavefunctions are orthogonal to the core states to acceptable choices for the expansion coefficients of the orthogonalized plane-wave method, and the use of core orbitals dramatically reduces the number of plane-wave components required for reproduction of the valence states.

In the familiar paper from Phillips and Kleinman in 1959, these advances led to further innovations and the roots of the modern pseudopotential method (Phillips & Kleinman, 1959). These authors formed the valence electron equations based on a weaker (softer) effective potential as additional information to the orthogonalized plane-wave method (Kohanoff, 2006). The nucleus and core electrons' strong Coulomb potential is replaced by the powerful ionic potential acting on the valence electrons in order to counteract the use of larger basis sets (Kohanoff, 2006). Thus, in an atomic reference configuration with frozen core approximation, the core states are essentially set and the ground state pseudo wave function identically mimics the all-electron wavefunction beyond the core cut-off radius (Singh & Nordstrom, 2006). Compared to all-electron wave functions, the fitting of pseudopotentials is normally done, with the benefit of reducing the number of electrons, electronic states, and basis sets to be considered, and thus the cost of calculation (Martin, 2020).

For electronic structure calculations, there are two general types of pseudopotentials. The first one created is the norm-conserving and has its origins in many simple physical consideration ideas. On Kohanoff ideas (Kohanoff, 2006), the norm-conserving pseudopotentials should consider atomic reference states where all-electron and pseudo-valence eigenvalues agree. Also, beyond a chosen core radius, all electron and pseudo-valence wavefunctions, as well as the integrated charge for each wavefunction, must agree. On the other hand, taking the logarithmic derivatives of the pseudo wavefunction and all-electron wavefunction and also the first energy derivative of the log derivatives of both wavefunctions agree at the core radius.

These characteristics have the effect of generating an accurate charge-density transferable wavefunction and are the reason for their success and continued use in research today (Singh & Nordstrom, 2006). The detriment to the norm-conserving potential is that a low cut-off radius (creating a hard potential) is needed in order to provide a pseudopotential that has high accuracy and transferability. Computational factors, however, lead one to want the least number of basis sets (cost scales as a power of the requested number of Fourier components) to generate smooth curves that are inherently restricted to larger cut-off radii (Kohanoff, 2006).

The norm-conserving pseudopotentials are faced with problems of hardness and high energy cut-off values. Vanderbilt (1990) proposed an option to mitigate this complication, whereby the norm-conserving restriction was relaxed, allowing for softer potentials with a significant reduction in energy cut-off values (Singh & Nordstrom, 2006). This became the basis for ultrasoft pseudopotentials. The softness of these potentials is correlated with their use of fewer base sets, re-expressing the issue in terms of a smooth function and an auxiliary function located around the core to reflect the density area that varies rapidly, enabling larger cut-off radii (Kohanoff, 2006). An additional term is added in the calculation to account for the difference in charge density since it is a function of the wavefunction to obtain the right results from all-electron wavefunctions (Martin, 2020). For example, in the simulation of oxygen with ultrasoft pseudopotential, Koval *et al.* (2005) acquired significant reductions in the energy cut-offs for plane-wave calculations, providing the same degree of accuracy with a decreased energy cut-off value from 150 Ry to 40 Ry. This study adopted the ultrasoft pseudopotentials from the QE website generated using the atomic code developed by Dal Corso (2014).

CHAPTER THREE

MATERIALS AND METHODS

3.1 Theoretical Background

In this section, the theory for simulations is discussed and the software and parameters used are explained. In this work, quantum chemical computational methods were employed for structural optimization and electronic properties estimation of the crystal compounds. The study comprises of running experiments on a computer to obtain and interpret results without real physical experiments. That approach can save a great deal of effort and time. The benefits of the computing methods are their flexibility, accuracy and relatively modest expenditures. The structures and atom constraints can easily be modified for emphasis on the specific instances to analyze the system's behaviour.

Here, the Quantum ESPRESSO (QE) simulation package was used for DFT calculations (Giannozzi *et al.*, 2009) running on a 12 cores machine with 32 GB of RAM and 2 TB HDD. A step by step method of employing QE in computing the electronic and thermodynamic properties is found in appendix 6. The DFT states that electron density distribution, which can be used to quantify different electronic properties of the system, can approximate the ground state energy of a system.

3.2 Introduction to Quantum ESPRESSO

The Quantum ESPRESSO (opEn Source Package for Research in Electronic Structure, Simulation and Optimization) open-source computer code (Giannozzi *et al.*, 2009) was used in the electronic and thermodynamic calculations. Using plane-wave basis sets and pseudopotentials to characterize the interaction of nuclei and electrons, the Kohn-Sham equations are solved within a density functional theory formalism. It is possible to download source files and binaries from the website http:/www.quantum-espresso.org under the GNU General Public License, along with advanced calculation plug-ins and some third-party packages. Once compiled, one can simulate several periodic and aperiodic networks using optimized mathematical libraries (BLAS, LAPACK, and FFTW) and parallel algorithms for high performance, being especially suitable for infinite crystalline systems. In combination with many common exchange-correlation functions (LDA, GGA, GGA+U), ultrasoft and norm-conserving pseudopotentials, as well as projector-augmented waves, can be used.

Pseudopotentials can either be downloaded from the website of Quantum ESPRESSO, taken from other UPF (Unified Pseudopotential Format) libraries, or generated using Quantum ESPRESSO's atomic code (Giannozzi *et al.*, 2009).

The relaxed crystal structures generate lattice constants and other physical quantities with properly selected pseudopotentials, which are extremely similar to experimentally measured values, to signify the robust ability of this software. A multitude of calculations and post-processing tools are also included in this software package. Just some of the procedures that can be chosen are Kohn-Sham orbitals and energies for isolated or periodic structures, structural optimizations using Hellmann-Feynman force, magnetic and spin-polarized ground-states, ab initio MD within a range of ensembles, and transition-path optimization. It is easy to plot quantities such as charge and spin density, Scanning Tunneling Microscope (STM) images, and electron localization functions and combine them with other tools, e.g. XCrySDen (Kokalj, 1999), for other applications.

With the PWscf (v 6.4.1) package, standing for Plane-Wave self-consistent field, structural optimization can be performed. In order to achieve self-consistency in the context of the pseudopotential method (Giannozzi *et al.*, 2009), this package uses an iterative approach with diagonalization techniques at each step. One can locate the equilibrium structure of ground-state energies by individually adjusting the lattice parameters. Determination of atomic forces and stresses, macroscopic polarization and Berry phases, orbital magnetization, minimum energy paths with the nudged elastic band system and Born-Oppenheimer or Car-Parrinello MD are other procedures available from the PWscf package.

Post-processing of the output data files allows the extraction of specific information from the calculations of the self-consistent field and position it in a format appropriate for graphical representations. The PostProc (v 6.4) package from Quantum ESPRESSO manages these routines. Charge density, the local density of states, selected squared wavefunctions, STM images, electron localization functions, the integrated local density of states, and different potentials are some of the quantities that can be plotted. It is possible to define various types of plots (line, plane, three-dimensional, polar) and output formats (including the common cube format). In addition, data can be stored in an intermediate (formatted) file so that further data sets can be summed up or subtracted at a later time. Output files can be read directly by the free plotting device Gnuplot (1D or 2D plots), or by the code plotrho.x that comes with PostProc and generates PostScript 2D plots, or by the advanced plotting applications

XCrySDen and gOpenMol (3D plots). These can also be made in different planar slices for multi-dimensional plots, giving one the freedom to choose particular axes for contour plots or values along a line.

The bands.x code reads data files, extracts the eigenvalues, and then regroups them into bands. The output is written to a file in a simple format that can be read and translated directly to a plottable format through the plotband.x auxiliary code. If k-points are not sequenced along lines, or if two consecutive points are the same, unpredictable plots can result. The symmetry study of the band structure is also carried out by the code bands.x.

The projwfc.x code calculates wavefunction projections over atomic orbitals. Atomic wave functions are those found in the pseudopotential files. The population analysis of Lowdin is currently applied (similar to the Mulliken analysis). You can also measure and write the predicted density of states (DOS) and projected DOS (PDOS), i.e., the DOS projected onto atomic orbitals, into a file. The data generated by the code projwfc.x can be further analyzed using the auxiliary codes sumpdos.x (the selected PDOS are summed through specifying the names of the files containing the desired PDOS) and plotproj.x.

3.3 Determination of Structural and Electronic Properties of the Orthorhombic $MASnI_3$

The $CH_3NH_3SnI_3$ crystallographic information (CIF) files were collected from the Open Crystallography Database (Gražulis *et al.*, 2009; Stoumpos *et al.*, 2013) and the Materials Project (Jain *et al.*, 2013), which are free crystal structure databases. The crystal structural properties were determined using the XCrySDen (Kokalj, 1999) and VESTA (Momma & Izumi, 2008) software and the band gaps and densities of states were estimated using Quantum ESPRESSO.

The input files for the QE were generated according to the program manual’s instructions (Giannozzi *et al.*, 2017). The initial simulation data were produced by convergence tests run on the structure by self-consistent field (SCF) calculations; the convergence values for the plane wave cut-offs (ecutwfc), lattice parameters along with the charge density cut-offs (ecutrho) in relation to the total energies were determined. Three separate functions of exchange-correlation (XC) were used with the ultrasoft pseudopotentials, Local Density Approximation (LDA), Perdew, Burke and Ernzerhof (PBE), (Ceperley & Alder, 1980; Perdew *et al.*, 1996), and Perdew-Burke-Ernzerhof revised solids (PBEsol) (Perdew *et al.*, 2008). Via convergence checks, ecutrho and ecutwfc were obtained as, 490 with 70 Ry, 600 with 60 Ry and 450 with 50 Ry, respectively for the PBEsol, PBE, and LDA functionals. As defined by Hinuma et al. (Hinuma *et al.*, 2017) and Setyawan, Curtarolo (Setyawan & Curtarolo, 2010) for orthorhombic structures, Brillouin zone sampling was performed. Cell relaxation (cell optimization) was carried out using the algorithm by Broyden-Fletcher-Goldfarb-Shanno (BFGS), as defined in the Quantum Espresso input file (Giannozzi *et al.*, 2017; Giannozzi *et al.*, 2009). The obtained coordinates after relaxation of the system are reported in Appendix 1. The method of vibration frequencies can be used when interested in the phonons and the vibration spectra by employing the density functional perturbation theory (DFPT) with the ph.x code implemented in QE (Baroni *et al*., 1987). The DFPT has grown in popularity as a technique for analyzing the vibrational and spectroscopic properties of materials, consistently yielding phonon frequencies and dielectric properties with only a few percent of the inaccuracy of experiment. However, because the focus of this research was on electrical and thermodynamic properties, the BFGS algorithm was sufficient. For each XC functional, the atomic structure positions and cell parameters were relaxed to a convergence energy threshold of 1.0E-08 Ry with a convergence force threshold of 1.0E-04 Ry/Bohr, which was adequate to attain a relaxed structure file (Giannozzi *et al.*, 2017; Giannozzi *et al.*, 2009). Furthermore, the QE database ultrasoft pseudopotentials consistent with the three exchange-correlation functions (PBEsol, PBE, and LDA) were used for both band structures and projected densities of states calculations. The code band.x was used to analyze the bands of the materials and the projwfc.x was employed in determining the projections of the wavefunctions over atomic orbitals.

3.4 Calculation of Structural and Electronic Properties of the Orthorhombic GUASnX$_3$

First-principles calculations were adopted using Quantum ESPRESSO software package code (Giannozzi *et al.*, 2009). The initial structures were created by substituting the MA-cations with GUA-cations and using the proposed Hautier and co-workers model (Hautier *et al.*, 2011) for structure predictions with the aid of Avogadro (Hanwell *et al.*, 2012) and VESTA (Momma & Izumi, 2008) editing and visualization tools, based on the orthorhombic structures of methylammonium tin halide perovskites available in the Materials Project database (Jain *et al.*, 2013). For the determination of the electronic and structural properties of $C(NH_2)_3SnX_3$, X = Cl, Br, I, the PBE XC functional (Perdew *et al.*, 1996) was employed.

In the simulation, a bulk crystal system with eight formula units (112 atoms) was used to preserve the symmetry. Following the usual procedures described in the literature, the structural parameter optimizations were performed at a 1.0E-04 Ry/Bohr mechanical force (Giannozzi *et al.*, 2017; Giannozzi *et al.*, 2009) which resulted in strong convergence of the internal forces along with the system's total energy. The optimized coordinates are recorded in appendix 2. Via several convergence tests, the cutoff charge and energy were obtained as 480 Ry and 60 Ry, respectively. The Martyna-Tuckerman method with truncated Coulomb interaction was used for the gaseous molecules and charged particles; the method is implemented in the QE software package. In the namelist SYSTEM, a related variable in the pw.x input is called assume_isolated, and the measurements are done by placing the species in large boxes based on their actual sizes. The system's minimum energy is found by optimizing the species using a self-consistent method.

3.5 Computation of Thermodynamic Properties of $MASnI_3$

The decomposition of the methylammonium tin iodide, $CH_3NH_3SnI_3$ into its solid-state products proceeds as shown by the following equation:

$$CH_3NH_3SnI_3(s) = CH_3NH_3I(s) + SnI_2(s) \quad (25)$$

The energy of this reaction $\Delta_r E$ was found through the total energies E of the components:

$$\Delta_r E = E(CH_3NH_3I) + E(SnI_2) - E(CH_3NH_3SnI_3) \quad (26)$$

The total energies E were computed for the relaxed structures of all the participants by using the three DFT XC functionals. Based on the enthalpy of reaction $\Delta_r E$, the determination of the enthalpy of formation of the orthorhombic phase of $CH_3NH_3SnI_3$ perovskite was carried out using the individual enthalpies of formation of the given precursors:

$$\Delta_f H°(CH_3NH_3SnI_3, s, 0\ K) = \Delta_f H°(CH_3NH_3I, s, 0\ K) + \Delta_f H°(SnI_2, s, 0\ K) - \Delta_r H°(0\ K). \quad (27)$$

3.6 Computation of Thermodynamic Properties of $GUASnX_3$, X = I, Br, Cl

The thermodynamic stability of the guanidinium halides, $GUASnX_3$ compounds was evaluated through the given decomposition routes:

$GUASnX_3$, s = GUAX, s + SnX_2, s (R1)

$GUASnX_3$, s = SnX_2, s + HX, g + CH_5N_3, g (R2)

$GUASnX_3$, s = SnX_2, s + X^-, g + GUA^+, g (R3)

The reactions energies, $\Delta_r E$ were calculated employing the total energies E obtained for the individual components:

$$\Delta_r E = \Sigma E(\text{products}) - E(\text{GUASnX}_3\text{, s}) \quad (28)$$

On the basis of the energies of the reactions, $\Delta_r E$, the enthalpies of formation of the $GUASnX_3$ were assessed.

3.7 Evaluation of the $CH_3NH_3SnI_3/Cu_2O$ Interface Properties

3.7.1 Slabs Preparation

An orthorhombic phase of $CH_3NH_3SnI_3$ was used as an absorber material and Cu_2O as a HTM (Fig. 8) to study the interaction between the two surfaces when they come in contact. The slabs for the two structures were prepared using VESTA software (Momma & Izumi, 2008) after relaxing the individual structures to save some computation time during the relaxation of the slabs. In order to obtain the common match in the dimensions of the two materials during the preparation of the heterostructure, Cu_2O was transformed by 2x3 in a and b directions, respectively (Fig. 9) to match the a and b lattice parameters of $CH_3NH_3SnI_3$.

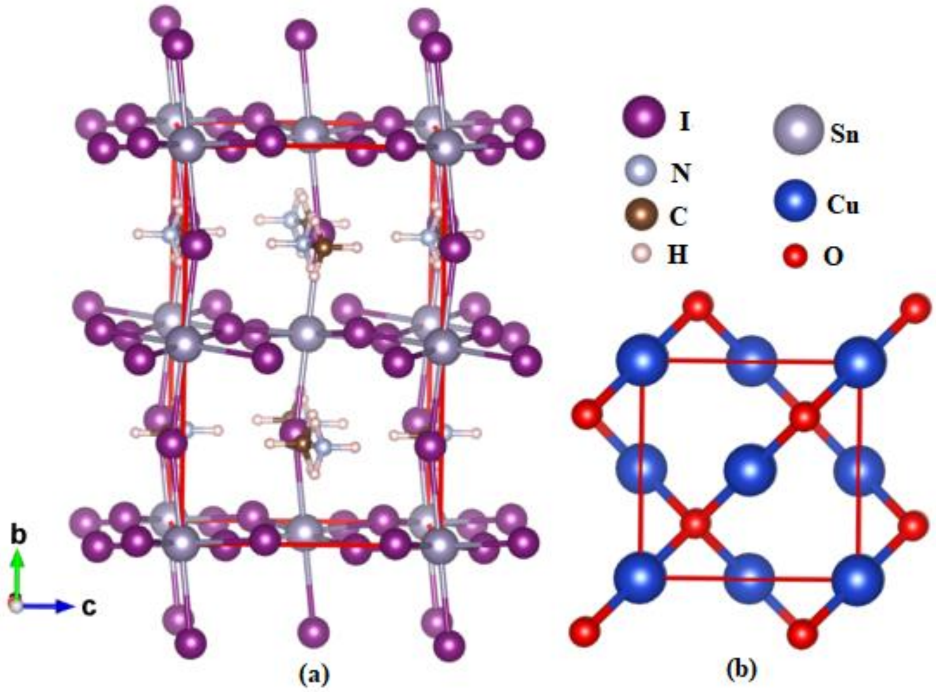

Figure 8: (a) Orthorhombic phase $CH_3NH_3SnI_3$ and (b) Cuprous oxide crystal (a direction is pointing into the page)

The lattice constants of the orthorhombic $CH_3NH_3SnI_3$ and cubic Cu_2O were fixed to the relaxed values. The (001) surface was exposed in the slab models of the $CH_3NH_3SnI_3$ with both MAI and SnI_2 termination models for proper studying of these surfaces (Fig. 10). The bottom layers of the atoms were fixed during the geometric relaxations and a vacuum of 20 Å was set above $MASnI_3$ in the c-direction to prevent the interaction between the upper and lower surfaces (Fig. 11).

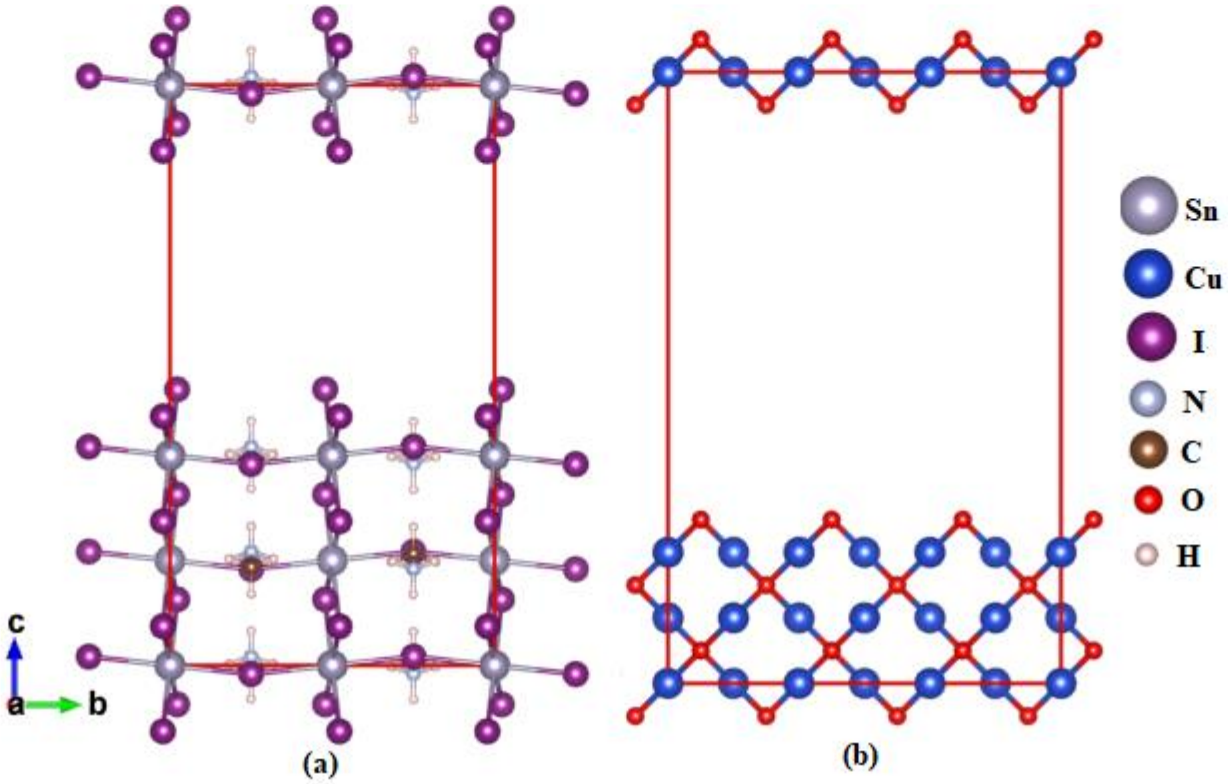

Figure 9: $CH_3NH_3SnI_3$ (a) and Cu_2O (b) slabs to be simulated individually

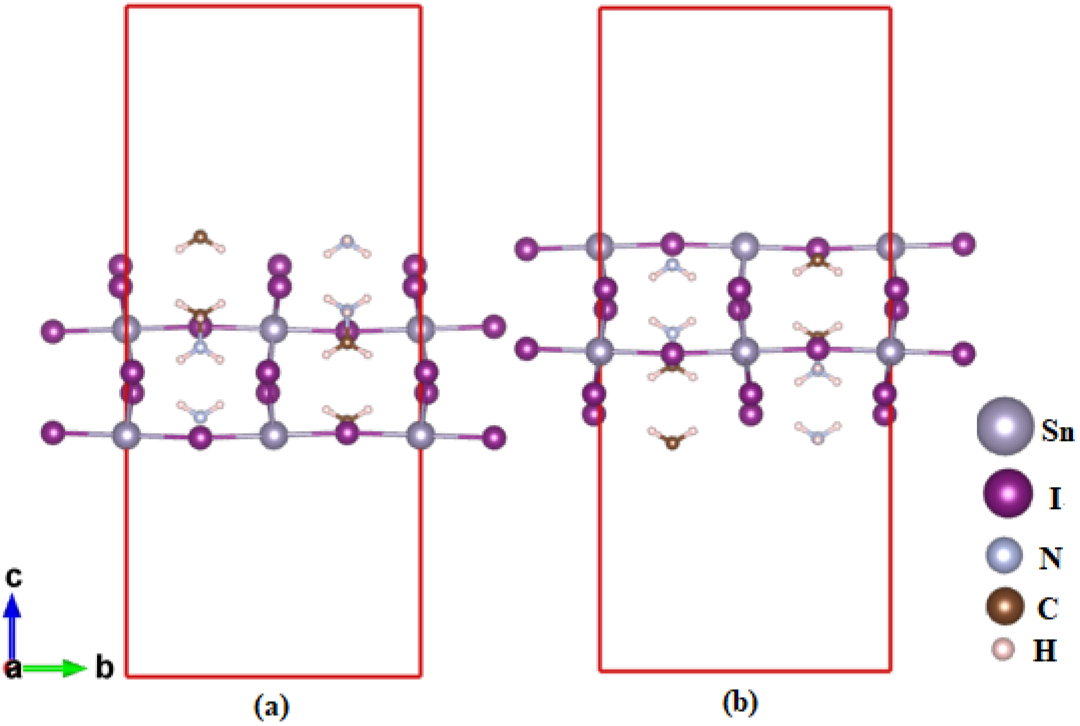

Figure 10: $CH_3NH_3SnI_3$ slabs (a) with MAI termination and (b) with SnI_2 termination

The Cu_2O/$MASnI_3$ interfaces are constructed by connecting the Cu_2O slab to the MAI−T or SnI_2−T (three MAI and three SnI_2 layers) slabs, leaving 20 Å of orthogonal vacuum in the direction of the surface along the non-periodic direction (Fig. 11). To prevent contact between anion–anion, i.e. I–O, Cu_2O slabs have been slightly moved in certain locations.

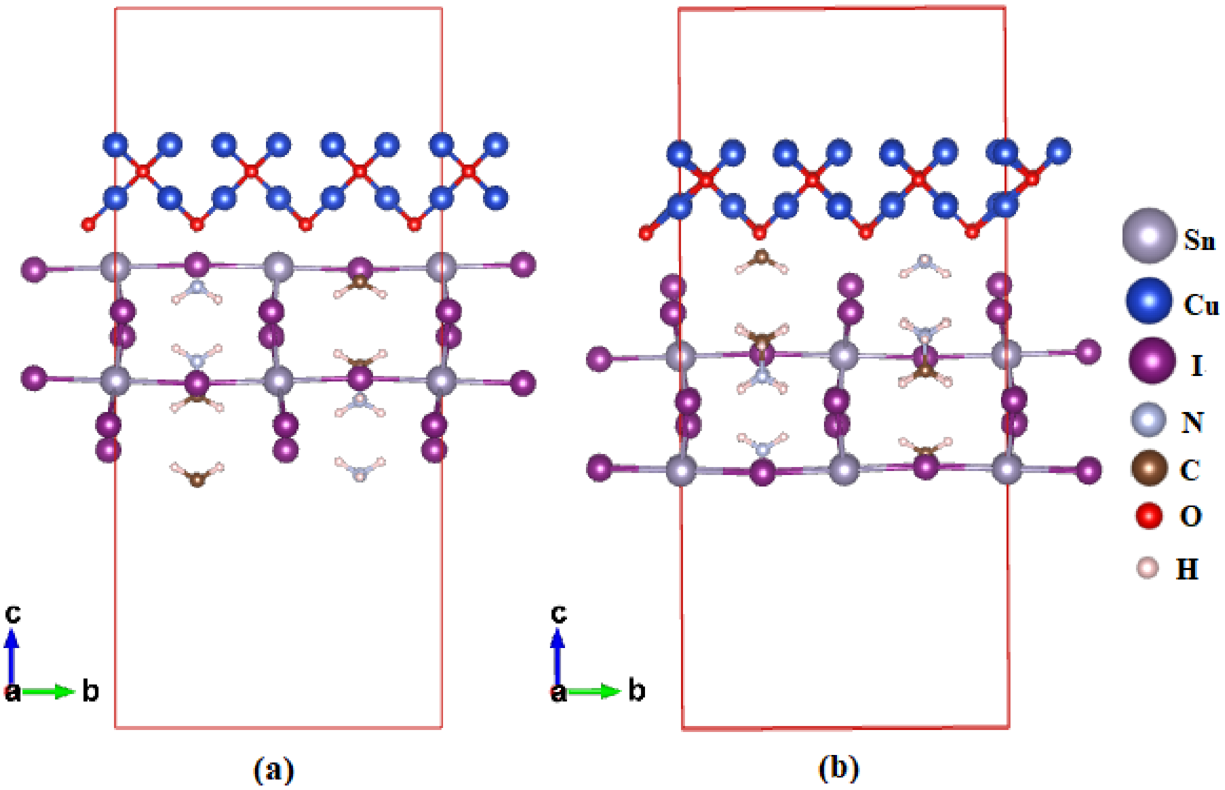

Figure 11: $CH_3NH_3SnI_3/Cu_2O$ composite (a) SnI_2-T and (b) MAI-T

3.7.2 Evaluation of the Binding Energy of the Composites

The PBE XC functional employed in the QE package was used to determine the binding energy of the composites. A 48 Ry kinetic-energy cutoff was set with a charge density cutoff of 432 Ry which were obtained through convergence tests performed using different values. The atomic positions (see Appendix 3) and cell parameters were relaxed with the PBE XC functional to energy convergence threshold of 1.0E-08 Ry and a force convergence threshold of 1.0E-03 Ry/Bohr which were enough to obtain a relaxed structure employing the Broyden-Fletcher-Goldfarb-Shanno algorithm (Giannozzi *et al.*, 2017; Giannozzi *et al.*, 2009). In addition, ultrasoft pseudopotentials from the QE database were used in determining all properties of the material under this study.

In order to understand the interfacial properties of the composite, the binding energies E_b were calculated and compared through employing the relation:

$$E_b = E_{total} - E_{HTM} - E_P \tag{29}$$

where E_{total}, E_{HTM} and E_P represent the total energies of the composite $MASnI_3/Cu_2O$, Cu_2O and $MASnI_3$, respectively.

CHAPTER FOUR

RESULTS AND DISCUSSION

4.1 Structural, Electronic and Thermodynamic Properties of the MASnI$_3$ obtained with LDA, PBE, and PBEsol XC Functionals

4.1.1 Structural Properties of MASnI$_3$

Through convergence tests on the cell parameters of MASnI$_3$ as well as the kinetic energy and charge density cutoffs, the equilibrium structures were obtained using the LDA, PBE and PBEsol XC functionals as represented in Fig. 12-14. The lattice parameter for celldm(1) is approximately equal to 8.5 Å as estimated by all three XC functionals while for celldm(2) and celldm(3) different values were obtained by using the three functionals, the PBE XC functional giving the closest values to the experimental parameters as summarized in Table 2.

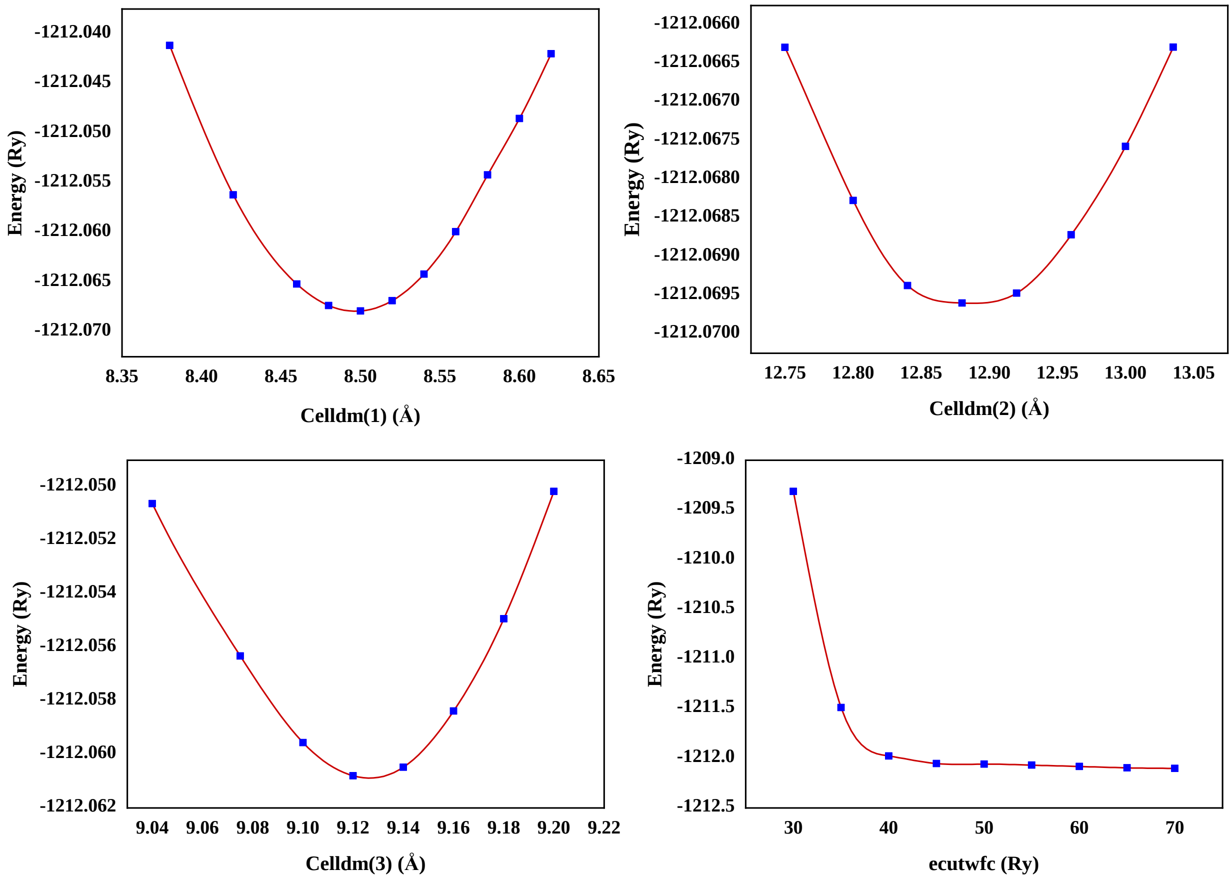

Figure 12: **The convergence for lattice parameters (celldm) and kinetic energy cutoff (ecutwfc) obtained for the MASnI$_3$ using the LDA XC functional**

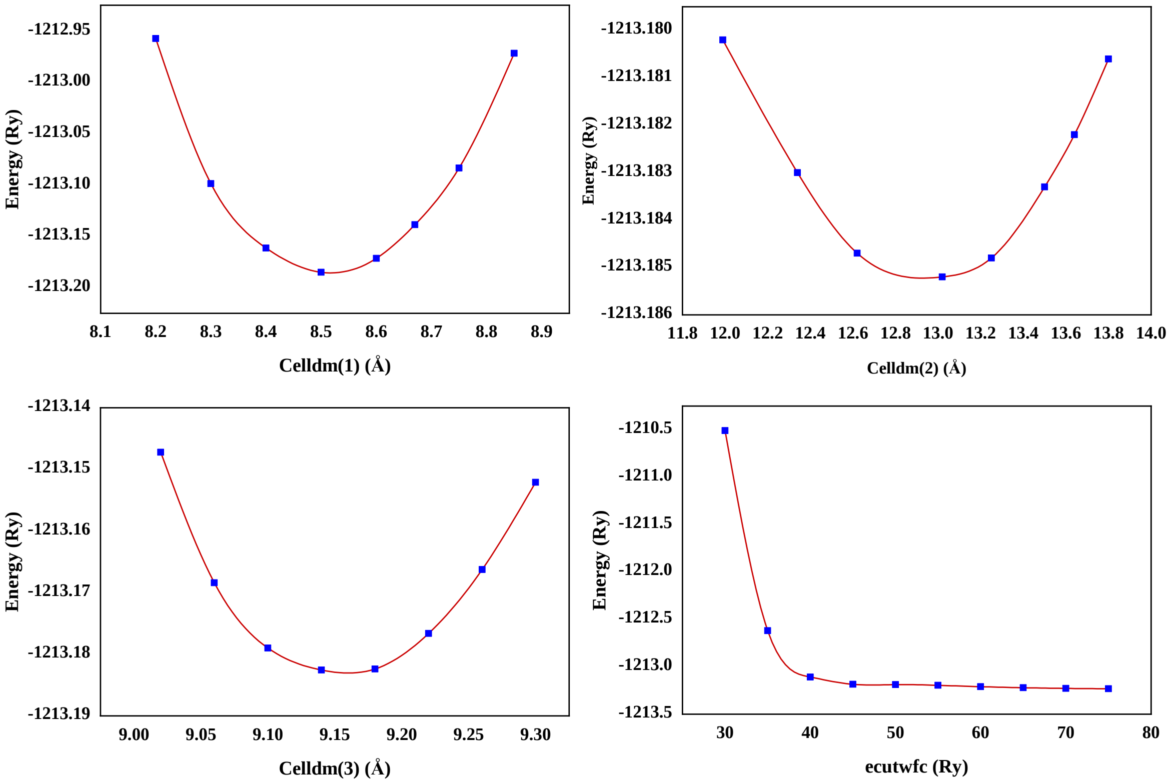

Figure 13: The convergence for lattice parameters (celldm) and kinetic energy cutoff (ecutwfc) obtained for the MASnI$_3$ using the PBE XC functional

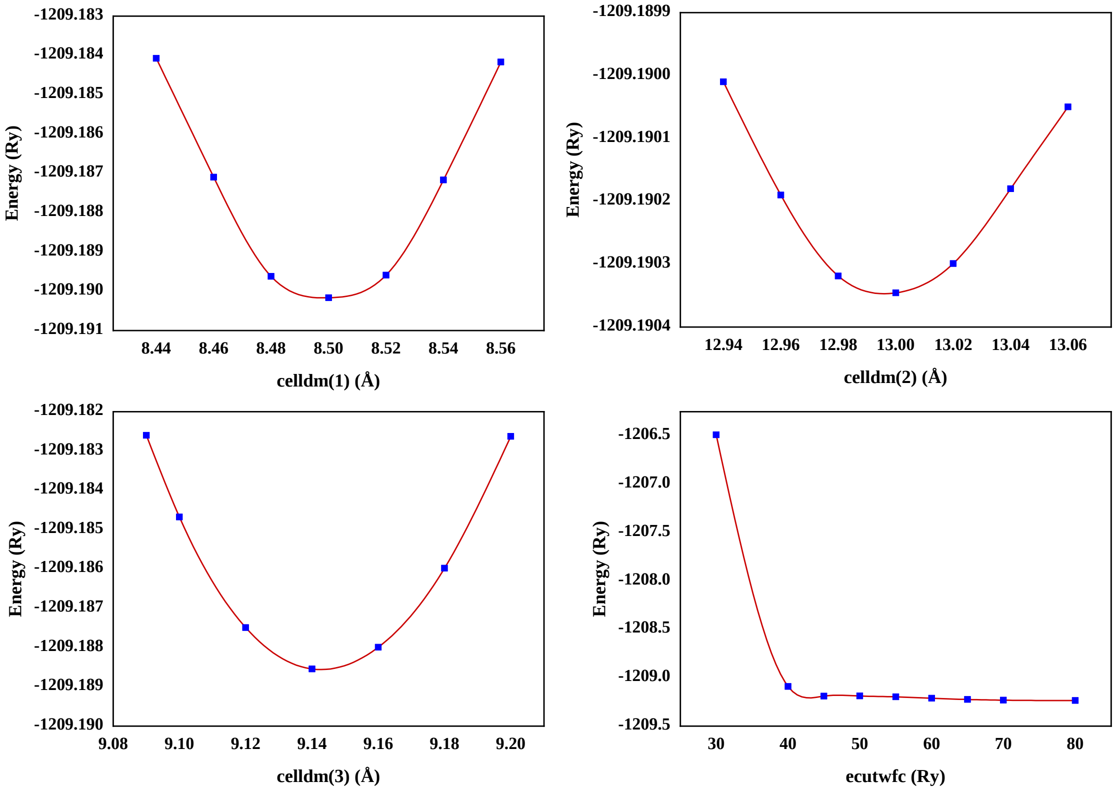

Figure 14: The convergence for lattice parameters (celldm) and kinetic energy cutoff (ecutwfc) obtained for the MASnI$_3$ using the PBEsol XC functional

The orthorhombic phase of $MASnI_3$ was considered with 48 atoms per cell. Through the use of the same values for ecutwfc and ecutrho, both the original database structure (unrelaxed structure) and the optimized structures were simulated to verify the validity of structure optimization prior to simulation. The applications, VESTA (Momma & Izumi, 2008) and XCrySDen (Kokalj, 1999), were used before and after optimization to display the structures. A corner-sharing network of $[SnI_6]$ octahedrons with the iodide anions and Sn-site cations, and the organic cation $[CH_3NH_3]^+$ between the octahedral corners is included in the structure (Fig. 15). If compare the lattice parameters before optimization and after during the structural relaxation there was no visible deformation of the structures, just minor changes can be observed in the lattice parameters and cell volume.

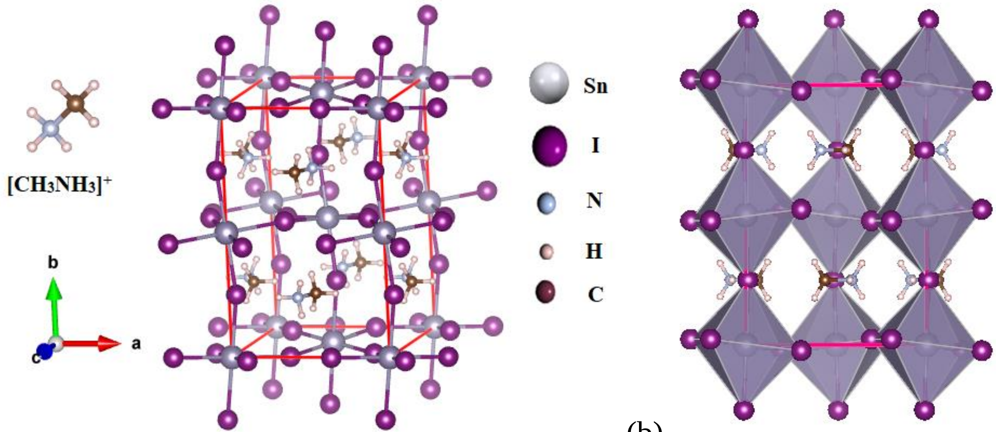

(a) (b)

Figure 15: The orthorhombic phase unit cell of $MASnI_3$ as visualization by VESTA (Momma & Izumi, 2008), (a) balls and sticks, and (b) polyhedral style

The structural properties of methylammonium tin iodide employing different exchange-correlation functionals compared to previous studies are summarized in Table 2.

Table 2: The structural properties and band gap of $MASnI_3$ using different XC functionals

Lattice parameters (Å)			Volume (Å^3)	E_g (eV)	XC functional	Ref.
a	b	c				
8.505	13.156	9.149	1023.70	0.88	PBE	This work[*]
				0.82	PBEsol	*ibid*
8.500	12.880	9.120	998.46	0.46	LDA	This work[**]
8.490	13.020	9.150	1011.44	1.12	PBE	*ibid*
8.500	13.000	9.140	1009.97	0.98	PBEsol	*ibid*
8.556	12.428	8.326	885.34	1.70	HSE06	Feng and Xiao (2014)
8.56	12.41	8.43	895.52	1.27	HSE06	Wu *et al.* (2016)
8.83	12.68	8.51	952.82	0.60	PBE(GGA)	Peng and Xu (2018)
				0.94	PBE	Suhaili *et al.* (2017)

[*] E_g estimated with the original lattice parameters obtained from the database (Jain *et al.*, 2013; Stoumpos *et al.*, 2013)

[**] E_g estimated with optimized parameters

4.1.2 Band Structure and PDOS of $MASnI_3$

There are important factors to explore the electronic structure of the hybrid halide perovskites, as these materials can be used as a light-harvesting medium. The determined band structures in the first Brillouin zone along the high symmetry lines are presented in Fig. 16-19 for both the unoptimized and optimized orthorhombic crystal of $MASnI_3$.

The orthorhombic crystal of $MASnI_3$ has a direct band gap at gamma point as estimated with various DFT functionals such as LDA, PBE and PBEsol. The Fermi levels are all between the conduction band minimum and valence band maximum for the three exchange-correlation functionals. Various E_g values of $MASnI_3$ have been obtained using the DFT functionals; PBEsol, PBE and LDA. The best possible accuracy of the band gap energies is obtained for the optimized $MASnI_3$ structure, i.e., 0.98 eV (PBEsol) and 1.12 eV (PBE), which are analogous to the experimental results 1.2-1.35 eV (Huang *et al.*, 2019; Stoumpos *et al.*, 2013). The E_g = 0.46 eV obtained using the LDA functional is much smaller than the experimental value. This finding is not unexpected because, generally speaking, the LDA XC functionality of the standard DFT method has the tendency to underestimate the band gap energy of solid-state semiconductors, as well as insulators by approximately 40 per cent (Perdew *et al.*, 2017; Perdew & Zunger, 1981), resulted from the assignment of a physical value to the Kohn-Sham energy level rather than from the inherent errors of the DFT methods

(Morales-García *et al.*, 2017). The unoptimized PBEsol and PBE functional values for O-phase are significantly underestimated in the band gap values of 0.82 eV and 0.88 eV, respectively, suggesting apparently that the crystal structure should be relaxed before the electronic properties are measured. It is important to note that other $MASnI_3$ orthorhombic structure DFT studies (Feng & Xiao, 2014; Peng & Xu, 2018; Suhaili *et al.*, 2017; Wu *et al.*, 2016) performed with different XC functionals recorded band gap values in a large range, in between 0.6 and 1.7 eV.

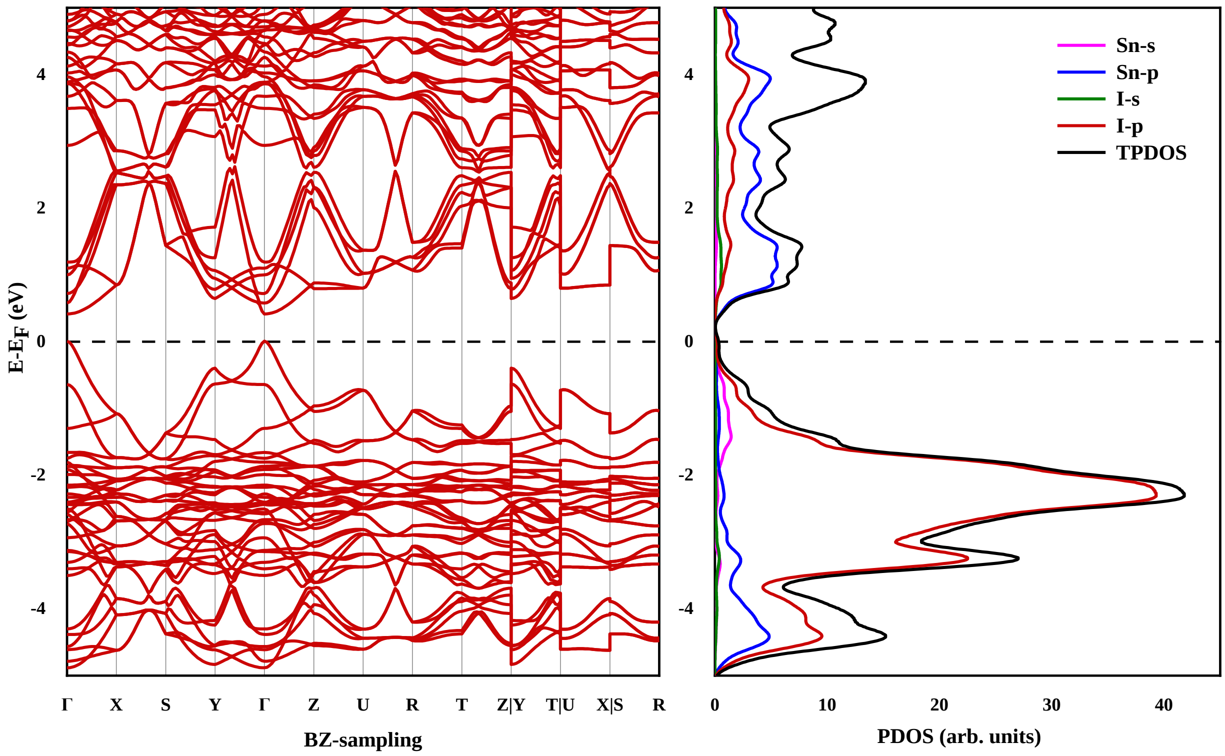

Figure 16: LDA optimized band structure of $MASnI_3$

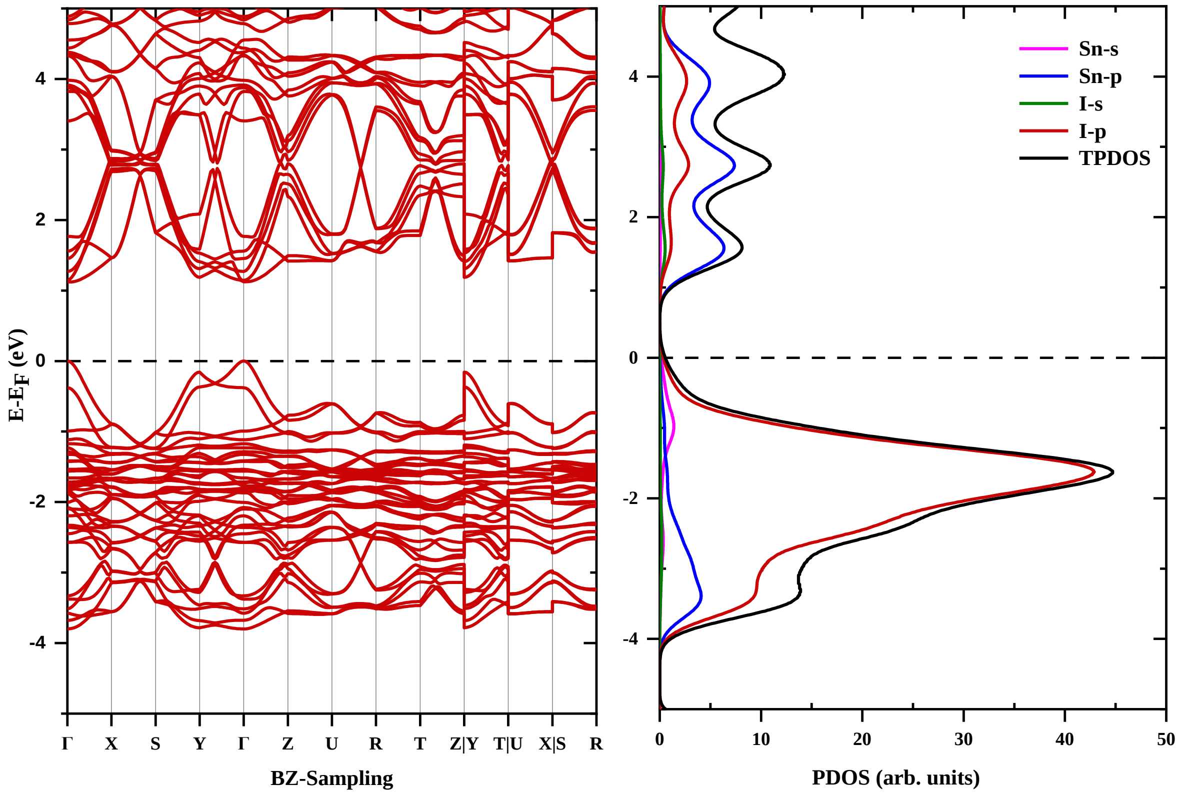

Figure 17: PBE optimized band structure of $MASnI_3$

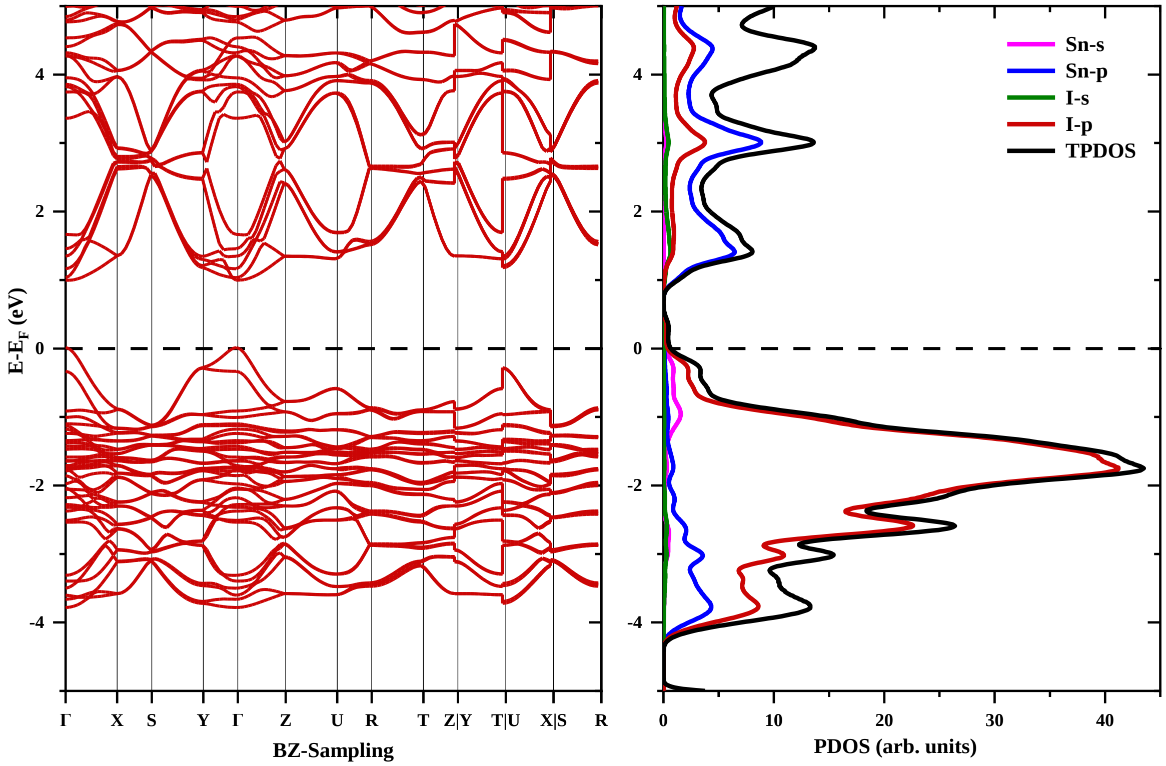

Figure 18: PBEsol band structure and PDOS of $MASnI_3$

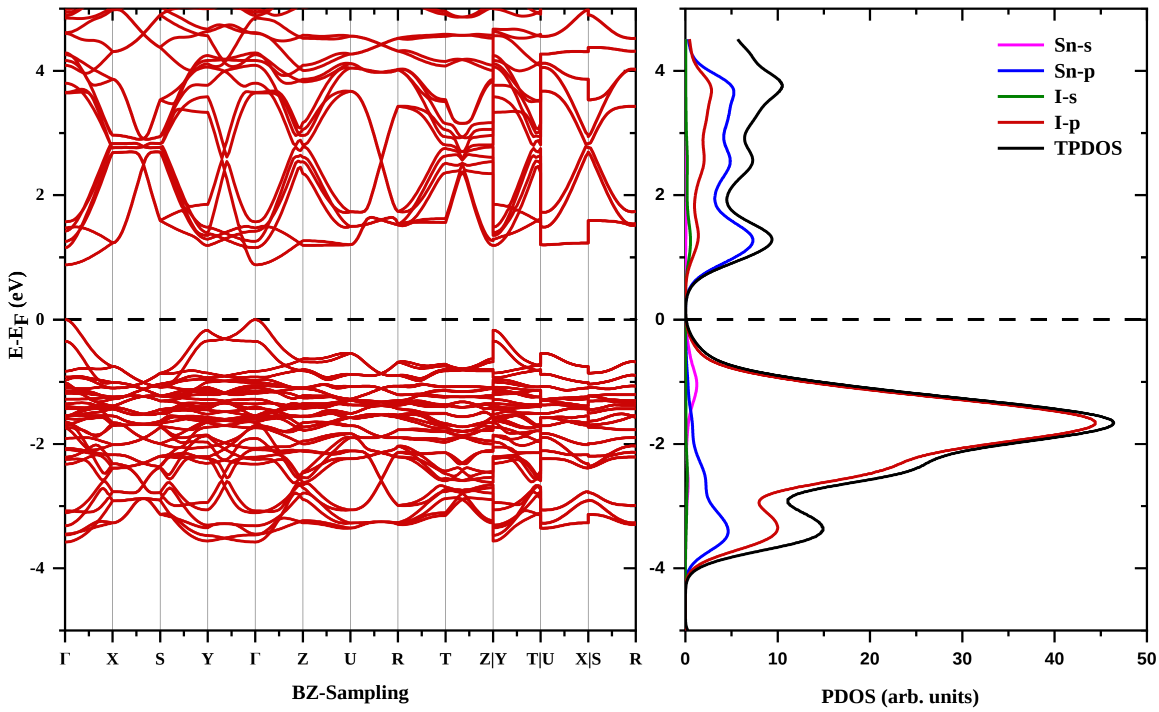

Figure 19: Unoptimized orthorhombic MASnI$_3$ band structure using PBE XC functional

Using the code projwfc.x, as implemented in the Quantum ESPRESSO package, the projected total state densities (TPDOS) and the projected state densities (PDOS) of the orthorhombic MASnI3, were determined. The PDOS reveals the interaction between orbitals to comprehend the relation among the atoms in the system (Fig. 16-19, right-hand side). The study offers a clearer understanding of the changes in the band gap as affected by the electronic conditions of the atoms, tin and iodine. With minor overlaps with 5s states, the 5p-state atoms of iodine are the primary contributors to the valence band's maximum value. The 5p-states of Sn atoms are involved in creating the minima of conducting band with a minor contribution from the 5p-state of the iodine atoms. The position of the Fermi level situated between the valence and conduction band is calculated based on the electron density of the Sn and I atoms' p-states in the perovskite.

4.1.3 Thermodynamic properties of MASnI$_3$

In determining the stabilities of materials when exposed to light, moisture, and heat, the decomposition reactions energy, and the enthalpy of the formation of many photovoltaic materials are important. Both methylammonium-based tin and lead halide perovskites undergo rapid conversion into halides under high humidity conditions (Nagabhushana *et al.*, 2016; Zhao & Park, 2015). The decomposition of MASnI$_3$ into the solid-state products of

CH_3NH_3I(s), and SnI_2(s) is shown via Equation 25. Through the total energies E of the reacting components, the energy of the reaction $\Delta_r E$ was found:

$$\Delta_r E = E(SnI_2) + E(CH_3NH_3I) - E(CH_3NH_3SnI_3). \quad (30)$$

The total energies E of the components were computed using the three DFT XC functionals mentioned earlier for the relaxed structures of all the participants (Table 3). As can be shown, the XC feature significantly affects the measured $\Delta_r E$: 9 kJ mol^{-1} (PBEsol), 37 kJ mol^{-1} (PBE) and –22 kJ mol^{-1} (LDA). The orthorhombic $MASnI_3$ is considered to be stable at temperatures below 110 K (Parrott *et al.*, 2016; Takahashi *et al.*, 2013), so the PBE outcome seems most rational. The enthalpy of formation of the orthorhombic phase $CH_3NH_3SnI_3$ can be calculated on the basis of the $\Delta_r E$ by means of the enthalpies of precursor formation:

$$\Delta_f H°(CH_3NH_3SnI_3, s, 0\ K) = \Delta_f H°(SnI_2, s, 0\ K) + \Delta_f H°(CH_3NH_3I, s, 0\ K) - \Delta_r H°(0\ K). \quad (31)$$

There are available reference values: $\Delta_f H°(CH_3NH_3I, s, 298\ K) = -200.7$ kJ mol^{-1} (Wilson, 1976) and $\Delta_f H°(SnI_2, s, 0\ K) = -152.4$ kJ mol^{-1} (Gurvich *et al.*, 1992). Assuming that the correction of lattice vibration energies for the reaction 24 is negligible, $\Delta_r E \approx \Delta_r H°(0\ K)$ is acceptable here. Furthermore, the study proposes that the increase in enthalpy $H°(298) - H°(0)$ for CH_3NH_3I does not exceed a few kJ mol^{-1}. Ciccioli and Latini (2018) considered similar assumptions for the decomposition reaction of lead perovskites $CH_3NH_3PbX_3(s) = PbI_2(s) + CH_3NH_3X(s)$, X = Cl, Br, I. The enthalpy of the formation of O-phase tin perovskite $CH_3NH_3SnI_3$ was thus obtained (Table 3). As discussed in the previous parts, in determining the electronic properties, the PBE XC functional outperformed the other two, so the considered accurate values of the enthalpy of formation and reaction are $\Delta_f H°(CH_3NH_3SnI_3, 0\ K) = -390$ kJ mol^{-1} and $\Delta_r H°(0\ K) = 37$ kJ mol^{-1} respectively.

Table 3: The thermodynamic properties of methylammonium tin iodide

XC functional	–*E*, Ry			$\Delta_r H°$(0 K), kJ mol^{-1}	$-\Delta_f H°$(0 K), kJ mol^{-1}
	$MASnI_3$	MAI	SnI_2		
LDA	303.095607	73.460970	229.651248	–21.8	331
PBE	303.298946	73.449692	229.821122	36.9	390
PBEsol	302.377144	72.961524	229.408919	8.8	362

These findings are worth comparing with the available literature data for the methylammonium lead perovskite, $CH_3NH_3PbI_3$(s). The decomposition reaction enthalpy $\Delta_r H°(298\ K) = 34.5 \pm 1.0$ kJ mol^{-1} was measured by solution calorimetry (Nagabhushana *et al.*, 2016) for the tetragonal phase of $MAPbI_3$. The exploitation of the enthalpy of formation of PbI_2, $\Delta_f H°(PbI_2, s, 298\ K) = -176$ kJ mol^{-1} (Gurvich *et al.*, 1992), the enthalpy of formation of $CH_3NH_3PbI_3$(s) can be estimated as $\Delta_f H°(CH_3NH_3PbI_3, s, 298\ K) = -411$ kJ mol^{-1}. The calculation of the $\Delta_f H°(MAPbI_3$, O-phase, 0 K$) \approx -414$ kJ mol^{-1} was considered by taking into account the enthalpy of phase transition from tetragonal to orthorhombic of 3 kJ mol^{-1} (Onoda-Yamamuro *et al.*, 1990) and neglecting the enthalpy increment, $H°(298) - H°(0)$. Compared to this value (− 414 kJ mol−1), the result for the enthalpy of formation of the tin perovskite (− 390 kJ mol−1) is in a good accordance. It is also important to note that the difference in enthalpy of formation, $\Delta_f H°$ between the methylammonium tin and lead perovskites (24 kJ mol^{-1}) appeared to be almost equal to the difference between PbI_2 and SnI_2 (23 kJ mol^{-1}). So, the evaluated values of the enthalpy of the reaction $\Delta_r H°(0\ K) = 37$ kJ mol^{-1} and enthalpy of formation of the O-phase perovskite $\Delta_f H°(CH_3NH_3SnI_3, 0\ K) = -390$ kJ mol^{-1} indicate the stability of the O-phase $CH_3NH_3SnI_3$ at low temperature, in agreement with experimental findings.

4.2 Structural, Electronic and Thermodynamic Properties of the $GUASnX_3$, X = Cl, Br, I

4.2.1 Structural Properties of $GUASnX_3$

Convergence tests were conducted for the kinetic energy cutoff with the total energy of the $GUASnX_3$ system by using the PBE XC functional. Through these tests, the equilibrium structures were obtained at the minimum energy for $GUASnCl_3$, $GUASnBr_3$, and $GUASnI_3$, respectively, as presented in Fig. 20.

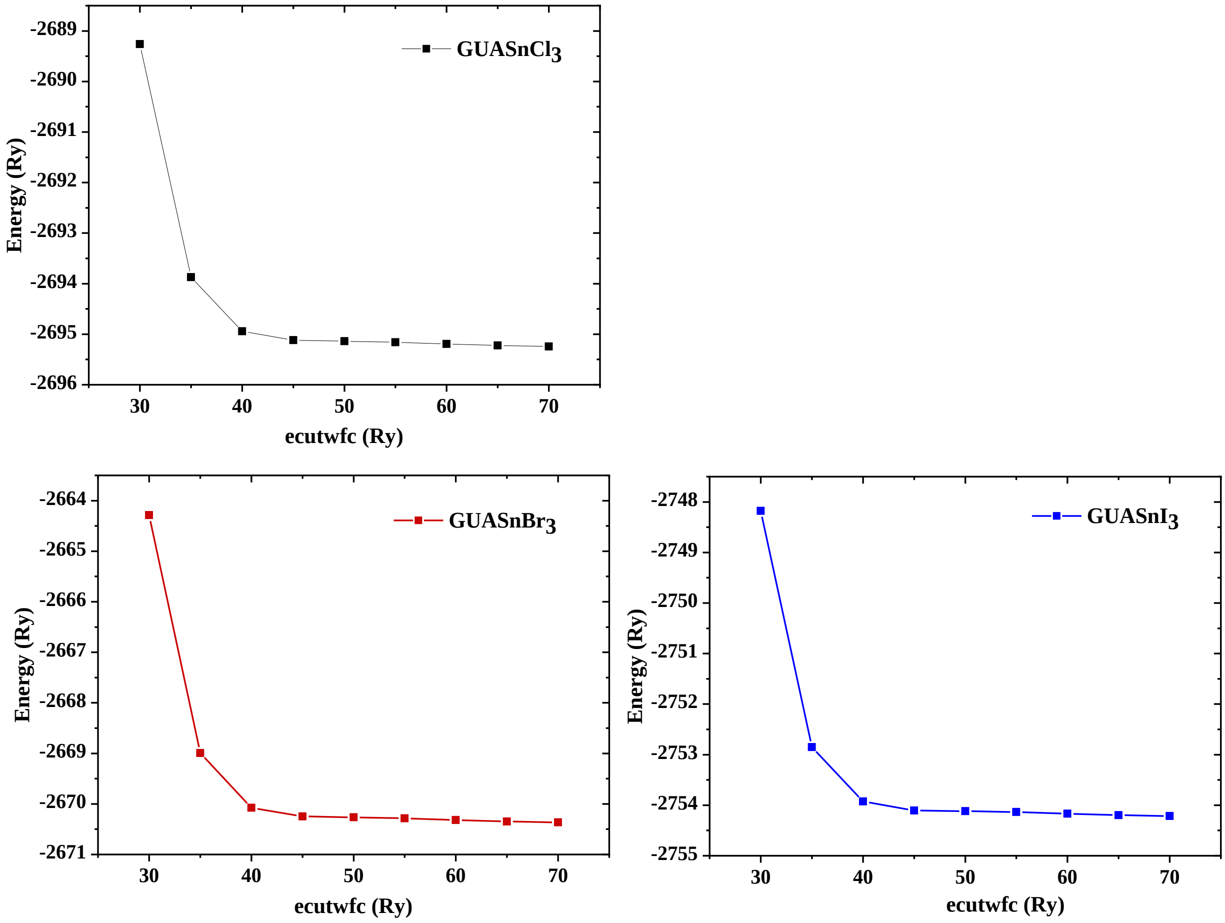

Figure 20: The convergence for the kinetic energy cutoff (ecutwfc) of GUASnX$_3$ (X = Cl, Br, I) using the PBE XC functional

The $C(NH_2)_3SnX_3$ crystals under analysis with a Pbca space group, group number 61 and D_{2h} symmetry have an orthorhombic perovskite structure. Unlike the methylammonium cation, $CH_3NH_3^+$ with C_{3v} symmetry (Angell *et al.*, 1957), the guanidinium cation, $C(NH_2)_3^+$ has a D_{3h} symmetry structure (Chiarella *et al.*, 2008). Optimized unit cells from the crystals $C(NH_2)_3SnCl_3$, $C(NH_2)_3SnBr_3$, and $C(NH_2)_3SnI_3$ are shown in Fig. 21. Also is seen the A-cation $C(NH_2)_3^+$ incorporated in the structure of tin halide perovskites. Table 4 summarizes the computed equilibrium lattice constants of $C(NH_2)_3SnX_3$ (X = Cl, Br, I) together with the theoretical data for similar tin halide perovskites available in the literature. No experimental or theoretical data for either lattice constants or the band gaps for the orthorhombic $C(NH_2)_3SnX_3$ (X= Cl, Br, I) compounds are available in the literature to the best of our knowledge.

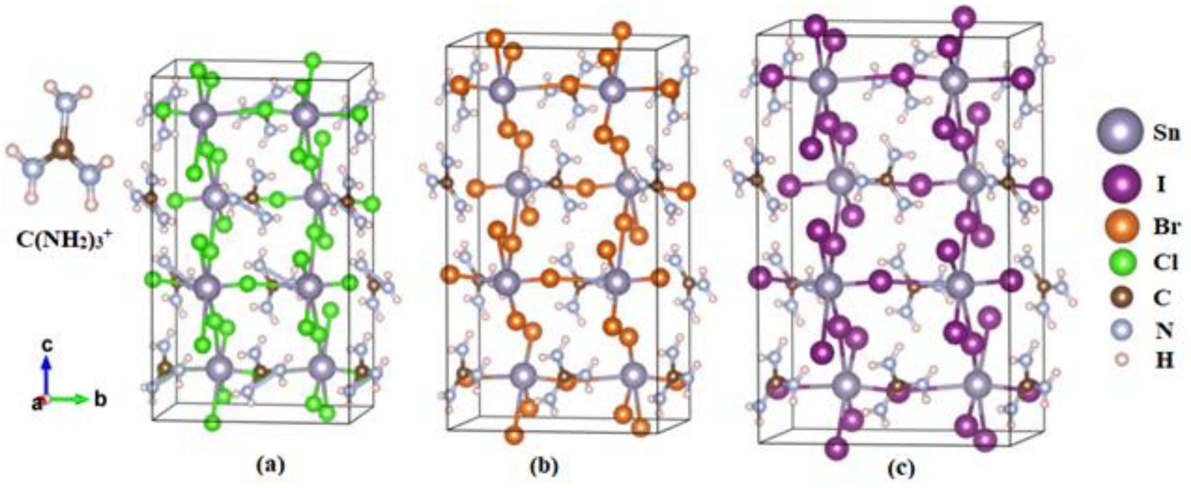

Figure 21: The optimized orthorhombic phase unit cells (a) $C(NH_2)_3SnCl_3$, (b) $C(NH_2)_3SnBr_3$, and, (c) $C(NH_2)_3SnI_3$ as visualized by using VESTA (Momma & Izumi, 2008) software

The volume of orthorhombic guanidinium perovskites is clearly shown to rely on the halide attached; the unit cell of $GUASnI_3$ has the largest volume in comparison to Br and Cl guanidinium perovskites due to the largest iodine dimension. In the latter, parameter c contributes more to the cell volume due to its largest size among the three lattice parameters; a, b, and c, of the crystal structure; c> b> a. Taking into account the other tin halide perovskites mentioned in Table 4, their cell volume does differ widely as from the most compacted cubic unit cell of $CH_3NH_3SnBr_3$ with the lowest volume of 204.34 Å^3 to the lowermost symmetry trigonal unit cell of trimethylammonium tine iodide perovskite $(CH_3)_3NHSnI_3$ with the highest volume of 16093 Å^3 due to their different crystal systems. However, depending on the structure of the perovskite to be unique due to the A-cation attached, their band gaps range between 1.12 and 3.69 eV.

Table 4: The $C(NH_2)_3SnX_3$ (X = Cl, Br, I) equilibrium lattice parameters and band gaps along with other structures of the tin halide perovskite crystals

Compound	Crystal phase	Lattice parameters (Å)			Volume (Å^3)	E_g (eV)	Ref.
		a	b	c			
$C(NH_2)_3SnCl_3$	orthorhombic	8.054	12.405	17.827	1781.09	3.00	This work
$C(NH_2)_3SnBr_3$	orthorhombic	8.424	12.862	18.373	1990.71	2.47	*ibid*
$C(NH_2)_3SnI_3$	orthorhombic	8.958	14.172	19.020	2414.64	1.78	*ibid*
$CH_3NH_3SnCl_3$	monoclinic	5.690	8.230	7.940	371.82	3.69	Chiarella *et al.* (2008)
$CH_3NH_3SnBr_3$	cubic	5.890	5.890	5.890	204.34	2.15	Chiarella *et al.* (2008)
$CH_3NH_3SnI_3$	orthorhombic	8.490	13.020	9.150	1011.44	1.12	This work
$(CH_3)_3NHSnI_3$	trigonal	16.040	16.040	72.226	16093.0	2.55	Stoumpos *et al.* (2017)
κ-$[C(NH_2)_3]SnI_4$	orthorhombic	13.047	13.558	9.348	1653.58	2.10	Stoumpos *et al.* (2017)
θ-$C(NH_2)_3SnI_3$	hexagonal	9.3309	9.3309	21.546	1624.59	1.90	Stoumpos *et al.* (2017)
$(CH_3)_4NSnI_4$	orthorhombic	8.8370	8.6191	27.562	2099.30	2.60	Mitzi (1996)
µ-$CH_3CH_2NH_3SnI_3$	hexagonal	8.966	8.966	23.079	1606.70	2.18	Stoumpos *et al.* (2017)
$HC(NH_2)_2SnI_3$	orthorhombic	12.512	12.517	12.510	1959.20	1.41	Stoumpos *et al.* (2013)
θ-$CH_3C(NH_2)_2SnI_3$	hexagonal	9.2277	9.2277	15.286	1127.22	2.15	Stoumpos *et al.* (2017)
$C_3N_2H_5SnI_3$	trigonal	9.2735	9.2735	34.921	2601.00	2.20	Stoumpos *et al.* (2017)

4.2.2 Electronic Properties of $GUASnX_3$

For the three $GUASnX_3$ perovskites, the measured band structures along the high symmetry points in space are shown in Figs. 22-24. For these three perovskites, the band structures display a direct band gap at the gamma symmetry points, which accords to that recorded for guanidinium lead halide perovskites (Dimesso *et al.*, 2016; Jodlowski *et al.*, 2017). The band gap is reduced from 3.0 eV ($GUASnCl_3$) to 1.78 eV ($GUASnI_3$). The band gap is usually underestimated by DFT, as have shown by several studies (Borriello *et al.*, 2008; Chiarella *et al.*, 2008; Perdew *et al.*, 2017; Takahashi *et al.*, 2011; Umari *et al.*, 2014). The SOC-GW method was suggested in Umari *et al.* (2014) to improve the results; the band gaps of the $MAPbI_3$ and $MASnI_3$ estimated using this method seemed to agree well with the experimental values. The spin-orbit coupling effect was investigated in Pb and Sn perovskites (Even *et al.*, 2013; Even *et al.*, 2014; Umari *et al.*, 2014), with the effect in the Sn perovskites being three times less. The relativistic effects may be expected to be less pronounced in guanidinium perovskites, and they may be exempted for Sn-based perovskites.

Studies (Chiarella *et al.*, 2008; Mitzi *et al.*, 1995) have shown that the transport properties of $CH_3NH_3SnX_3$ species have progressed in the Cl → Br → I sequence from semiconductivity to metallicity, as reflected by their decrease in band gap from $MASnCl_3$ to $MASnI_3$. Thus, for the studied guanidinium compounds, identical conductivity character transformation is also seen. However, the halogen can be considered as the only distinct structural element in the $GUASnX_3$, Cl is more electronegative than Br and I, it can be inferred that with the increase in electronegativity of X, the band gap of $GUASnX_3$ increases. As the atomic size decreases as one moves down the periodic table of elements group, the bond length Sn-X (X = Cl, Br, I) increases in the order Sn-Cl → Sn-Br → Sn-I, resulting in a decrease in bond strength. With the Sn-X bond elongation, the octahedra network tilting gradually decreases. The tilting behaviour is induced by the GUA-cation's ionic radius along with its planar form (Nazarenko *et al.*, 2019), and the Sn-X-Sn bridging angles (Borriello *et al.*, 2008). The increased octahedral tilting happened to reduce the overlap between the Sn and X orbitals (Prasanna *et al.*, 2017), allowing the bands to shift to higher energies and widening the band gap. In this analysis, as the octahedral tilting from Cl to I decreases, the band gap decreases as well, as seen in the guanidinium tin halides.

The band gap expansion from $MASnX_3$ to $GUASnX_3$ (X = Br, I) is observed; for example, the band gap is 1.12 eV for $CH_3NH_3SnI_3$ (see section 4.1.2) and 1.78 eV for $C(NH_2)_3SnI_3$; this widening is most likely due to the GUA-cation's much greater ionic radius than the MA-cation. It is well known that bulky cations are much difficult to organize inside the inorganic networks because their size causes the 3D frame to break down and evolve into a 2D-like structure, which widens the band gap (Kieslich *et al.*, 2014, 2015). These hypotheses are supported by an experimental analysis by Szafranski and coworkers (Szafrański, 1997), who discovered the instability of iodoplumbate compounds based on GUA, together with a stable phase yellow in colour and a reddish metastable phase for the $GUAPbI_3$, with the yellowish evolving as a 2 dimension layered system having a larger band gap. The wider perovskite band gap results in an improvement in the open-circuit voltage of photovoltaic devices (Luo *et al.*, 2018). Studies show that iodide perovskites are promising photovoltaic materials with light absorption in the 1.2 - 1.7 eV spectral region (Stoumpos *et al.*, 2013). Among the guanidinium perovskites studied, $GUASnI_3$ has an acceptable band gap in the range within the spectral region that supports its application in photovoltaics.

For further reference, the band structure estimation for the perovskite methylammonium lead iodide ($MAPbI_3$) (Fig. 25) was done using the same theoretical method employed to guanidinium perovskites. The $MAPbI_3$ band gap equal to 1.69 eV was estimated; in reasonable agreement with known theoretical results (Brivio *et al.*, 2014; Geng *et al.*, 2014; Quarti *et al.*, 2016; Umari *et al.*, 2014); and experimental value 1.65 eV (Quarti *et al.*, 2016). This agreement validates the computing approach utilized in this analysis. The band gap sequence in the series $MASnI_3$ 1.12 eV → $MAPbI_3$ 1.69 eV → $GUASnI_3$ 1.79 eV → $GUAPbI_3$ 1.92 eV (Dimesso *et al.*, 2016) shows that the band gap increases from Sn to Pb with the same cation as well as from MA to GUA for the same metal. It is seen from the band gap that, $GUASnI_3$ will behave like $MAPbI_3$ when the MA-cation in the tin halide perovskite is replaced with the GUA-cation (Fig. 26), a step forward in solving the toxicity issue of perovskites containing lead.

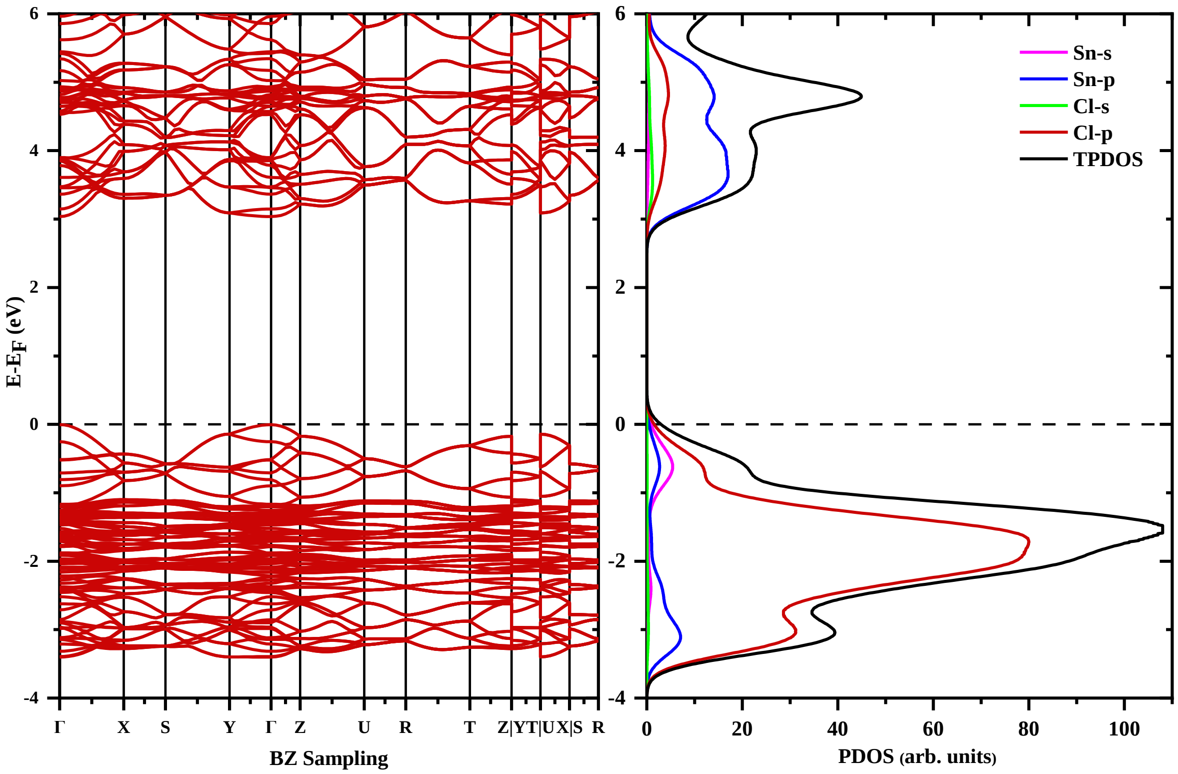

Figure 22: The band structure and PDOS of the $C(NH_2)_3SnCl_3$

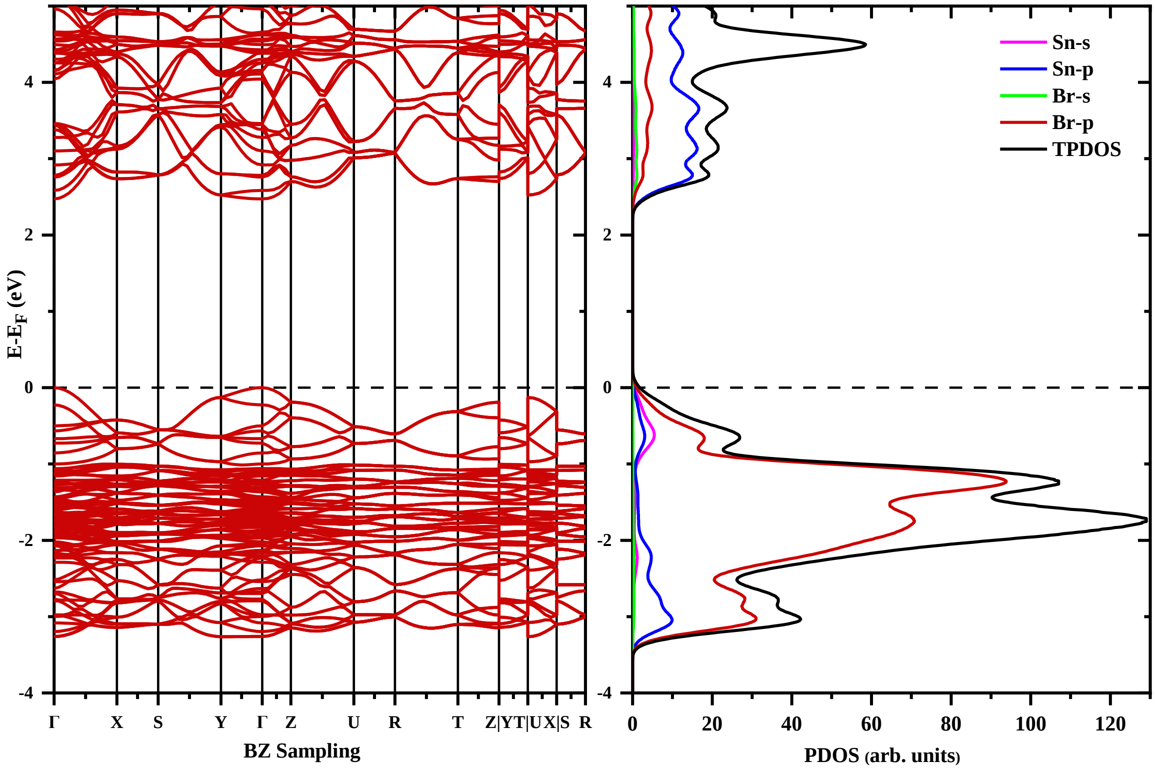

Figure 23: The band structure and PDOS of the $C(NH_2)_3SnBr_3$

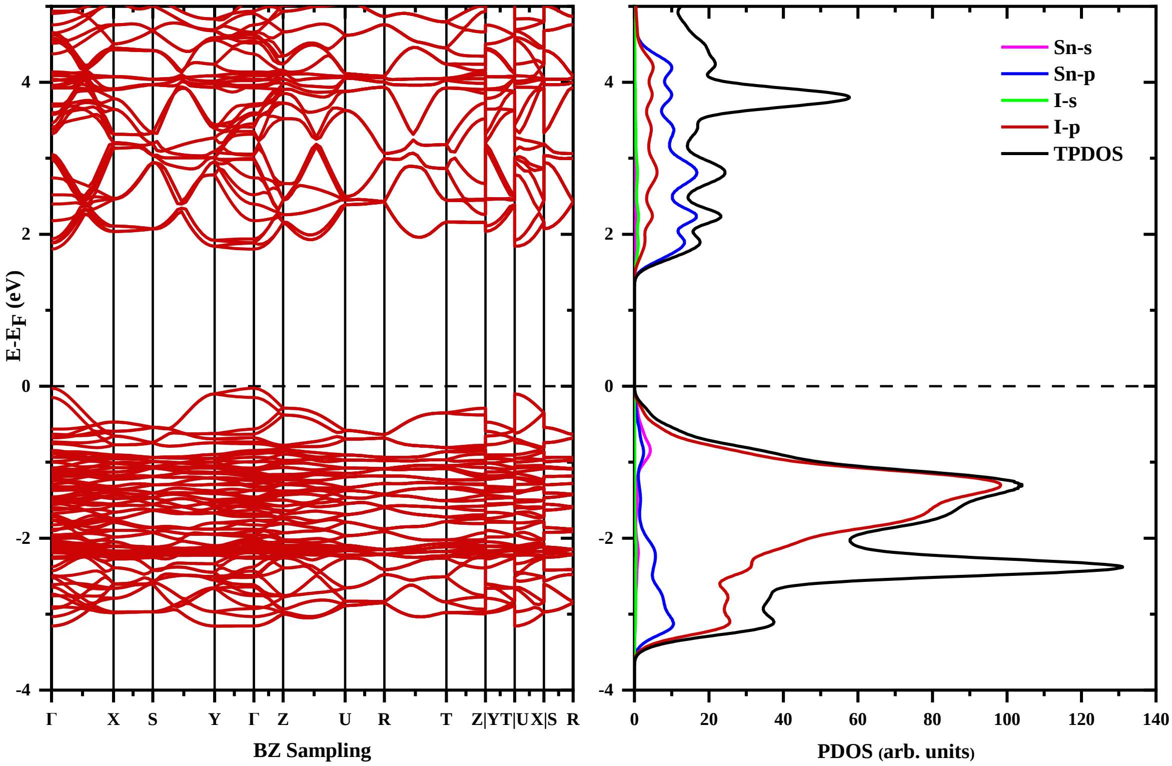

Figure 24: The band structure and PDOS of the $C(NH_2)_3SnI_3$

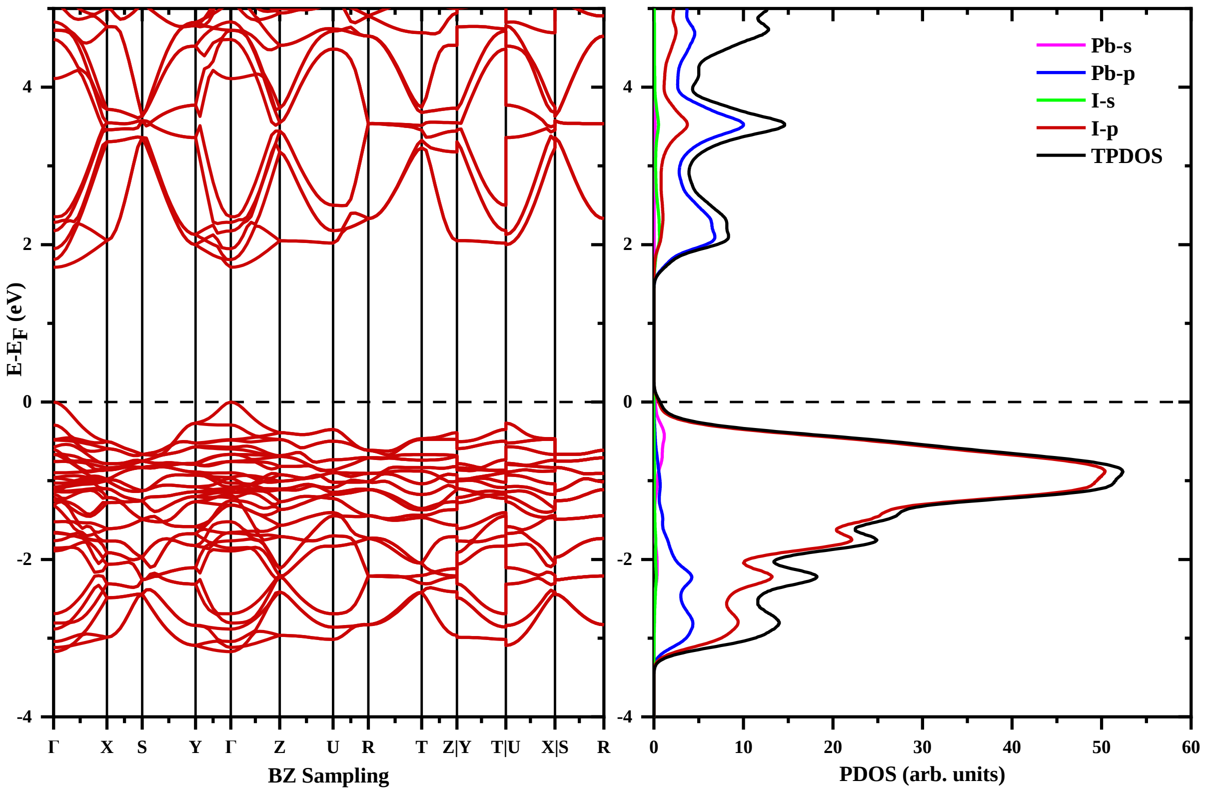

Figure 25: The band structure and PDOS of the $CH_3NH_3PbI_3$

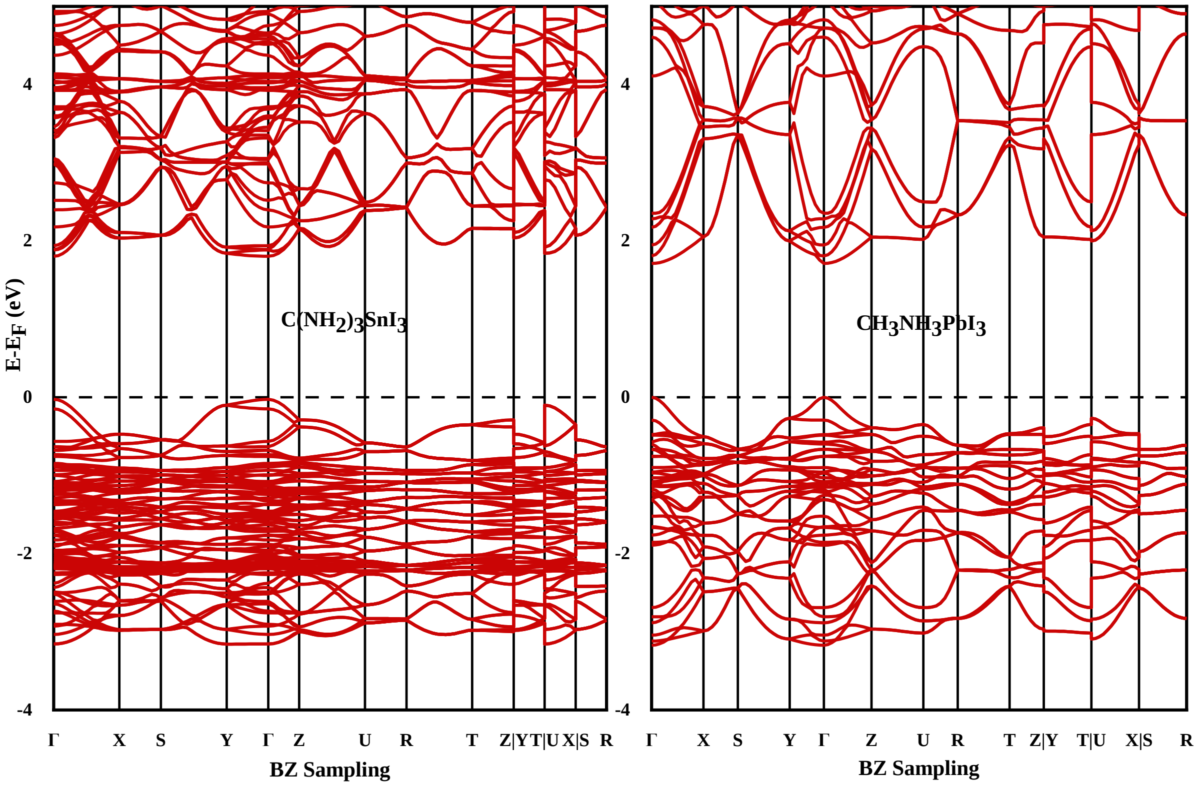

Figure 26: The band structures of $C(NH_2)_3SnI_3$ and $CH_3NH_3PbI_3$

When the perovskites are considered to be light-harvesting materials, the individual element states contributions are critical in favouring the electron-hole pairs spatial separation once photon absorption occurs, which may cause a longer lifetime of the charge carriers (Tuoc & Huan, 2020). Fig. 27-29 display the approximate projected densities of states with the contribution pattern of the s- and p-states of the halogens and Sn atoms. The atomic orbitals of tin and halogen show their individual contribution to the TPDOS of the perovskites. The s-states of the Sn atom are mostly located in the valence band (VB) with the p-states dominating in the conduction band (CB), clearly portrayed in Fig. 22-24; 27 and 28. On the other hand, VB is dominated by the p-states of the halogens, with the minimum contribution of the s-states in the valence and conduction bands (Fig. 22-24; 27). Therefore, in all compounds examined, the p-states of the halogens primarily apply to the VB while the Sn-p state dominates in the conduction band of the guanidinium halide perovskites.

The $GUASnI_3$ PDOS is compared to $MASnI_3$ and $MAPbI_3$ in Fig. 29. There is a correlation in contribution behaviour between the tin and lead states in the three perovskites, namely the p-states of the metals that are mainly active in the CB. Simultaneously, the contribution of the Sn atom in $GUASnI_3$ is higher than that of the lead p-state in $MAPbI_3$ (see insert in Fig. 29). Observations are consistent with those previously recorded for the $CH_3NH_3SnX_3$ (Sun *et al.*, 2016; Umari *et al.*, 2014) of the s- and p-state contributions of halogens and Sn atoms in $GUASnX_3$. Figure 30 summarizes the contribution of the states in $GUASnI_3$ and $MAPbI_3$ where it is clearly seen how the behaviour of Sn-states contribution changes when the GUA cation replaces the MA cation in the tin perovskites and its resemblance with Pb.

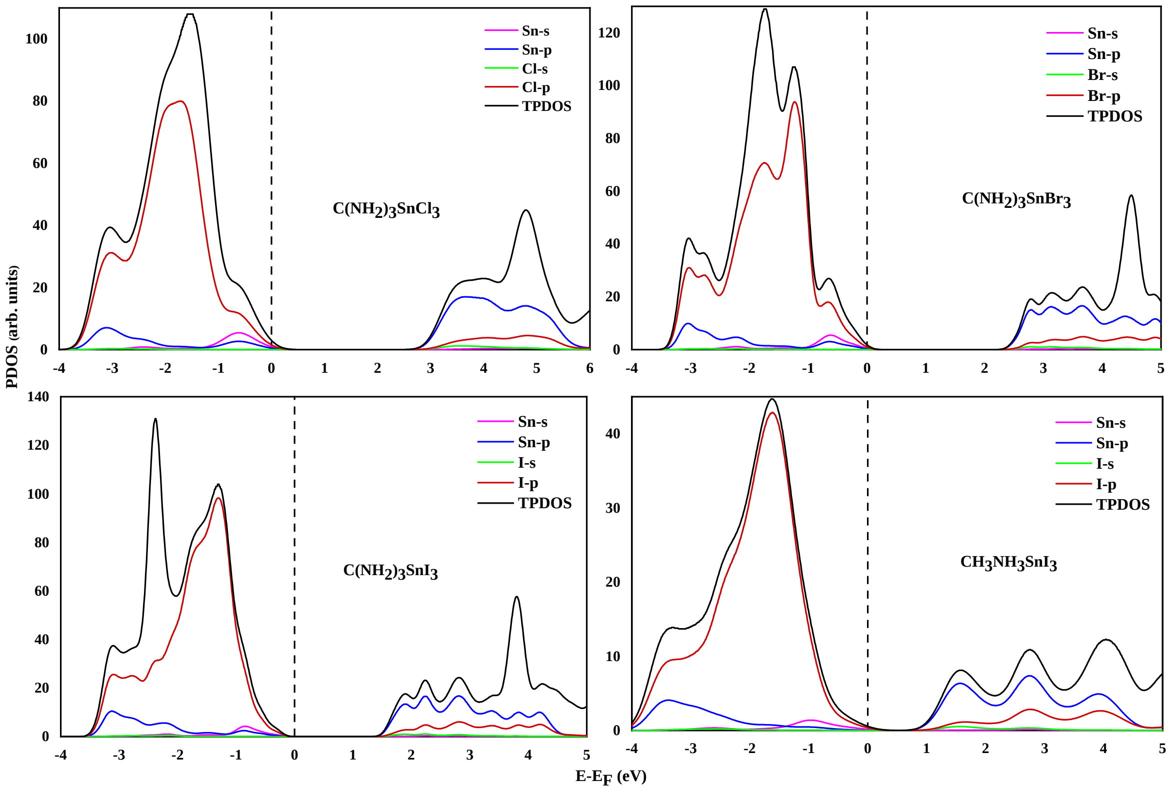

Figure 27: The projected density of states computed for the GUASnX_3 and MASnI_3 perovskites

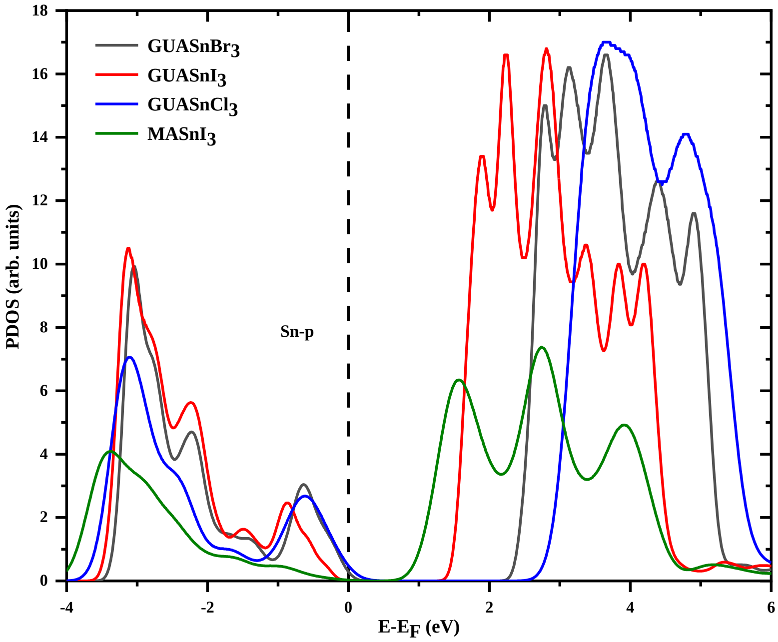

Figure 28: The contribution of the p-states of the tin atom to the VB and CB in the GUASnX_3 and MASnI_3 perovskites

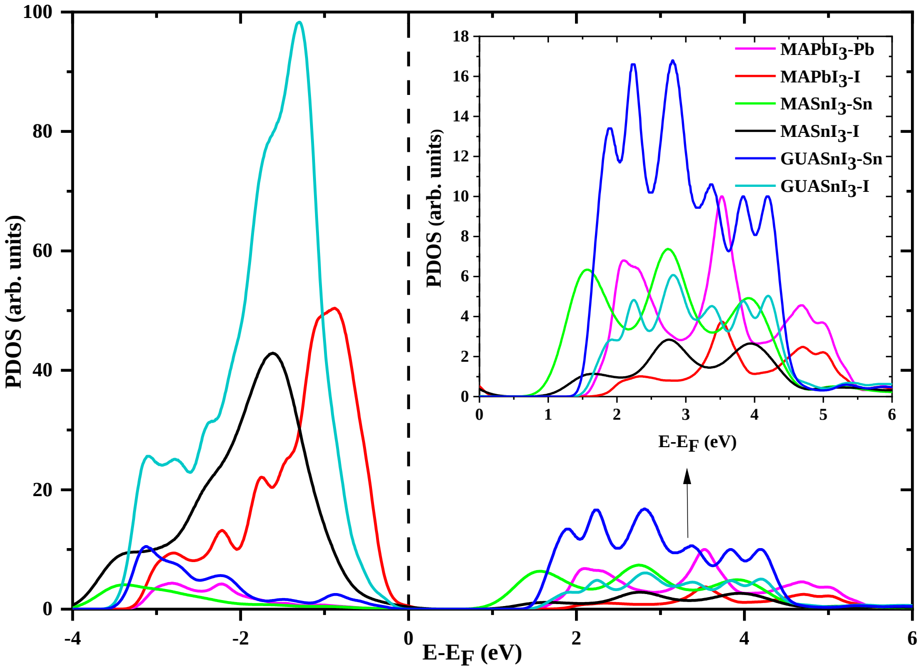

Figure 29: The contribution made by the p-states of the tin, lead, and iodine atoms to the VB and CB in the $GUASnI_3$, $MASnI_3$, and $MAPbI_3$ perovskites

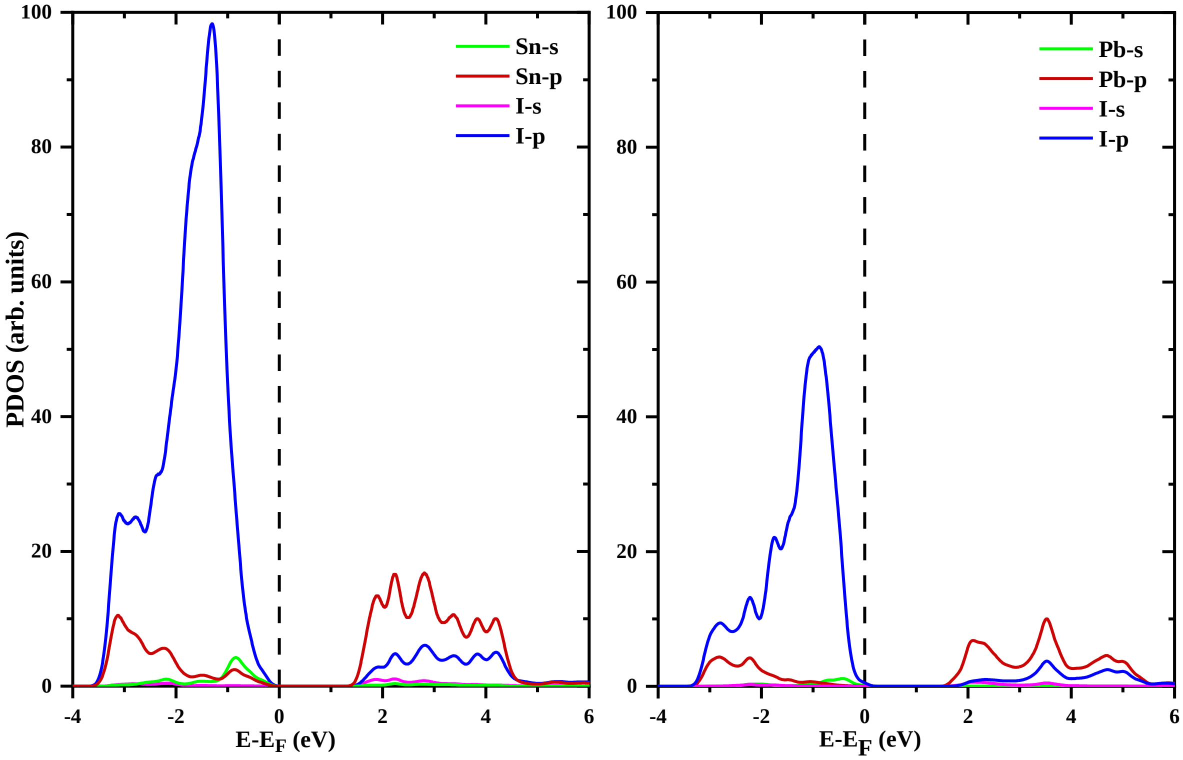

Figure 30: The contribution made by the s- and p-states of the tin, lead and iodine atoms to the VB and CB in the $GUASnI_3$ and $MAPbI_3$ perovskites

4.2.3 Thermodynamic Properties of $GUASnX_3$

The stability of perovskites is of significance for practical applications. High humidity and the tendency of converting to their halides (Nagabhushana *et al.*, 2016; Zhao & Park, 2015) can affect lead and tin halide perovskites' performance. In relation to various decomposition processes, material stability can be evaluated. In this study, the $GUASnX_3$ was decomposed into component products through R1-R3 channels and reaction energies were obtained with Equation 28. Complete reactant energies were measured at a theoretical level and indicated in Table 5. Enthalpies of reactions, $\Delta_r H°(298\ K)$ were accepted to be equal to reaction energies, $\Delta_r E$ values, i.e. the thermal and vibrational energy contributions were omitted. It is believed that the increment in enthalpy, $\Delta_r[H°(298)–H°(0)]$ is just a few kJ mol^{-1}; a similar assumption was made in Ciccioli and Latini's (Ciccioli & Latini, 2018) analysis of methylammonium lead perovskite.

Table 5: The total energies computed for the components of reaction R1-R3

System	$–E$, Ry
$Cl^–$, g	30.9881
$Br^–$, g	29.9741
$I^–$, g	33.4927
HCl, g	32.0599
HBr, g	31.0149
HI, g	34.5060
$SnCl_2$, s	224.9058
$SnBr_2$, s	222.8403
SnI_2, s	229.8336
CH_5N_3, g	79.7123
$C(NH_2)_3^+$, g	80.5638
$C(NH_2)_3Cl$, s	111.9733
$C(NH_2)_3Br$, s	110.9369
$C(NH_2)_3I$, s	114.4224
$C(NH_2)_3SnCl_3$, s	336.8908
$C(NH_2)_3SnBr_3$, s	333.7833
$C(NH_2)_3SnI_3$, s	344.2837

Table 6: The standard enthalpies of formation for products of decomposition reactions R1-R3

System	$-\Delta_f H°$(298 K), kJ mol^{-1}	Ref.
Cl^-, g	233.67	Gurvich *et al.* (1992
Br^-, g	219.03	*ibid*
I^-, g	195.04	*ibid*
HCl, g	92.31	*ibid*
HBr, g	36.29	*ibid*
HI, g	–26.50	*ibid*
$SnCl_2$, s	333	*ibid*
$SnBr_2$, s	253.60	*ibid*
SnI_2, s	153	*ibid*
CH_5N_3, g	–31.8	Marcus (2012)
$C(NH_2)_3^+$, g	–462.00 ± 3	*ibid*
$C(NH_2)_3Cl$, s	324.93±0.88	Matyushin *et al.* (1985)
$C(NH_2)_3Br$, s	278.7	This study
$C(NH_2)_3I$, s	213.2	*ibid*

Table 7: Enthalpies of reactions R1-R3 and calculated enthalpies of formation for $GUASnX_3$, in kJ mol^{-1}

	Reaction equation	$GUASnX_3$	$\Delta_r H°$ (298 K)	$-\Delta_f H°$ (298 K)
R1	$GUASnX_3$, s = GUAX, s + SnX_2, s	$GUASnCl_3$	15.4	673.3
		$GUASnBr_3$	7.9	540.2
		$GUASnI_3$	36.4	402.6
R2	$GUASnX_3$, s = SnX_2, s + HX, g + CH_5N_3, g	$GUASnCl_3$	279.5	673.0
		$GUASnBr_3$	283.3	541.4
		$GUASnI_3$	304.3	399.0
R3	$GUASnX_3$, s = SnX_2, s + X^-, g + GUA^+, g	$GUASnCl_3$	568.7	673.4
		$GUASnBr_3$	531.8	542.4
		$GUASnI_3$	516.7	402.7

The computed enthalpies of decomposition channels and enthalpies of formation of the $GUASnX_3$ are recorded in Table 7. Every decomposition route R1, R2, or R3 for $GUASnX_3$ has a unique heat effect; with reaction R1 having the smallest $\Delta_r H°$, thus being the most feasible, whereas the other two, R2 and R3, are highly endothermic with $\Delta_r H°$, ranging from 279 to 569 kJ mol^{-1}. The enthalpies of reactions for GUASnX$_3$ are displayed in Fig. 31; the MAPbX$_3$ data (Brunetti *et al.*, 2016; Ciccioli & Latini, 2018) is shown for comparison. The findings for the GUASnI$_3$ do not contradict to findings (Ciccioli & Latini, 2018) that the decomposition channel of MAPbX$_3$ into solid $CH_3NH_3X(s)$ and $PbX_2(s)$ products has also been shown to be the most viable in comparison to other paths. At the same time, when comparing the enthalpy trends in the Cl-Br-I sequence, they differ for the GUASnX$_3$ and MAPbX$_3$: the $\Delta_r H°$ values obtained vary from about 8 kJ mol^{-1} for GUASnCl$_3$ to 36 kJ mol^{-1} (GUASnI$_3$), while for the MAPbX$_3$, within the uncertainty limits, the experimental enthalpies of the decomposition reactions into solid constituents are almost equal to each other (Brunetti *et al.*, 2016; Ciccioli & Latini, 2018).

It was also thought that the formation of volatile products as a result of perovskites degradation was significant (Brunetti *et al.*, 2016; Ciccioli & Latini, 2018; Ivanov *et al.*, 2018). In this work, for the decay of GUASnX$_3$ into gaseous materials in R2, the enthalpies $\Delta_r H°$ decrease from I to Cl; that is, in accordance with experimental evidence of Knudsen effusion mass spectrometry (Brunetti *et al.*, 2016) calculated for the related reaction of methylammonium lead halide, $CH_3NH_3PbX_3(s)$ decomposition, $CH_3NH_3PbX_3(s) = CH_3NH_2(g) + PbX_2(s) + HX(g)$: 208.4 ± 10.9 kJ mol^{-1} (X = I), 207.8 ± 10.5 (X = Br), 190.4 ± 8.0 (X = Cl).

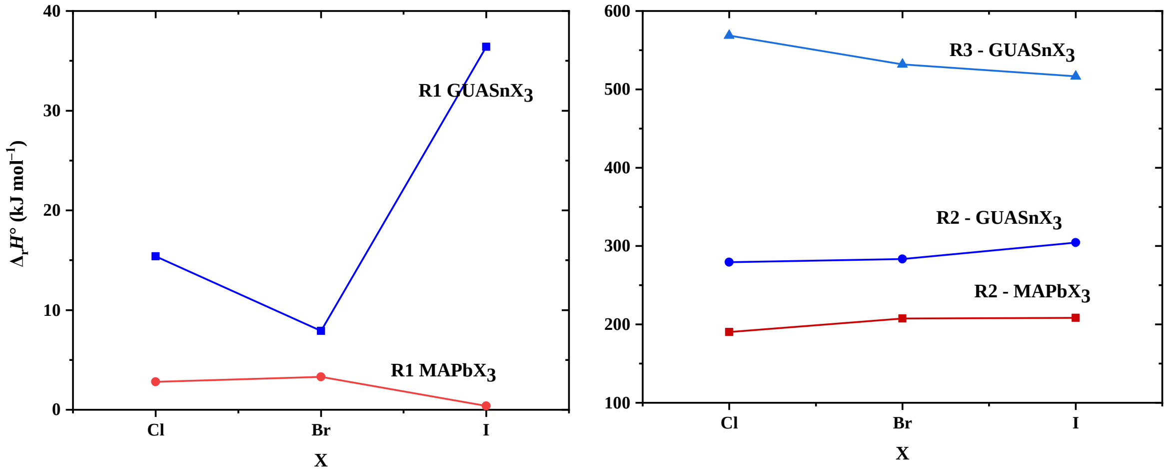

Figure 31: Enthalpies of decomposition reactions R1 (left), and R2, R3 (right) of the GUASnX$_3$ perovskites (our results), and MAPbX$_3$ (Brunetti *et al.*, 2016; Ciccioli & Latini, 2018)

The ionic decay products GUA$^+$ and X$^-$ are formed in reaction R3; the values of $\Delta_r H°$(R3) gradually decrease in series Cl-Br-I; this pattern is expectable since it normally occurs for the degradation of simple metal halides, e.g., SnX_2 or PbX_2. To summarize this analysis, the irregular Cl-Br-I pattern in the stability of the perovskites regarding the decomposition routes R1, R2, and R3 should be emphasized. The higher stability of the $GUASnI_3$ to the most feasible route R1 may be contributed by a steric factor when a greater size of iodine leads to tighter lattice packing that hinders the withdrawal of GUAI.

The enthalpies of the formation, $\Delta_f H°$(298 K) of the guanidinium tin halide perovskites were evaluated via each route using the $\Delta_r H°$ obtained (Table 7). The reference values for the standard enthalpies of formation of the reactions products were adopted from literature (Gurvich *et al.*, 1992; Marcus, 2012; Matyushin *et al.*, 1985) and listed in Table 6. As is shown, the values of $\Delta_f H°$(298 K) determined from these three reactions for each halide agree perfectly well with each other, indicating the reliability of the results. The average values of standard enthalpy of formation, $\Delta_f H°$ (298 K) are accepted for $GUASnCl_3$, $GUASnBr_3$, and $GUASnI_3$ as –673, –541, and –401 kJ mol^{-1}, respectively. For the $GUASnX_3$ in sequence Cl-Br-I, a gradual ascending of the enthalpy of formation, $\Delta_f H°$ is observed (Fig. 32); and it seemed to comply well with the experimental data that has been previously recorded for the lead halide perovskites $MAPbX_3$ (Brunetti *et al.*, 2016; Ciccioli & Latini, 2018; Ivanov *et al.*, 2018; Nagabhushana *et al.*, 2016). It should be noted that the enthalpies of formation of the $GUASnX_3$ and corresponding $MAPbX_3$ are very similar to each other. The perovskites plots have identical but steeper paths than those for the dihalides, SnX_2 and PbX_2, respectively. At the same time, relative to other substances, the line slope is smoother for the GUAX. It can also be observed that enthalpies of perovskite formation $GUASnX_3$ are nearly equal to the sum of all $\Delta_f H°$ values for SnX_2 and the respective GUAX. It suggests that the perovskite behaviour in the Cl–Br–I order is mainly determined by the metal dihalide, SnX_2 or PbX_2, while the effect of guanidine is less expressed.

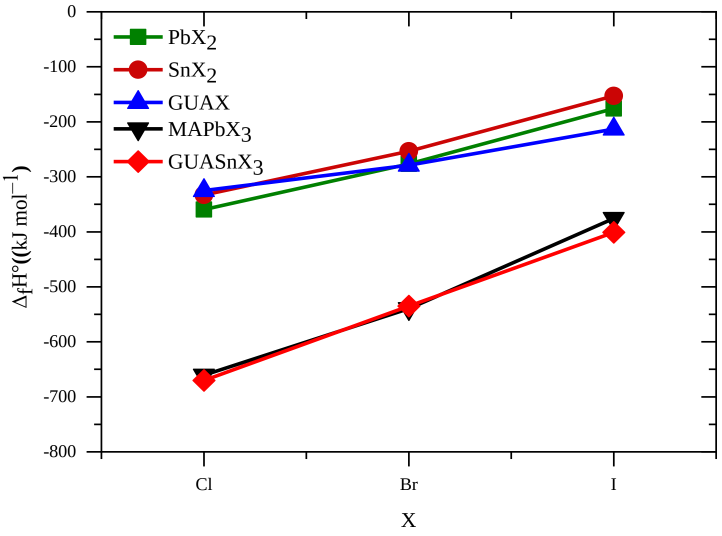

Figure 32: Trends in enthalpies of formation for PbX_2 (Gurvich *et al.*, 1992), SnX_2 (Gurvich *et al.*, 1992), GUAX (Matyushin *et al.*, 1985), $MAPbX_3$ (Brunetti *et al.*, 2016), and $GUASnX_3$ (this work)

4.3 $CH_3NH_3SnI_3/Cu_2O$ Interface Properties

The distinct PCE achieved by different synthetic methods for PSCs suggests the complexity and significance of the interface structure in the efficient separation of charges (Geng *et al.*, 2016). This implies that interactions at the interface are very complex and the mechanism of interfacial transmission of electrons remains unknown, so it is important to investigate the structural, electronic properties of different interfaces with perovskites. In this work, the interface of the $MASnI_3$ perovskite with the HTM Cu_2O is considered.

4.3.1 Structural Properties

The optimized structures of the $MASnI_3/Cu_2O$ interface for two cases, for Cu_2O on MAI and SnI_2, terminated surfaces, are presented in Fig. 33 and 34, respectively. The (001) surface of the $CH_3NH_3SnI_3$ perovskite considered in this analysis, includes the units SnI_2 and CH_3NH_3I which are constructed along the c direction (Fig. 10). The perovskite is composed of MAI and SnI_2 layers along the c axis, so the (001) perovskite slab has two types of terminations: the MAI termination with MA^+ and I^- ions (MAI−T), and SnI_2 termination with Sn^{2+} and I^- ions (SnI_2−T). Both the SnI_2 and MAI termination surfaces of $CH_3NH_3SnI_3$ were considered for electronic structure calculations in this study. The optimized cell parameters are listed in Table 8. The obtained lattice parameter for the cubic phase of Cu_2O (4.31 Å) has been overestimated when compared to the experimental value of 4.27 Å (Wang *et al.*, 2014). The overestimation and underestimation of electronic properties of semiconductors by DFT have been reported previously (Perdew *et al.*, 1981; Perdew *et al.*, 2017). For both the Cu_2O/MAI and Cu_2O/SnI_2 interfaces, O atoms are much closer to MAI or SnI_2 surface than to the Cu atoms (Figs. 33 and 34). The observed conformation infers the attractive and repulsive electrostatic interactions of the positively charged Cu with the negatively charged I and positively charged Sn on the $MASnI_3$ surfaces, respectively. A similar observation was made by Geng *et al.* (2016) on $MAPbI_3/TiO_2$ interface and Yang *et al.* (2018) on $MASnI_3/TiO_2$ interface where the O atoms of TiO_2 were closer to the perovskite surface than the Ti atoms leading to the breaking of the O-Ti bond due to interaction with the Pb and Sn atoms, respectively.

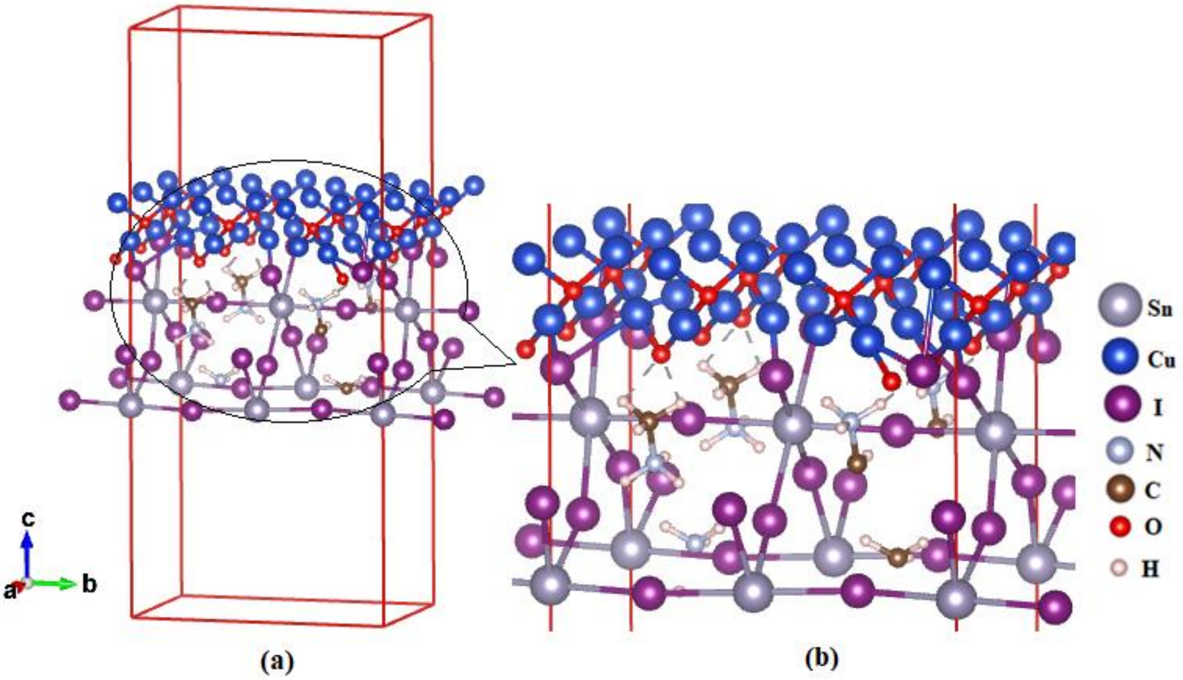

(a) (b)

Figure 33: The optimized structure of $MASnI_3/Cu_2O$ slab with MAI termination (a) and the interaction taking place at the surface portrayed by the Cu-I and H-O bonding (b)

Table 8: The optimized parameters for Cu_2O, $CH_3NH_3SnI_3$, and $CH_3NH_3SnI_3/Cu_2O$ slab

Material	Lattice parameters (Å)			Volume ($Å^3$)
	a	b	c	
Cu_2O	4.31	4.31	4.31	79.97
$CH_3NH_3SnI_3$	8.49	13.02	9.15	1011.44
$CH_3NH_3SnI_3$ / Cu_2O	8.49	13.02	29.15	3222.24

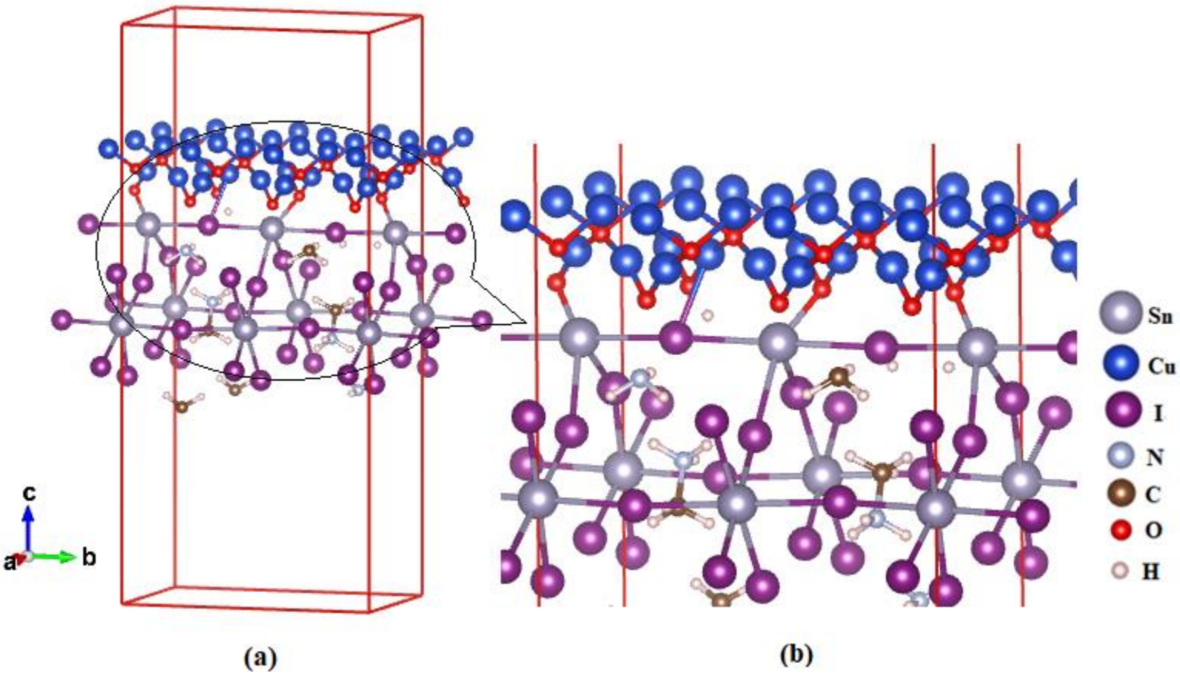

Figure 34: **The optimized structure of $MASnI_3/Cu_2O$ slab with SnI_2 termination (a) and the interaction taking place at the surface portrayed by the Sn-O and Cu-I bonding (b)**

The interaction between Cu_2O and the perovskite occurs mainly due to the perovskite iodine atoms and under-coordinated Cu atoms on the Cu_2O surface, as shown in Fig. 33 and 34. Table 9 displays the bonding properties of the $CH_3NH_3SnI_3$ perovskite/Cu_2O interface. Minor distortion of the structure is observed at the interface, such as change of the interlayer undercoordinated I atoms leading to surface SnI_6 octahedron distortion. The SnI_6 octahedron structure is the $CH_3NH_3SnI_3$ perovskite skeleton, and the bond angle Sn−I−Sn between the octahedrons of SnI_6 is very flexible, which may decrease to stabilize the structure when the phase changes; while the bond angle I−Sn−I within the octahedron of SnI_6 is rigid and it lies always around 180°. As previously pointed out by Geng *et al.* (2016), the I−Pb−I interface angle may decrease to about 174° relative to 176° in the interior; a behaviour observed in lead perovskites surfaces and the bulk of the tetragonal phase. A similar trend is clearly seen in Fig. 34 (a) where the I-Sn-I angle lying on direction b confirms the interface interaction. Interestingly for the SnI_2/Cu_2O system, the formation of O−Sn−O bonding is observed without breaking the Cu−O bond. There is a movement of the interfacial Sn atoms towards the perovskite which makes the Sn−O and the Cu−I bonds to shorten after optimization to 1.998 Å and 2.417 Å, respectively, a property that indicates a stronger interaction between the two surfaces. However, some of the Cu_2O interfacial O atoms rise slightly from the initial O−Cu bond broken to create a new O−H bond. Molecular parameters, internuclear distances

r_e and dissociation energies D_0, of diatomics SnI, CuI, SnO and CuO, (Krasnov *et al.*, 1979) are shown in Table 9 for comparison. It is seen that the Sn-O bond is stronger than Sn-I; this apparently favours the bond Sn-O forming, and thus the interface binding. At the same time, the parameters of the CuI and CuO molecules, where the Cu-I distance is longer than Cu-O, and the dissociation energies D_0 are comparable; indicate the interlayer interaction due to the formation of the new Cu-I bond is less probable, still, the hydrogen bond is expected to form (see Fig. 33). These speculations accord well with the study done by Castellanos-Águila *et al.* (2020) in which similar behaviour was observed for $MAPbI_3/Cu_2O$ interface where the Cu-O bonds were broken to create the O-H and Pb-O bonds enhancing interaction between the two surfaces.

Table 9: The bond lengths at the $MASnI_3/Cu_2O$ interface and parameters of diatomic molecules adopted from Krasnov *et al.* (1979).

Bonds	**Bond length, Å**		**In Diatomics**	
	Before optimization	**After optimization**	**r_e, Å**	**D_0, kcal/mol**
Sn-I	3.223	3.057	2.70	55±10
Cu-I	4.267	2.417	2.338	69±15
Sn-O	2.823	1.998	1.832	126±2
Cu-O	1.845	1.856	1.725	63±10
H-O	2.335	1.336		

4.3.2 Electronic Properties

The calculated electronic properties of the $MASnI_3/Cu_2O$ composite are listed in Table 10. The percentage analysis of the lattice mismatch between the two surfaces is less than 2% in magnitude with more than 98% lattice match signifying a good atom arrangement match between the perovskite and Cu_2O surfaces. The lattice match can be seen in optimized structures in Fig. 33 and 34 where all the interfacial atoms are involved in chemical bonding.

The Henkelman Group program (Tang *et al.*, 2009) was used to calculate the Bader atom charges (Bader & Laidig, 1990) for the analysis of spatial charge redistribution across the $MASnI_3/Cu_2O$ interfaces. The atomic Bader charge is defined as the total electrical charge (including that of the core electrons) of the atomic boundary, determined by the topological properties of the electron density. When the two components form an interface, there is a transfer of electrons from the $MASnI_3$ slab to the Cu_2O slab due to the difference in the Fermi levels between the perovskite and Cu_2O. This phenomenon leads to an electric field built-in from the perovskite to Cu_2O in contrary to the charge transfer making the interface to be at equilibrium. The charge transfer has been quantified as Bader charges, and the values obtained here are negative for both surface terminations, −0.063 for SnI_2-T/Cu_2O and −0.097 for MAI-T/Cu_2O, indicating the direction of charge transfer from the perovskite to Cu_2O for the SnI_2-T/Cu_2O and from the Cu_2O to the perovskite for the MAI-T/Cu_2O composite. The MAI-T/Cu_2O has weaker charge transfer compared to the SnI_2-T/Cu_2O interface which concludes a stronger capability of separation of hole-electron at the SnI_2-T/Cu_2O interface.

Table 10: The calculated binding energy, Bader charge and lattice mismatch at the interface

Interface	Bader Charge	Lattice mismatch (%)	Binding energy (eV)
CH_3NH_3I/Cu_2O	−0.097	−1.51(a); 0.69(b)	−3.63
SnI_2/Cu_2O	−0.063	−1.51(a); 0.69(b)	−5.94

The binding energy of the materials at the interface has been obtained using Equation 29. As it is reported in Table 10, the interface with SnI_2 termination is thermodynamically more stable than that with MAI-T by about 2.3 eV influenced by the type of interaction at the two surface terminations. The type of interaction existing between the MAI-ions of the MAI-T and other ions is either Van der Waals or hydrogen bonding which is weak resulting in small binding energy. On the other side, the Sn ions of the SnI_2-T interacts with the other atoms chemically connecting the perovskite and Cu_2O as a bridge. The same observation has been made by Geng *et al.,* 2016 on the analysis of the $MAPbI_3/TiO_2$ interface. From this study one can suppose that the relatively large binding energies obtained (3.63 and 5.94 eV) are attributed to the electrostatic Coulomb interaction which is larger compared to other bonding types like for example, in fullerene and zinc phthalocyanine (Qin *et al.*, 2020) on the surface of a perovskite. The intermolecular interactions are relatively small and only have a slight impact on the alignment of the energy levels. The calculated binding energy values obtained in present study indicate that the loss of energy did not affect the systems' energy as the lattice mismatch are all small to affect the interaction between the atoms at the surface.

CHAPTER FIVE

CONCLUSION AND RECOMMENDATIONS

5.1 Conclusion

Basing on the findings obtained, the following conclusions can be made:

(i) The structural, electronic, and thermodynamic properties for the orthorhombic phase of the methylammonium and guanidinium tin perovskites, $CH_3NH_3SnI_3$ and $GUASnX_3$, X= Cl, Br, I, have been studied. For the $MASnI_3$, various exchange-correlation functions LDA, PBE, and PBEsol have been considered; the PBE XC functional outperforms the other two with a band gap of 1.12 eV close to the experimental value, 1.2 eV. Similarly, band gaps of 3.00, 2.47 and 1.78 eV for $GUASnCl_3$, $GUASnBr_3$, $GUASnI_3$, respectively, have been obtained using the PBE XC functional.

(ii) The projected density of states analysis has shown that the p-states of the halogens primarily correspond to the valence bands of the $CH_3NH_3SnI_3$ and $GUASnX_3$, and the p-states of the tin atoms mainly participate in the materials' conduction bands, in consistency with results previously published for the $CH_3NH_3SnX_3$ perovskites.

(iii) Based on the thermodynamic approach, a stable low-temperature material has been reported for $MASnI_3$ perovskite that is in good accordance with the literature data on the phase transformations in the crystal. For the $GUASnX_3$ decomposition channels into solid and gaseous products, the $\Delta_r H°$ values did not always tend to change regularly in the series Cl – Br – I. The comparison of $GUASnX_3$ findings with the available experimental data for $MAPbX_3$ shows higher stability of the former in the related reactions as well as a certain similarity in the behaviour of the two perovskite groups.

(iv) The interface between the perovskite $MASnI_3$ and HTM Cu_2O has been investigated. Formation and breaking of bonds observed at the surface show that interaction occurs at the $MASnI_3/Cu_2O$ interface; the Sn-O, H-O, and Cu-I bonds are predicted to form.

(v) Through the analysis of the binding energy between $MASnI_3$ and Cu_2O, it can be concluded that Cu_2O can be a good candidate as a HTM for the $MASnI_3$ as the two components are expected to bind well in both SnI_2/Cu_2O and MAI/Cu_2O terminations.

5.2 Recommendations

This study recommends the following:

(i) Experimental work should be conducted to verify the electronic data obtained for $GUASnX_3$ materials and test their application in the solar cells. Some methods for preparation and characterization of perovskite materials are reported in appendices 4 and 5 respectively.

(ii) A high-performance computer (HPC) with at least 100 cores should be used to study the band gap, density of states and other electronic properties at the interface between $MASnI_3$ and Cu_2O. The study of the interface characteristics can be extended to the interface of $MASnI_3$ with other HTM like NiO, CuSCN, and others which have shown high PSC power conversion efficiency with $MAPbI_3$.

(iii) For $GUASnX_3$, optical properties can be computed to analyze the spectroscopic behaviour of the materials.

(iv) The interface between tin guanidinium halide perovskites and HTMs can also be considered and the electronic properties can be computed.

(v) Based on the $GUASnX_3$ full cell structure with all components can be modelled to analyze the electronic properties and power conversion efficiency of the solar cells.

(vi) The area of this research, solid-state matter, is a very complicated branch of Physics and Chemistry and requires good basic knowledge and profound computer skills so, the study recommends that, one should get familiarized with the theoretical aspect of it before experimentation or computation for better understanding of what is being done and easier the whole process of interpretation of the results.

REFERENCES

Abate, A., Saliba, M., Hollman, D. J., Stranks, S. D., Wojciechowski, K., Avolio, R., Grancini, G., Petrozza, A., & Snaith, H. J. (2014). Supramolecular halogen bond passivation of organic-inorganic halide perovskite solar cells. *Nano Letters*, *14*(6), 3247-3254.

Adamo, C., & Barone, V. (1999). Toward reliable density functional methods without adjustable parameters: the PBE0 model. *The Journal of Chemical Physics*, *110*(13), 6158-6170.

Adamo, C., Scuseria, G. E., & Barone, V. (1999). Accurate excitation energies from time-dependent density functional theory: assessing the PBE0 model. *The Journal of Chemical Physics*, *111*(7), 2889-2899.

Agiorgousis, M. L., Sun, Y. Y., Zeng, H., & Zhang, S. (2014). Strong covalency-induced recombination centers in perovskite solar cell material $CH_3NH_3PbI_3$. *Journal of the American Chemical Society*, *136*(41), 14570-14575.

Ahn, N., Son, D. Y., Jang, I. H., Kang, S. M., Choi, M., & Park, N. G. (2015). Highly reproducible perovskite solar cells with average efficiency of 18.3% and best efficiency of 19.7% fabricated via Lewis base adduct of lead (II) iodide. *Journal of the American Chemical Society*, *137*(27), 8696-8699.

Anaraki, E. H., Kermanpur, A., Steier, L., Domanski, K., Matsui, T., Tress, W., Saliba, M., Abate, A., Grätzel, M., & Hagfeldt, A. (2016). Highly efficient and stable planar perovskite solar cells by solution-processed tin oxide. *Energy & Environmental Science*, *9*(10), 3128-3134.

Angell, C., Sheppard, N., Yamaguchi, A., Shimanouchi, T., Miyazawa, T., & Mizushima, S. (1957). The infra-red spectrum, structure, and normal vibrations of the guanidinium ion. *Transactions of the Faraday Society*, *53*, 589-600.

Ashcroft, N. W., & Mermin, N. D. (1976). *Solid State Physics*. New York: Holt, Rinehart and Winston.

Bader, R. F. W., & Laidig, K. F. (1990). Analysis and classification of the charge distribution using quantum mechanics. *Transactions of the American Crystallographic Association*, 26, 1-21.

Baena, J. P. C., Steier, L., Tress, W., Saliba, M., Neutzner, S., Matsui, T., Giordano, F., Jacobsson, T. J., Kandada, A. R. S., & Zakeeruddin, S. M. (2015). Highly efficient planar perovskite solar cells through band alignment engineering. *Energy & Environmental Science, 8*(10), 2928-2934.

Baranwal, A. K., Masutani, H., Sugita, H., Kanda, H., Kanaya, S., Shibayama, N., Sanehira, Y., Ikegami, M., Numata, Y., & Yamada, K. (2017). Lead-free perovskite solar cells using Sb and Bi-based $A_3B_2X_9$ and A_3BX_6 crystals with normal and inverse cell structures. *Nano convergence*, *4*(1), 1-14.

Baroni, S., Giannozzi, P., & Testa, A. (1987). Green's-function approach to linear response in solids. *Physical Review Letters*, *58*(18), 1861-1864.

Becke, A. D. (1997). Density-functional thermochemistry. V. Systematic optimization of exchange-correlation functionals. *The Journal of Chemical Physics*, *107*(20), 8554-8560.

Bera, A., Wu, K., Sheikh, A., Alarousu, E., Mohammed, O. F., & Wu, T. (2014). Perovskite oxide $SrTiO_3$ as an efficient electron transporter for hybrid perovskite solar cells. *The Journal of Physical Chemistry C, 118*(49), 28494-28501.

Berhe, T. A., Su, W. N., Chen, C. H., Pan, C. J., Cheng, J. H., Chen, H. M., Tsai, M. C., Chen, L. Y., Dubale, A. A., & Hwang, B. J. (2016). Organometal halide perovskite solar cells: degradation and stability. *Energy & Environmental Science*, *9*(2), 323-356.

Bi, D., Moon, S. J., Häggman, L., Boschloo, G., Yang, L., Johansson, E. M., Nazeeruddin, M. K., Grätzel, M., & Hagfeldt, A. (2013). Using a two-step deposition technique to prepare perovskite ($CH_3NH_3PbI_3$) for thin film solar cells based on ZrO_2 and TiO_2 mesostructures. *RSC Advances*, *3*(41), 18762-18766.

Borriello, I., Cantele, G., & Ninno, D. (2008). Ab initio investigation of hybrid organic-inorganic perovskites based on tin halides. *Physical Review B*, *77*(23), 1-9.

Bowen, T., del Ninno, C., Andrews, C., Coll-Black, S., Gentilini, U., Johnson, K., Kawasoe, Y., Kryeziu, A., Maher, B., & Williams, A. (2020). *Tracking SDG 7: The Energy Progress Report 2020.* https://openknowledge.worldbank.org/bitstream/handle/-10986/33822/148874.pdf?sequence=2&isAllowed=y.

Brivio, F. (2016). *Atomistic modelling of perovskite solar cells*. University of Bath.

Brivio, F., Butler, K. T., Walsh, A., & Van Schilfgaarde, M. (2014). Relativistic quasiparticle self-consistent electronic structure of hybrid halide perovskite photovoltaic absorbers. *Physical Review B, 89*(15), 1-6.

Brunetti, B., Cavallo, C., Ciccioli, A., Gigli, G., & Latini, A. (2016). On the thermal and thermodynamic (in) stability of methylammonium lead halide perovskites. *Scientific Reports*, *6*, 1-12.

Buin, A., Comin, R., Xu, J., Ip, A. H., & Sargent, E. H. (2015). Halide-dependent electronic structure of organolead perovskite materials. *Chemistry of Materials*, *27*(12), 4405-4412.

Burschka, J., Pellet, N., Moon, S. J., Humphry-Baker, R., Gao, P., Nazeeruddin, M. K., & Grätzel, M. (2013). Sequential deposition as a route to high-performance perovskite-sensitized solar cells. *Nature, 499*(7458), 316-319.

Calio, L., Kazim, S., Graetzel, M., & Ahmad, S. (2016). Hole-transport materials for perovskite solar cells. *Angewandte Chemie International Edition*, *55*(47), 14522-14545.

Carnie, M. J., Charbonneau, C., Davies, M. L., Troughton, J., Watson, T. M., Wojciechowski, K., Snaith, H., & Worsley, D. A. (2013). A one-step low temperature processing route for organolead halide perovskite solar cells. *Chemical Communications*, *49*(72), 7893-7895.

Castellanos-Águila, J. E., Lodeiro, L., Menendez-Proupin, E., Montero-Alejo, A. L., Palacios, P., Conesa, J. C., & Wahnón, P. (2020). Atomic-scale model and electronic structure of $Cu_2O/CH_3NH_3PbI_3$ interfaces in perovskite solar cells. *ACS Applied Materials & Interfaces*, *12*(40), 44648-44657.

Ceperley, D., & Alder, B. (1980). Exchange-correlation potential and energy for density-functional calculation. *Physical Review Letters*, *45*, 567-581.

Chaudhary, S., Gupta, S. K., & Negi, C. M. S. (2020). Enhanced performance of perovskite photodetectors fabricated by two-step spin coating approach. *Materials Science in Semiconductor Processing*, *109*, 1-8.

Chen, Q., Zhou, H., Hong, Z., Luo, S., Duan, H. S., Wang, H. H., Liu, Y., Li, G., & Yang, Y. (2014). Planar heterojunction perovskite solar cells via vapor-assisted solution process. *Journal of the American Chemical Society*, *136*(2), 622-625.

Chiarella, F., Zappettini, A., Licci, F., Borriello, I., Cantele, G., Ninno, D., Cassinese, A., & Vaglio, R. (2008). Combined experimental and theoretical investigation of optical, structural, and electronic properties of $CH_3NH_3SnX_3$ thin films (X= Cl, Br). *Physical Review B*, *77*(4), 1-6.

Ciccioli, A., & Latini, A. (2018). Thermodynamics and the intrinsic stability of lead halide perovskites $CH_3NH_3PbX_3$. *The Journal of Physical Chemistry Letters*, *9*(13), 3756-3765.

Colella, S., Mosconi, E., Fedeli, P., Listorti, A., Gazza, F., Orlandi, F., Ferro, P., Besagni, T., Rizzo, A., & Calestani, G. (2013). $MAPbI_{3-x}Cl_x$ mixed halide perovskite for hybrid solar cells: the role of chloride as dopant on the transport and structural properties. *Chemistry of Materials*, *25*(22), 4613-4618.

Conings, B., Baeten, L., De Dobbelaere, C., D'Haen, J., Manca, J., & Boyen, H. G. (2014). Perovskite-based hybrid solar cells exceeding 10% efficiency with high reproducibility using a thin film sandwich approach. *Advanced Materials*, *26*(13), 2041-2046.

Costa, R., Pogrebnoi, A., & Pogrebnaya, T. (2021). Betanidin isomerisation and decarboxylation, thermodynamic and charge transfer dye properties towards dye sensitised solar cells application. *Journal of Physical Organic Chemistry*, *34*(6), 1-25.

Cramer, C. J. (2013). *Essentials of computational chemistry: theories and models*. John Wiley & Sons.

Dal Corso, A. (2014). Pseudopotentials periodic table: From H to Pu. *Computational Materials Science*, *95*, 337-350.

Deogratias, G., Seriani, N., Pogrebnaya, T., & Pogrebnoi, A. (2020). Tuning optoelectronic properties of triphenylamine based dyes through variation of pi-conjugated units and anchoring groups: A DFT/TD-DFT investigation. *Journal of Molecular Graphics and Modelling*, *94*, 1-13.

Dimesso, L., Quintilla, A., Kim, Y.M., Lemmer, U., & Jaegermann, W. (2016). Investigation of formamidinium and guanidinium lead tri-iodide powders as precursors for solar cells. *Materials Science and Engineering: B*, *204*, 27-33.

Divitini, G., Cacovich, S., Matteocci, F., Cinà, L., Di Carlo, A., & Ducati, C. (2016). In situ observation of heat-induced degradation of perovskite solar cells. *Nature Energy*, *1*(2), 1-6.

Dong, H., Guo, X., Li, W., & Wang, L. (2014). Cesium carbonate as a surface modification material for organic-inorganic hybrid perovskite solar cells with enhanced performance. *RSC Advances*, *4*(104), 60131-60134.

Dong, X., Hu, H., Lin, B., Ding, J., & Yuan, N. (2014). The effect of ALD-ZnO layers on the formation of $CH_3NH_3PbI_3$ with different perovskite precursors and sintering temperatures. *Chemical Communications*, *50*(92), 14405-14408.

EIA. (2020). *Annual Energy Outlook 2020 with projections to 2050* (AEO2020). Washington.

Eperon, G. E., Burlakov, V. M., Docampo, P., Goriely, A., & Snaith, H. J. (2014). Morphological control for high performance, solution-processed planar heterojunction perovskite solar cells. *Advanced Functional Materials*, *24*(1), 151-157.

Even, J., Pedesseau, L., Jancu, J. M., & Katan, C. (2013). Importance of spin-orbit coupling in hybrid organic/inorganic perovskites for photovoltaic applications. *The Journal of Physical Chemistry Letters*, *4*(17), 2999-3005.

Even, J., Pedesseau, L., Jancu, J. M., & Katan, C. (2014). DFT and k.p modelling of the phase transitions of lead and tin halide perovskites for photovoltaic cells. *Physica Status Solidi (RRL)-Rapid Research Letters*, *8*(1), 31-35.

Fakharuddin, A., De Rossi, F., Watson, T. M., Schmidt-Mende, L., & Jose, R. (2016). Research update: Behind the high efficiency of hybrid perovskite solar cells. *APL Materials*, *4*(9), 1-16.

Fan, Z., Xiao, J., Sun, K., Chen, L., Hu, Y., Ouyang, J., Ong, K. P., Zeng, K., & Wang, J. (2015). Ferroelectricity of $CH_3NH_3PbI_3$ perovskite. *The Journal of Physical Chemistry Letters*, *6*(7), 1155-1161.

Feng, J., & Xiao, B. (2014). Effective masses and electronic and optical properties of nontoxic $MASnX_3$ (X= Cl, Br, and I) perovskite structures as solar cell absorber: a theoretical study using HSE06. *The Journal of Physical Chemistry C*, *118*(34), 19655-19660.

Frost, J. M., Butler, K. T., Brivio, F., Hendon, C. H., Van Schilfgaarde, M., & Walsh, A. (2014). Atomistic origins of high-performance in hybrid halide perovskite solar cells. *Nano Letters*, *14*(5), 2584-2590.

Frost, J. M., & Walsh, A. (2016). What is moving in hybrid halide perovskite solar cells? *Accounts of Chemical Research*, *49*(3), 528-535.

Fu, L., Li, B., Li, S., & Yin, L. (2020). *Future Challenges of the Perovskite Materials. In Revolution of Perovskite* (pp. 315-320). Springer.

Gaml, E. A., Dubey, A., Reza, K. M., Hasan, M. N., Adhikari, N., Elbohy, H., Bahrami, B., Zeyada, H., Yang, S., & Qiao, Q. (2017). Alternative benzodithiophene (BDT) based polymeric hole transport layer for efficient perovskite solar cells. *Solar Energy Materials and Solar Cells, 168,* 8-13.

Geng, W., Tong, C. J., Liu, J., Zhu, W., Lau, W. M., & Liu, L. M. (2016). Structures and electronic properties of different $CH_3NH_3PbI_3/TiO_2$ interface: a first-principles study. *Scientific Reports*, *6*(1), 1-8.

Geng, W., Zhang, L., Zhang, Y. N., Lau, W. M., & Liu, L. M. (2014). First-principles study of lead iodide perovskite tetragonal and orthorhombic phases for photovoltaics. *The Journal of Physical Chemistry C*, *118*(34), 19565-19571.

Giannozzi, P., Andreussi, O., Brumme, T., Bunau, O., Nardelli, M. B., Calandra, M., Car, R., Cavazzoni, C., Ceresoli, D., & Cococcioni, M. (2017). Advanced capabilities for materials modelling with Quantum ESPRESSO. *Journal of Physics: Condensed Matter*, *29*(46), 1-30.

Giannozzi, P., Baroni, S., Bonini, N., Calandra, M., Car, R., Cavazzoni, C., Ceresoli, D., Chiarotti, G. L., Cococcioni, M., & Dabo, I. (2009). Quantum ESPRESSO: A modular and open-source software project for quantum simulations of materials. *Journal of Physics: Condensed Matter*, *21*(39), 1-19.

Goldschmidt, V. (1927). Crystal structure and chemical correlation. *Berichte der Deutschen Chemischen Gesellschaft*, *60*, 1263-1296.

Grancini, G., Roldán-Carmona, C., Zimmermann, I., Mosconi, E., Lee, X., Martineau, D., Narbey, S., Oswald, F., De Angelis, F., & Graetzel, M. (2017). One-year stable perovskite solar cells by 2D/3D interface engineering. *Nature Communications*, *8*(1), 1-8.

Gražulis, S., Chateigner, D., Downs, R. T., Yokochi, A., Quirós, M., Lutterotti, L., Manakova, E., Butkus, J., Moeck, P., & Le Bail, A. (2009). Crystallography Open Database: an open-access collection of crystal structures. *Journal of Applied Crystallography*, *42*(4), 726-729.

Guo, Y., Lei, H., Xiong, L., Li, B., & Fang, G. (2018). An integrated organic-inorganic hole transport layer for efficient and stable perovskite solar cells. *Journal of Materials Chemistry A*, *6*(5), 2157-2165.

Gurvich, L., Yungman, V., Bergman, G., Veitz, I., Gusarov, A., Iorish, V., Leonidov, V. Y., Medvedev, V., Belov, G., & Aristova, N. (1992). *Thermodynamic Properties of individual Substances. Ivtanthermo for Windows Database on Thermodynamic Properties of Individual Substances and Thermodynamic Modeling Software. In (Vol. Version 3.0).* Moscow: Glushko Thermocenter of RAS.

Habisreutinger, S. N., Leijtens, T., Eperon, G. E., Stranks, S. D., Nicholas, R. J., & Snaith, H. J. (2014). Carbon nanotube/polymer composites as a highly stable hole collection layer in perovskite solar cells. *Nano Letters*, *14*(10), 5561-5568.

Haider, S. Z., Anwar, H., Jamil, Y., & Shahid, M. (2020). A comparative study of interface engineering with different hole transport materials for high-performance perovskite solar cells. *Journal of Physics and Chemistry of Solids*, *136*, 1-11.

Hailegnaw, B., Kirmayer, S., Edri, E., Hodes, G., & Cahen, D. (2015). Rain on methylammonium lead iodide based perovskites: possible environmental effects of perovskite solar cells. *The Journal of Physical Chemistry Letters*, *6*(9), 1543-1547.

Hanwell, M. D., Curtis, D. E., Lonie, D. C., Vandermeersch, T., Zurek, E., & Hutchison, G. R. (2012). Avogadro: an advanced semantic chemical editor, visualization, and analysis platform. *Journal of Cheminformatics*, *4*(1), 1-17.

Hao, F., Stoumpos, C. C., Cao, D. H., Chang, R. P., & Kanatzidis, M. G. (2014). Lead-free solid-state organic-inorganic halide perovskite solar cells. *Nature Photonics*, *8*(6), 1-6.

Hautier, G., Fischer, C., Ehrlacher, V., Jain, A., & Ceder, G. (2011). Data mined ionic substitutions for the discovery of new compounds. *Inorganic Chemistry*, *50*(2), 656-663.

Hawash, Z., Ono, L. K., & Qi, Y. (2018). Recent advances in spiro-MeOTAD hole transport material and its applications in organic-inorganic halide perovskite solar cells. *Advanced Materials Interfaces*, *5*(1), 1-22.

Haynes, P. (1998). *Linear-scaling methods in ab initio quantum-mechanical calculations*. University of Cambridge.

Hedin, L. (1965). New method for calculating the one-particle Green's function with application to the electron-gas problem. *Physical Review*, *139*(3A), A796-A823.

Heo, J. H., Han, H. J., Kim, D., Ahn, T. K., & Im, S. H. (2015). Hysteresis-less inverted $CH_3NH_3PbI_3$ planar perovskite hybrid solar cells with 18.1% power conversion efficiency. *Energy & Environmental Science*, *8*(5), 1602-1608.

Heyd, J., Scuseria, G. E., & Ernzerhof, M. (2003). Hybrid functionals based on a screened Coulomb potential. *The Journal of Chemical Physics*, *118*(18), 8207-8215.

Hinuma, Y., Pizzi, G., Kumagai, Y., Oba, F., & Tanaka, I. (2017). Band structure diagram paths based on crystallography. *Computational Materials Science*, *128*, 140-184.

Hoefler, S. F., Trimmel, G., & Rath, T. (2017). Progress on lead-free metal halide perovskites for photovoltaic applications: a review. *Monatshefte für Chemie-Chemical Monthly*, *148*(5), 795-826.

Huang, F., Jiang, L., Pascoe, A. R., Yan, Y., Bach, U., Spiccia, L., & Cheng, Y.B. (2016). Fatigue behavior of planar $CH_3NH_3PbI_3$ perovskite solar cells revealed by light on/off diurnal cycling. *Nano Energy*, *27*, 509-514.

Huang, Y., Su, J., Li, Q., Wang, D., Xu, L., & Bai, Y. (2019). Structure, optical and electrical properties of $CH_3NH_3SnI_3$ single crystal. *Physica B: Condensed Matter*, *563*, 107-112.

Hwang, I., Jeong, I., Lee, J., Ko, M. J., & Yong, K. (2015). Enhancing stability of perovskite solar cells to moisture by the facile hydrophobic passivation. *ACS Applied Materials & Interfaces*, *7*(31), 17330-17336.

IEA. (2020). *Snapshot of Global PV Markets: Photovoltaic Power Systems Programme*. https://iea-pvps.org/wp-content/uploads/2020/04/IEA_PVPS_Snapshot_2020.pdf

Ivanov, I., Steparuk, A., Bolyachkina, M., Tsvetkov, D., Safronov, A., & Zuev, A. Y. (2018). Thermodynamics of formation of hybrid perovskite-type methylammonium lead halides. *The Journal of Chemical Thermodynamics*, *116*, 253-258.

Jain, A., Ong, S. P., Hautier, G., Chen, W., Richards, W. D., Dacek, S., Cholia, S., Gunter, D., Skinner, D., & Ceder, G. (2013). Commentary: The Materials Project: A materials genome approach to accelerating materials innovation. *APL Materials*, *1*(1), 1-11.

Jayan, K. D., & Sebastian, V. (2021). Comprehensive device modelling and performance analysis of MASnI3 based perovskite solar cells with diverse ETM, HTM and back metal contacts. *Solar Energy*, *217*, 40-48.

Jean, J., Brown, P. R., Jaffe, R. L., Buonassisi, T., & Bulović, V. (2015). Pathways for solar photovoltaics. *Energy & Environmental Science*, *8*(4), 1200-1219.

Jeng, J. Y., Chiang, Y. F., Lee, M. H., Peng, S. R., Guo, T. F., Chen, P., & Wen, T. C. (2013). $CH_3NH_3PbI_3$ perovskite/fullerene planar-heterojunction hybrid solar cells. *Advanced Materials*, *25*(27), 3727-3732.

Jensen, F. (2017). *Introduction to computational chemistry*. John Wiley & Sons.

Jeon, N. J., Noh, J. H., Yang, W. S., Kim, Y. C., Ryu, S., Seo, J., & Seok, S. I. (2015). Compositional engineering of perovskite materials for high-performance solar cells. *Nature*, *517*(7535), 1-5.

Jia, J., Dong, J., Wu, J., Wei, H., & Cao, B. (2020). Combustion procedure deposited SnO_2 electron transport layers for high efficient perovskite solar cells. *Journal of Alloys and Compounds*, 1-11.

Jiang, F., Yang, D., Jiang, Y., Liu, T., Zhao, X., Ming, Y., Luo, B., Qin, F., Fan, J., & Han, H. (2018). Chlorine-incorporation-induced formation of the layered phase for antimony-based lead-free perovskite solar cells. *Journal of the American Chemical Society*, *140*(3), 1019-1027.

Jiang, Q., Zhang, X., & You, J. (2018). SnO_2: a wonderful electron transport layer for perovskite solar cells. *Small*, *14*(31), 1-14.

Jodlowski, A. D., Roldán-Carmona, C., Grancini, G., Salado, M., Ralaiarisoa, M., Ahmad, S., Koch, N., Camacho, L., De Miguel, G., & Nazeeruddin, M. K. (2017). Large guanidinium cation mixed with methylammonium in lead iodide perovskites for 19% efficient solar cells. *Nature Energy*, *2*(12), 972-979.

Jung, M., Kim, Y. C., Jeon, N. J., Yang, W. S., Seo, J., Noh, J. H., & Seok, S. I. (2016). Thermal stability of CuSCN hole conductor-based perovskite solar cells. *ChemSusChem*, *9*(18), 2592-2596.

Kavan, L., Tétreault, N., Moehl, T., & Grätzel, M. (2014). Electrochemical characterization of TiO_2 blocking layers for dye-sensitized solar cells. *The Journal of Physical Chemistry C*, *118*(30), 16408-16418.

Ke, W., Fang, G., Wan, J., Tao, H., Liu, Q., Xiong, L., Qin, P., Wang, J., Lei, H., & Yang, G. (2015). Efficient hole-blocking layer-free planar halide perovskite thin-film solar cells. *Nature Communications*, *6*(1), 1-7.

Kieslich, G., Sun, S., & Cheetham, A. K. (2014). Solid-state principles applied to organic-inorganic perovskites: new tricks for an old dog. *Chemical Science*, *5*(12), 4712-4715.

Kieslich, G., Sun, S., & Cheetham, A. K. (2015). An extended tolerance factor approach for organic-inorganic perovskites. *Chemical Science*, *6*(6), 3430-3433.

Kim, H.B., Choi, H., Jeong, J., Kim, S., Walker, B., Song, S., & Kim, J. Y. (2014). Mixed solvents for the optimization of morphology in solution-processed, inverted-type perovskite/fullerene hybrid solar cells. *Nanoscale*, *6*(12), 6679-6683.

Kim, Y. Y., Park, E. Y., Yang, T. Y., Noh, J. H., Shin, T. J., Jeon, N. J., & Seo, J. (2018). Fast two-step deposition of perovskite via mediator extraction treatment for large-area, high-performance perovskite solar cells. *Journal of Materials Chemistry A*, *6*(26), 12447-12454.

Kittel, C., McEuen, P., & McEuen, P. (1996). *Introduction to solid state physics* (Vol. 8). Wiley New York.

Koh, T. M., Krishnamoorthy, T., Yantara, N., Shi, C., Leong, W. L., Boix, P. P., Grimsdale, A. C., Mhaisalkar, S. G., & Mathews, N. (2015). Formamidinium tin-based perovskite with low E_g for photovoltaic applications. *Journal of Materials Chemistry A*, *3*(29), 14996-15000.

Kohanoff, J. (2006). *Electronic structure calculations for solids and molecules: theory and computational methods*. Cambridge University Press.

Kohnehpoushi, S., Nazari, P., Nejand, B. A., & Eskandari, M. (2018). MoS_2: a two dimensional hole transporting material for high-efficiency, low-cost perovskite solar cells. *Nanotechnology*, *29*(20), 1-8.

Kojima, A., Teshima, K., Shirai, Y., & Miyasaka, T. (2009). Organometal halide perovskites as visible-light sensitizers for photovoltaic cells. *Journal of the American Chemical Society*, *131*(17), 6050-6051.

Kokalj, A. (1999). XCrySDen: a new program for displaying crystalline structures and electron densities. *Journal of Molecular Graphics and Modelling*, *17*(3-4), 176-179.

Korshunova, K., Winterfeld, L., Beenken, W. J., & Runge, E. (2016). Thermodynamic stability of mixed Pb: Sn methyl-ammonium halide perovskites. *Physica Status Solidi (B)*, *253*(10), 1907-1915.

Koval, S., Kohanoff, J., Lasave, J., Colizzi, G., & Migoni, R. (2005). First-principles study of ferroelectricity and isotope effects in H-bonded KH_2PO_4 crystals. *Physical Review B, 71*(18), 1-15.

Krasnov, K., Filippenko, N., Bobkova, V., Lebedeva, N., Morozov, E., Ustinova, T., & Romanova, G.A. (1979). *Molekulyarnye postoyannye neorganicheskikh soedinenii*. Khimiya, Leningrad.

Kung, P. K., Li, M. H., Lin, P. Y., Chiang, Y. H., Chan, C. R., Guo, T. F., & Chen, P. (2018). A review of inorganic hole transport materials for perovskite solar cells. *Advanced Materials Interfaces*, *5*(22), 1-35.

Laban, W. A., & Etgar, L. (2013). Depleted hole conductor-free lead halide iodide heterojunction solar cells. *Energy & Environmental Science*, *6*(11), 3249-3253.

Lang, L., Yang, J. H., Liu, H. R., Xiang, H., & Gong, X. (2014). First-principles study on the electronic and optical properties of cubic ABX_3 halide perovskites. *Physics Letters A, 378*(3), 290-293.

Lazemi, M., Asgharizadeh, S., & Bellucci, S. (2018). A computational approach to interface engineering of lead-free $CH_3NH_3SnI_3$ highly-efficient perovskite solar cells. *Physical Chemistry Chemical Physics*, *20*(40), 25683-25692.

Leijtens, T., Eperon, G. E., Noel, N. K., Habisreutinger, S. N., Petrozza, A., & Snaith, H. J. (2015). Stability of metal halide perovskite solar cells. *Advanced Energy Materials, 5*(20), 1-23.

Leijtens, T., Eperon, G. E., Pathak, S., Abate, A., Lee, M. M., & Snaith, H. J. (2013). Overcoming ultraviolet light instability of sensitized TiO_2 with meso-superstructured organometal tri-halide perovskite solar cells. *Nature Communications*, *4*(1), 1-8.

Li, C., Lu, X., Ding, W., Feng, L., Gao, Y., & Guo, Z. (2008). Formability of ABX_3 (X= F, Cl, Br, I) Halide Perovskites. *Acta Crystallographica Section B: Structural Science*, *64*(6), 702-707.

Liang, C., Li, P., Zhang, Y., Gu, H., Cai, Q., Liu, X., Wang, J., Wen, H., & Shao, G. (2017). Mild solution-processed metal-doped TiO_2 compact layers for hysteresis-less and performance-enhanced perovskite solar cells. *Journal of Power Sources*, *372*, 235-244.

Liu, X., Bu, T., Li, J., He, J., Li, T., Zhang, J., Li, W., Ku, Z., Peng, Y., & Huang, F. (2018). Stacking n-type layers: effective route towards stable, efficient and hysteresis-free planar perovskite solar cells. *Nano Energy*, *44*, 34-42.

Luo, D., Yang, W., Wang, Z., Sadhanala, A., Hu, Q., Su, R., Shivanna, R., Trindade, G. F., Watts, J. F., & Xu, Z. (2018). Enhanced photovoltage for inverted planar heterojunction perovskite solar cells. *Science*, *360*(6396), 1442-1446.

Madili, N., Pogrebnoi, A., & Pogrebnaya, T. (2018). Theoretical Design of Complex Molecule via Combination of Natural Lawsone and Synthetic Indoline D131 Dyes for Dye Sensitized Solar Cells Application. *Computational Chemistry*, *6*(04), 87-112.

Makoye, A., Pogrebnoi, A., & Pogrebnaya, T. (2020). Lawsone isomers, lawsone ether and bilawsone for dye-sensitized solar cells applications: DFT and UV–Vis studies. *Journal of Molecular Graphics and Modelling*, *94*, 1-10.

Mali, S. S., & Hong, C. K. (2016). pin/nip type planar hybrid structure of highly efficient perovskite solar cells towards improved air stability: synthetic strategies and the role of p-type hole transport layer (HTL) and n-type electron transport layer (ETL) metal oxides. *Nanoscale*, *8*(20), 10528-10540.

Mali, S. S., Shim, C. S., & Hong, C. K. (2015). Highly porous Zinc Stannate (Zn_2SnO_4) nanofibers scaffold photoelectrodes for efficient methyl ammonium halide perovskite solar cells. *Scientific Reports*, *5*, 1-14.

Marcus, Y. (2012). The guanidinium ion. *The Journal of Chemical Thermodynamics*, *48*, 70-74.

Martin, R. M. (2020). *Electronic structure: Basic theory and practical methods*. Cambridge university press.

Matyushin, Y. N., Kon'kova, T., Titova, K., Rosolovskii, V. Y., & Lebedev, Y. A. (1985). Enthalpy of formation of guanidinium nitrate, perchlorate, and chloride. *Bulletin of the Academy of Sciences of the USSR, Division of Chemical Science*, *34*(4), 713-716.

Mitzi, D. B. (1996). Synthesis, crystal structure, and optical and thermal properties of $(C_4H_9NH_3)_2MI_4$ (M= Ge, Sn, Pb). *Chemistry of Materials*, *8*(3), 791-800.

Mitzi, D. B., Chondroudis, K., & Kagan, C. R. (2001). Organic-inorganic electronics. *IBM Journal of Research and Development*, *45*(1), 29-45.

Mitzi, D. B., Feild, C., Schlesinger, Z., & Laibowitz, R. (1995). Transport, optical, and magnetic properties of the conducting halide perovskite $CH_3NH_3SnI_3$. *Journal of Solid State Chemistry*, *114*(1), 159-163.

Miyano, K., Yanagida, M., Tripathi, N., & Shirai, Y. (2016). Hysteresis, stability, and ion migration in lead halide perovskite photovoltaics. *The Journal of Physical Chemistry Letters*, *7*(12), 2240-2245.

Momma, K., & Izumi, F. (2008). VESTA: a three-dimensional visualization system for electronic and structural analysis. *Journal of Applied Crystallography*, *41*(3), 653-658.

Morales-García, A. N., Valero, R., & Illas, F. (2017). An empirical, yet practical way to predict the band gap in solids by using density functional band structure calculations. *The Journal of Physical Chemistry C*, *121*(34), 18862-18866.

Mosconi, E., Amat, A., Nazeeruddin, M. K., Grätzel, M., & De Angelis, F. (2013). First-principles modeling of mixed halide organometal perovskites for photovoltaic applications. *The Journal of Physical Chemistry C, 117*(27), 13902-13913.

Nagabhushana, G., Shivaramaiah, R., & Navrotsky, A. (2016). Direct calorimetric verification of thermodynamic instability of lead halide hybrid perovskites. *Proceedings of the National Academy of Sciences*, *113*(28), 7717-7721.

Navrotsky, A., & Weidner, D. J. (1989). *Perovskite: a structure of great interest to geophysics and materials science.* American Geophysical Union.

Nazarenko, O., Kotyrba, M. R., Yakunin, S., Wörle, M., Benin, B. M., Rainò, G., Krumeich, F., Kepenekian, M., Even, J., & Katan, C. (2019). Guanidinium and mixed cesium-guanidinium tin (ii) bromides: effects of quantum confinement and out of plane octahedral tilting. *Chemistry of Materials*, *31*(6), 2121-2129.

NREL. (2020). *Best Research-Cell Efficiencies*. Retrieved 08 April from https://www.nrel.gov/pv/assets/pdfs/best-research-cell-efficiencies.20200104.pdf

O'Regan, B., & Grätzel, M. (1991). A low-cost, high-efficiency solar cell based on dye-sensitized colloidal TiO_2 films. *Nature*, *353*(6346), 737-740.

Obila, J. O., Lei, H., Ayieta, E. O., Ogacho, A. A., Aduda, B. O., & Wang, F. (2021). Improving the efficiency and stability of tin-based perovskite solar cells using anilinium hypophosphite additive. *New Journal of Chemistry*, *45*(18), 8092-8100.

Ogomi, Y., Kukihara, K., Qing, S., Toyoda, T., Yoshino, K., Pandey, S., Momose, H., & Hayase, S. (2014). Control of charge dynamics through a charge-separation interface for all-solid perovskite-sensitized solar cells. *ChemPhysChem*, *15*(6), 1062-1069.

Ogomi, Y., Morita, A., Tsukamoto, S., Saitho, T., Fujikawa, N., Shen, Q., Toyoda, T., Yoshino, K., Pandey, S. S., & Ma, T. (2014). $CH_3NH_3Sn_xPb_{(1-x)}I_3$ Perovskite solar cells covering up to 1060 nm. *The Journal of Physical Chemistry Letters*, *5*(6), 1004-1011.

Oh, L. S., Kim, D. H., Lee, J. A., Shin, S. S., Lee, J.-W., Park, I. J., Ko, M. J., Park, N. G., Pyo, S. G., & Hong, K. S. (2014). Zn_2SnO_4-based photoelectrodes for organolead halide perovskite solar cells. *The Journal of Physical Chemistry C*, *118*(40), 22991-22994.

Okamoto, Y., Yasuda, T., Sumiya, M., & Suzuki, Y. (2018). Perovskite solar cells prepared by advanced Three-step method using additional $HC(NH_2)_2I$ spin-coating: efficiency improvement with multiple bandgap structure. *ACS Applied Energy Materials*, *1*(3), 1389-1394.

Ono, L. K., & Qi, Y. (2016). Surface and interface aspects of organometal halide perovskite materials and solar cells. *The Journal of Physical Chemistry Letters*, *7*(22), 4764-4794.

Ono, L. K., & Qi, Y. (2018). Research progress on organic-inorganic halide perovskite materials and solar cells. *Journal of Physics D: Applied Physics*, *51*(9), 1-27.

Onoda-Yamamuro, N., Matsuo, T., & Suga, H. (1990). Calorimetric and IR spectroscopic studies of phase transitions in methylammonium trihalogenoplumbates (II). *Journal of Physics and Chemistry of Solids*, *51*(12), 1383-1395.

Park, J. H., Seo, J., Park, S., Shin, S. S., Kim, Y. C., Jeon, N. J., Shin, H. W., Ahn, T. K., Noh, J. H., & Yoon, S. C. (2015). Efficient $CH_3NH_3PbI_3$ perovskite solar cells employing nanostructured p-type NiO electrode formed by a pulsed laser deposition. *Advanced Materials*, *27*(27), 4013-4019.

Park, N.-G. (2015). Perovskite solar cells: an emerging photovoltaic technology. *Materials Today*, *18*(2), 65-72.

Parrott, E. S., Milot, R. L., Stergiopoulos, T., Snaith, H. J., Johnston, M. B., & Herz, L. M. (2016). Effect of structural phase transition on charge-carrier lifetimes and defects in $CH_3NH_3SnI_3$ perovskite. *The Journal of Physical Chemistry Letters*, *7*(7), 1321-1326.

Pathak, S. K., Abate, A., Ruckdeschel, P., Roose, B., Gödel, K. C., Vaynzof, Y., Santhala, A., Watanabe, S. I., Hollman, D. J., & Noel, N. (2014). Performance and stability enhancement of dye-sensitized and perovskite solar cells by Al doping of TiO_2. *Advanced Functional Materials*, *24*(38), 6046-6055.

Peng, L., & Xu, L. (2018). Theoretical and experimental research base on the tin iodide organic-inorganic hybrid perovskite ($CH_3NH_3SnI_3$) tetragonal and orthorhombic phases for photovoltaics. *Science of Advanced Materials*, *10*(10), 1519-1527.

Perdew, J., McMullen, E., & Zunger, A. (1981). Density-functional theory of the correlation energy in atoms and ions: a simple analytic model and a challenge. *Physical Review A*, *23*(6), 2785-2789.

Perdew, J. P., Burke, K., & Ernzerhof, M. (1996). Generalized gradient approximation made simple. *Physical Review Letters*, *77*(18), 3865-3868.

Perdew, J. P., Ernzerhof, M., & Burke, K. (1996). Rationale for mixing exact exchange with density functional approximations. *The Journal of Chemical Physics*, *105*(22), 9982-9985.

Perdew, J. P., Ruzsinszky, A., Csonka, G. I., Vydrov, O. A., Scuseria, G. E., Constantin, L. A., Zhou, X., & Burke, K. (2008). Restoring the density-gradient expansion for exchange in solids and surfaces. *Physical Review Letters*, *100*(13), 1-4.

Perdew, J. P., Yang, W., Burke, K., Yang, Z., Gross, E. K., Scheffler, M., Scuseria, G. E., Henderson, T. M., Zhang, I. Y., & Ruzsinszky, A. (2017). Understanding band gaps of solids in generalized Kohn-Sham theory. *Proceedings of the National Academy of Sciences*, *114*(11), 2801-2806.

Phillips, J. C., & Kleinman, L. (1959). New method for calculating wave functions in crystals and molecules. *Physical Review*, *116*(2), 287-294.

Prasanna, R., Gold-Parker, A., Leijtens, T., Conings, B., Babayigit, A., Boyen, H.G., Toney, M. F., & McGehee, M. D. (2017). Band gap tuning via lattice contraction and octahedral tilting in perovskite materials for photovoltaics. *Journal of the American Chemical Society*, *139*(32), 11117-11124.

Qin, H., Xu, L., & Zhong, D. (2020). First principles study of zinc phthalocyanine molecules adsorbed on methylammonium lead iodide surfaces. *The Journal of Physical Chemistry C*, *124*(9), 5167-5173.

Quarti, C., Mosconi, E., Ball, J. M., D'Innocenzo, V., Tao, C., Pathak, S., Snaith, H. J., Petrozza, A., & De Angelis, F. (2016). Structural and optical properties of methylammonium lead iodide across the tetragonal to cubic phase transition: implications for perovskite solar cells. *Energy & Environmental Science*, *9*(1), 155-163.

Rao, H., Sun, W., Ye, S., Yan, W., Li, Y., Peng, H., Liu, Z., Bian, Z., & Huang, C. (2016). Solution-processed CuS NPs as an inorganic hole-selective contact material for inverted planar perovskite solar cells. *ACS Applied Materials & Interfaces*, *8*(12), 7800-7805.

Rao, H., Ye, S., Sun, W., Yan, W., Li, Y., Peng, H., Liu, Z., Bian, Z., Li, Y., & Huang, C. (2016). A 19.0% efficiency achieved in CuO_x-based inverted $CH_3NH_3PbI_{3-x}Cl_x$ solar cells by an effective Cl doping method. *Nano Energy*, *27*, 51-57.

Razza, S., Di Giacomo, F., Matteocci, F., CinÓ, L., Palma, A. L., Casaluci, S., Cameron, P., D'epifanio, A., Licoccia, S., & Reale, A. (2015). Perovskite solar cells and large area modules (100 cm^2) based on an air flow-assisted PbI_2 blade coating deposition process. *Journal of Power Sources*, *277*, 286-291.

Reining, L. (2018). The GW approximation: content, successes and limitations. *Wiley Interdisciplinary Reviews: Computational Molecular Science*, *8*(3), 1-26.

Rose, G. (1839). Beschreibung einiger neuen Mineralien des Urals. *Annalen der Physik*, *124*(12), 551-573.

Saliba, M., Matsui, T., Seo, J. Y., Domanski, K., Correa-Baena, J. P., Nazeeruddin, M. K., Zakeeruddin, S. M., Tress, W., Abate, A., & Hagfeldt, A. (2016). Cesium-containing triple cation perovskite solar cells: improved stability, reproducibility and high efficiency. *Energy & Environmental Science*, *9*(6), 1989-1997.

Saliba, M., Orlandi, S., Matsui, T., Aghazada, S., Cavazzini, M., Correa-Baena, J. P., Gao, P., Scopelliti, R., Mosconi, E., & Dahmen, K. H. (2016). A molecularly engineered hole-transporting material for efficient perovskite solar cells. *Nature Energy, 1*(2), 1-7.

Schmider, H. L., & Becke, A. D. (1998). Optimized density functionals from the extended G2 test set. *The Journal of Chemical Physics, 108*(23), 9624-9631.

Schmidt, T. M., Larsen-Olsen, T. T., Carlé, J. E., Angmo, D., & Krebs, F. C. (2015). Upscaling of perovskite solar cells: fully ambient roll processing of flexible perovskite solar cells with printed back electrodes. *Advanced Energy Materials*, *5*(15), 1-9.

Setyawan, W., & Curtarolo, S. (2010). High-throughput electronic band structure calculations: Challenges and tools. *Computational Materials Science*, *49*(2), 299-312.

Sha, W. E., Ren, X., Chen, L., & Choy, W. C. (2015). The efficiency limit of $CH_3NH_3PbI_3$ perovskite solar cells. *Applied Physics Letters, 106*(22), 1-5.

Shahbazi, M., & Wang, H. (2016). Progress in research on the stability of organometal perovskite solar cells. *Solar Energy, 123,* 74-87.

Shao, Y., Xiao, Z., Bi, C., Yuan, Y., & Huang, J. (2014). Origin and elimination of photocurrent hysteresis by fullerene passivation in $CH_3NH_3PbI_3$ planar heterojunction solar cells. *Nature Communications*, *5*(1), 1-7.

Sherkar, T. S., Momblona, C., Gil-Escrig, L. n., Ávila, J., Sessolo, M., Bolink, H. J., & Koster, L. J. A. (2017). Recombination in perovskite solar cells: significance of grain boundaries, interface traps, and defect ions. *ACS Energy Letters*, *2*(5), 1214-1222.

Sherkar, T. S., Momblona, C., Gil-Escrig, L., Bolink, H. J., & Koster, L. J. A. (2017). Improving perovskite solar cells: insights from a validated device model. *Advanced Energy Materials*, *7*(13), 1-9.

Shi, Z., Guo, J., Chen, Y., Li, Q., Pan, Y., Zhang, H., Xia, Y., & Huang, W. (2017). Lead-free organic-inorganic hybrid perovskites for photovoltaic applications: recent advances and perspectives. *Advanced Materials*, *29*(16), 1-28.

Shi, Z., & Jayatissa, A. H. (2018). Perovskites-based solar cells: a review of recent progress, materials and processing methods. *Materials*, *11*(5), 1-34.

Shin, S. S., Yang, W. S., Noh, J. H., Suk, J. H., Jeon, N. J., Park, J. H., Kim, J. S., Seong, W. M., & Seok, S. I. (2015). High-performance flexible perovskite solar cells exploiting Zn_2SnO_4 prepared in solution below 100^oC. *Nature Communications*, *6*(1), 1-8.

Shin, S. S., Yeom, E. J., Yang, W. S., Hur, S., Kim, M. G., Im, J., Seo, J., Noh, J. H., & Seok, S. I. (2017). Colloidally prepared La-doped $BaSnO_3$ electrodes for efficient, photostable perovskite solar cells. *Science*, *356*(6334), 167-171.

Sholl, D., & Steckel, J. A. (2011). *Density functional theory: a practical introduction*. John Wiley & Sons.

Singh, D. J., & Nordstrom, L. (2006). *Planewaves, Pseudopotentials, and the LAPW method*. Springer Science & Business Media.

Slavney, A. H., Smaha, R. W., Smith, I. C., Jaffe, A., Umeyama, D., & Karunadasa, H. I. (2017). Chemical approaches to addressing the instability and toxicity of lead–halide perovskite absorbers. *Inorganic Chemistry*, *56*(1), 46-55.

Snaith, H. J., Abate, A., Ball, J. M., Eperon, G. E., Leijtens, T., Noel, N. K., Stranks, S. D., Wang, J. T.-W., Wojciechowski, K., & Zhang, W. (2014). Anomalous hysteresis in perovskite solar cells. *The Journal of Physical Chemistry Letters*, *5*(9), 1511-1515.

Stoumpos, C. C., Malliakas, C. D., & Kanatzidis, M. G. (2013). Semiconducting tin and lead iodide perovskites with organic cations: phase transitions, high mobilities, and near-infrared photoluminescent properties. *Inorganic Chemistry*, *52*(15), 9019-9038.

Stoumpos, C. C., Mao, L., Malliakas, C. D., & Kanatzidis, M. G. (2017). Structure-band gap relationships in hexagonal polytypes and low-dimensional structures of hybrid tin iodide perovskites. *Inorganic Chemistry*, *56*(1), 56-73.

Stranks, S. D., & Snaith, H. J. (2015). Metal halide perovskites for photovoltaic and light-emitting devices. *Nature Nanotechnology*, *10*(5), 391-402.

Suhaili, N., Taib, M. F. M., Yaakob, M. K., Hassan, O. H., & Yahya, M. (2017). Properties of lead-free hybrid organic-inorganic halide perovskite $CH_3NH_3BX_3$ using Density Functional Theory. *Materials Today: Proceedings*, *4*(4), 5154-5160.

Sun, P. P., Li, Q. S., Yang, L. N., & Li, Z. S. (2016). Theoretical insights into a potential lead-free hybrid perovskite: substituting Pb^{2+} with Ge^{2+}. *Nanoscale*, *8*(3), 1503-1512.

Szafrański, M. (1997). Investigation of phase instabilities in guanidinium halogenoplumbates (II). *Thermochimica Acta*, *307*(2), 177-183.

Takahashi, Y., Hasegawa, H., Takahashi, Y., & Inabe, T. (2013). Hall mobility in tin iodide perovskite $CH_3NH_3SnI_3$: evidence for a doped semiconductor. *Journal of Solid State Chemistry*, *205*, 39-43.

Takahashi, Y., Obara, R., Lin, Z. Z., Takahashi, Y., Naito, T., Inabe, T., Ishibashi, S., & Terakura, K. (2011). Charge-transport in tin-iodide perovskite $CH_3NH_3SnI_3$: origin of high conductivity. *Dalton Transactions*, *40*(20), 5563-5568.

Tang, W., Sanville, E., & Henkelman, G. (2009). A grid-based Bader analysis algorithm without lattice bias. *Journal of Physics: Condensed Matter*, *21*(8), 1-7.

Tejuca, L. G., & Fierro, J. L. (1992). *Properties and applications of perovskite-type oxides*. CRC Press.

Thambidurai, M., Shini, F., Harikesh, P., Mathews, N., & Dang, C. (2020). Highly stable and efficient planar perovskite solar cells using ternary metal oxide electron transport layers. *Journal of Power Sources*, *448*, 1-8.

Travis, W., Glover, E., Bronstein, H., Scanlon, D., & Palgrave, R. (2016). On the application of the tolerance factor to inorganic and hybrid halide perovskites: a revised system. *Chemical Science*, *7*(7), 4548-4556.

Tress, W., Marinova, N., Moehl, T., Zakeeruddin, S. M., Nazeeruddin, M. K., & Grätzel, M. (2015). Understanding the rate-dependent J-V hysteresis, slow time component, and aging in $CH_3NH_3PbI_3$ perovskite solar cells: the role of a compensated electric field. *Energy & Environmental Science*, *8*(3), 995-1004.

Troughton, J., Carnie, M. J., Davies, M. L., Charbonneau, C., Jewell, E. H., Worsley, D. A., & Watson, T. M. (2016). Photonic flash-annealing of lead halide perovskite solar cells in 1 ms. *Journal of Materials Chemistry A*, *4*(9), 3471-3476.

Tuoc, V. N., & Huan, T. D. (2020). Lead-free hybrid organic-inorganic perovskites for solar cell applications. *The Journal of Chemical Physics*, *152*(1), 1-8.

Umari, P., Mosconi, E., & De Angelis, F. (2014). Relativistic GW calculations on $CH_3NH_3PbI_3$ and $CH_3NH_3SnI_3$ perovskites for solar cell applications. *Scientific Reports*, *4*, 1-7.

Wang, B., Zhang, M., Cui, X., Wang, Z., Rager, M., Yang, Y., Zou, Z., Wang, Z. L., & Lin, Z. (2020). Unconventional route to oxygen vacancy enabled highly efficient electron extraction and transport in perovskite solar cells. *Angewandte Chemie*, *132*(4), 1628-1635.

Wang, F., Meng, D., Li, X., Zhu, Z., Fu, Z., & Lu, Y. (2015). Influence of annealing temperature on the crystallization and ferroelectricity of perovskite $CH_3NH_3PbI_3$ film. *Applied Surface Science*, *357*, 391-396.

Wang, S., Kavaipatti, B., Kim, S.J., Pan, X., Ramesh, R., Ager III, J. W., & Wang, L.W. (2014). Atomic and electronic structures of lattice mismatched Cu_2O/TiO_2 interfaces. *Applied Physics Letters*, *104*(21), 1-4.

Weerasinghe, H. C., Dkhissi, Y., Scully, A. D., Caruso, R. A., & Cheng, Y. B. (2015). Encapsulation for improving the lifetime of flexible perovskite solar cells. *Nano Energy*, *18*, 118-125.

Williams, S. T., Rajagopal, A., Chueh, C. C., & Jen, A. K. Y. (2016). Current challenges and prospective research for upscaling hybrid perovskite photovoltaics. *The Journal of Physical Chemistry Letters*, *7*(5), 811-819.

Wilson, J. W. (1976). Standard enthalpies of formation and thermodynamic cycle values of crystal lattice energies of methylammonium halides. *Journal of the Chemical Society, Dalton Transactions*(10), 890-893.

Wu, L. J., Zhao, Y. Q., Chen, C. W., Wang, L. Z., Liu, B., & Cai, M. Q. (2016). First-principles hybrid functional study of the electronic structure and charge carrier mobility in perovskite $CH_3NH_3SnI_3$. *Chinese Physics B*, *25*(10), 1-7.

Wu, Y., Yang, X., Chen, H., Zhang, K., Qin, C., Liu, J., Peng, W., Islam, A., Bi, E., & Ye, F. (2014). Highly compact TiO_2 layer for efficient hole-blocking in perovskite solar cells. *Applied Physics Express*, *7*(5), 1-4.

Xiao, M., Huang, F., Huang, W., Dkhissi, Y., Zhu, Y., Etheridge, J., Gray-Weale, A., Bach, U., Cheng, Y. B., & Spiccia, L. (2014). A fast deposition crystallization procedure for highly efficient lead iodide perovskite thin film solar cells. *Angewandte Chemie International Edition*, *53*(37), 9898-9903.

Yang, W. S., Noh, J. H., Jeon, N. J., Kim, Y. C., Ryu, S., Seo, J., & Seok, S. I. (2015). High-performance photovoltaic perovskite layers fabricated through intramolecular exchange. *Science*, *348*(6240), 1234-1237.

Yang, Z., Cai, B., Zhou, B., Yao, T., Yu, W., Liu, S. F., Zhang, W. H., & Li, C. (2015). An up-scalable approach to $CH_3NH_3PbI_3$ compact films for high-performance perovskite solar cells. *Nano Energy*, *15*, 670-678.

Yang, Z., Chueh, C. C., Liang, P. W., Crump, M., Lin, F., Zhu, Z., & Jen, A. K. Y. (2016). Effects of formamidinium and bromide ion substitution in methylammonium lead triiodide toward high-performance perovskite solar cells. *Nano Energy*, *22*, 328-337.

Yang, Z., Wang, Y., & Liu, Y. (2018). Stability and charge separation of different $CH_3NH_3SnI_3/TiO_2$ interface: A first-principles study. *Applied Surface Science*, *441*, 394-400.

Yantara, N., Sabba, D., Yanan, F., Kadro, J. M., Moehl, T., Boix, P. P., Mhaisalkar, S., Grätzel, M., & Grätzel, C. (2015). Loading of mesoporous titania films by $CH_3NH_3PbI_3$ perovskite, single step vs. sequential deposition. *Chemical Communications*, *51*(22), 4603-4606.

Ye, M., Hong, X., Zhang, F., & Liu, X. (2016). Recent advancements in perovskite solar cells: flexibility, stability and large scale. *Journal of Materials Chemistry A*, *4*(18), 6755-6771.

Yi, C., Li, X., Luo, J., Zakeeruddin, S. M., & Grätzel, M. (2016). Perovskite photovoltaics with outstanding performance produced by chemical conversion of bilayer mesostructured lead halide/TiO_2 films. *Advanced Materials*, *28*(15), 2964-2970.

Yu, W., Li, F., Wang, H., Alarousu, E., Chen, Y., Lin, B., Wang, L., Hedhili, M. N., Li, Y., & Wu, K. (2016). Ultrathin Cu_2O as an efficient inorganic hole transporting material for perovskite solar cells. *Nanoscale*, *8*(11), 6173-6179.

Zhang, H., Wang, H., Chen, W., & Jen, A. K. Y. (2017). $CuGaO_2$: A promising inorganic hole-transporting material for highly efficient and stable perovskite solar cells. *Advanced Materials*, *29*(8), 1-8.

Zhang, Q., Dandeneau, C. S., Zhou, X., & Cao, G. (2009). ZnO nanostructures for dye-sensitized solar cells. *Advanced Materials*, *21*(41), 4087-4108.

Zhang, T., Chen, H., Bai, Y., Xiao, S., Zhu, L., Hu, C., Xue, Q., & Yang, S. (2016). Understanding the relationship between ion migration and the anomalous hysteresis in high-efficiency perovskite solar cells: a fresh perspective from halide substitution. *Nano Energy*, *26*, 620-630.

Zhang, Y. Y., Chen, S., Xu, P., Xiang, H., Gong, X. G., Walsh, A., & Wei, S. H. (2018). Intrinsic instability of the hybrid halide perovskite semiconductor $CH_3NH_3PbI_3$. *Chinese Physics Letters*, *35*(3), 1-6.

Zhao, P., Liu, Z., Lin, Z., Chen, D., Su, J., Zhang, C., Zhang, J., Chang, J., & Hao, Y. (2018). Device simulation of inverted $CH_3NH_3PbI_{3-x}Cl_x$ perovskite solar cells based on PCBM electron transport layer and NiO hole transport layer. *Solar Energy*, *169*, 11-18.

Zhao, X.-G., Yang, J. H., Fu, Y., Yang, D., Xu, Q., Yu, L., Wei, S. H., & Zhang, L. (2017). Design of lead-free inorganic halide perovskites for solar cells via cation-transmutation. *Journal of the American Chemical Society*, *139*(7), 2630-2638.

Zhao, X., & Park, N. G. (2015). Stability issues on perovskite solar cells. *Photonics*, *2*(4), 1139-1151.

Zhou, H., Chen, Q., Li, G., Luo, S., Song, T. B., Duan, H. S., Hong, Z., You, J., Liu, Y., & Yang, Y. (2014). Interface engineering of highly efficient perovskite solar cells. *Science*, *345*(6196), 542-546.

Zhou, Y., Yang, M., Game, O. S., Wu, W., Kwun, J., Strauss, M. A., Yan, Y., Huang, J., Zhu, K., & Padture, N. P. (2016). Manipulating crystallization of organolead mixed-halide thin films in antisolvent baths for wide-bandgap perovskite solar cells. *ACS Applied Materials & Interfaces*, *8*(3), 2232-2237.

Zhou, Y., Yang, M., Wu, W., Vasiliev, A. L., Zhu, K., & Padture, N. P. (2015). Room-temperature crystallization of hybrid-perovskite thin films via solvent-solvent extraction for high-performance solar cells. *Journal of Materials Chemistry A*, *3*(15), 8178-8184.

Zhu, L., Shao, Z., Ye, J., Zhang, X., Pan, X., & Dai, S. (2016). Mesoporous $BaSnO_3$ layer based perovskite solar cells. *Chemical Communications*, *52*(5), 970-973.

Zhu, P., Gu, S., Luo, X., Gao, Y., Li, S., Zhu, J., & Tan, H. (2020). Simultaneous contact and grain-boundary passivation in planar perovskite solar cells using SnO_2-KCl composite electron transport layer. *Advanced Energy Materials*, *10*(3), 1-7.

Zuo, C., & Ding, L. (2015). Solution-processed Cu_2O and CuO as hole transport materials for efficient perovskite solar cells. *Small*, *11*(41), 5528-5532.

APPENDICES

Appendix 1: The optimized geometric parameters of the O-phase of $MASnI_3$ using LDA, PBE and PBEsol XC functionals as represented by Tables A1(a) – A1(c)

Table A1(a): The coordinates for $MASnI_3$ using LDA XC functional

ATOM	ATOMIC POSITIONS (Å)		
	X	Y	Z
Sn	−0.5247	0.0083	0.0453
Sn	3.8050	−0.0381	4.5448
Sn	4.7796	6.4387	3.8406
Sn	0.5142	6.4772	0.7132
I	1.0939	0.1165	3.4421
I	7.0266	13.0371	6.4525
I	2.7257	12.8340	7.2515
I	5.2470	0.0715	1.1184
I	5.7905	6.5359	0.7806
I	1.0364	6.8149	7.1030
I	5.2776	6.7298	6.6156
I	1.5501	6.5756	3.7644
I	0.7731	3.5514	9.6819
I	7.9335	9.9812	−0.2033
I	3.7466	9.9313	4.7205
I	5.0350	3.5141	4.0382
C	0.8787	3.1914	5.4956
C	7.7586	9.7493	4.4625
C	3.4759	9.6692	0.1384
C	5.0542	3.1206	8.2297
N	0.2847	10.0266	5.4708
N	8.6351	3.4167	4.2499
N	4.3453	3.3820	0.3273
N	4.4742	9.9189	8.2583
H	0.2923	9.3022	6.2300
H	8.9372	4.3296	3.8219
H	4.6764	4.2914	0.7401
H	4.4837	9.1642	7.5284
H	4.2599	10.8307	7.7798
H	4.5442	2.6152	1.0152
H	8.8435	2.6468	3.5690
H	0.1003	10.9581	5.9177
H	−0.5619	8.7479	4.0406
H	9.1620	4.0051	6.2087
H	4.8375	3.9201	7.5022
H	3.6546	8.6765	0.5781
H	3.5743	10.4460	0.9137
H	4.7457	2.1401	7.8321
H	9.0855	2.2167	5.9218
H	−0.6626	10.5109	3.6695
H	1.9592	3.1923	5.2612
H	6.7534	9.7970	4.9255
H	2.4605	9.7163	−0.3023
H	6.1398	3.1111	8.4367
H	1.2685	10.0492	5.0757
H	7.5894	3.4454	4.3719
H	3.2982	3.4374	0.2208
H	5.4638	9.9765	8.6347

Table A1(b): The coordinates for MASnI$_3$ using PBE XC functional

ATOM	ATOMIC POSITIONS (Å)		
	X	Y	Z
Sn	−0.1364	−0.0860	−0.0097
Sn	4.1236	−0.0920	4.6127
Sn	4.4042	6.4279	4.5743
Sn	0.1400	6.4184	0.0393
I	1.6636	0.3608	2.6987
I	6.8415	12.8178	6.4026
I	2.5948	12.8194	7.3134
I	5.9166	0.3610	1.8596
I	5.8962	6.2877	1.8122
I	2.6023	6.8869	7.2969
I	6.8502	6.8872	6.4107
I	1.6373	6.2896	2.7447
I	0.3401	3.4251	9.0279
I	8.1628	9.9384	0.1192
I	3.9128	9.9364	4.4505
I	4.5931	3.4283	4.7003
C	0.2743	3.3066	5.1479
C	8.2315	9.8462	4.0010
C	3.9824	9.8457	0.5689
C	4.5218	3.3069	8.5797
N	0.3255	9.8485	5.3732
N	8.1799	3.3072	3.7760
N	3.9288	3.3077	0.7933
N	4.5753	9.8477	8.3550
H	0.0307	9.0011	5.8983
H	8.4970	4.1431	3.2443
H	4.2476	4.1430	1.3251
H	4.2792	9.0005	7.8298
H	4.2560	10.6818	7.8227
H	4.2257	2.4611	1.3184
H	8.4764	2.4603	3.2508
H	0.0063	10.6829	5.9055
H	0.0723	8.9488	3.4763
H	8.4384	4.2056	5.6727
H	4.1864	4.2062	8.0555
H	4.3226	8.9482	1.0933
H	4.3180	10.7445	1.0941
H	4.1820	2.4096	8.0543
H	8.4339	2.4098	5.6740
H	0.0678	10.7446	3.4753
H	1.3640	3.3043	5.0547
H	7.1416	9.8436	4.0928
H	2.8924	9.8432	0.4773
H	5.6116	3.3045	8.6725
H	1.3650	9.8643	5.3224
H	7.1405	3.3211	3.8280
H	2.8896	3.3218	0.7431
H	5.6148	9.8635	8.4052

Table A1(c): The coordinates for $MASnI_3$ using PBEsol XC functional

ATOM	ATOMIC POSITIONS (Å)		
	X	Y	Z
Sn	−0.1364	−0.0860	−0.0097
Sn	4.1236	−0.0920	4.6127
Sn	4.4042	6.4279	4.5743
Sn	0.1400	6.4184	0.0393
I	1.6636	0.3608	2.6987
I	6.8415	12.8178	6.4026
I	2.5948	12.8194	7.3134
I	5.9166	0.3610	1.8596
I	5.8962	6.2877	1.8122
I	2.6023	6.8869	7.2969
I	6.8502	6.8872	6.4107
I	1.6373	6.2896	2.7447
I	0.3401	3.4251	9.0279
I	8.1628	9.9384	0.1192
I	3.9128	9.9364	4.4505
I	4.5931	3.4283	4.7003
C	0.2743	3.3066	5.1479
C	8.2315	9.8462	4.0010
C	3.9824	9.8457	0.5689
C	4.5218	3.3069	8.5797
N	0.3255	9.8485	5.3732
N	8.1799	3.3072	3.7760
N	3.9288	3.3077	0.7933
N	4.5753	9.8477	8.3550
H	0.0307	9.0011	5.8983
H	8.4970	4.1431	3.2443
H	4.2476	4.1430	1.3251
H	4.2792	9.0005	7.8298
H	4.2560	10.6818	7.8227
H	4.2257	2.4611	1.3184
H	8.4764	2.4603	3.2508
H	0.0063	10.6829	5.9055
H	0.0723	8.9488	3.4763
H	8.4384	4.2056	5.6727
H	4.1864	4.2062	8.0555
H	4.3226	8.9482	1.0933
H	4.3180	10.7445	1.0941
H	4.1820	2.4096	8.0543
H	8.4339	2.4098	5.6740
H	0.0678	10.7446	3.4753
H	1.3640	3.3043	5.0547
H	7.1416	9.8436	4.0928
H	2.8924	9.8432	0.4773
H	5.6116	3.3045	8.6725
H	1.3650	9.8643	5.3224
H	7.1405	3.3211	3.8280
H	2.8896	3.3218	0.7431
H	5.6148	9.8635	8.4052

Appendix 2: The optimized geometric parameters of the O-phase of GUASnX_3 using PBE XC functional as represented by Tables A2(a) – A2(c)

Table A2(a): The optimized geometric parameters of GUASnCl_3

ATOM	ATOMIC POSITIONS (Å)		
	X	Y	Z
Sn	5.4703	9.5517	6.7808
Sn	1.4432	9.0551	11.0458
Sn	2.5840	3.3494	2.1325
Sn	6.6111	2.8528	15.6942
Sn	2.5840	2.8528	11.0458
Sn	6.6111	3.3494	6.7808
Sn	5.4703	9.0551	15.6942
Sn	1.4432	9.5517	2.1325
Cl	7.0724	9.6881	4.7353
Cl	3.0453	8.9187	13.0913
Cl	0.9818	3.4859	4.1780
Cl	5.0089	2.7164	13.6487
Cl	0.9818	2.7164	13.0913
Cl	5.0089	3.4859	4.7353
Cl	7.0724	8.9187	13.6487
Cl	3.0453	9.6881	4.1780
Cl	5.3900	12.0606	7.0757
Cl	1.3629	6.5462	10.7510
Cl	2.6642	5.8583	1.8376
Cl	6.6913	0.3439	15.9890
Cl	2.6642	0.3439	10.7510
Cl	6.6913	5.8583	7.0757
Cl	5.3900	6.5462	15.9890
Cl	1.3629	12.0606	1.8376
Cl	7.5761	9.3773	8.2856
Cl	3.5490	9.2295	9.5411
Cl	0.4781	3.1750	0.6278
Cl	4.5052	3.0272	17.1989
Cl	0.4781	3.0272	9.5411
Cl	4.5052	3.1750	8.2856
Cl	7.5761	9.2295	17.1989
Cl	3.5490	9.3773	0.6278
C	1.5088	0.3485	6.4859
C	5.5359	5.8537	11.3408
C	6.5455	6.5508	2.4275
C	2.5183	12.0560	15.3992
C	6.5455	12.0560	11.3408
C	2.5183	6.5508	6.4859
C	1.5088	5.8537	15.3992
C	5.5359	0.3485	2.4275
N	0.6357	0.1031	5.4954
N	4.6629	6.0991	12.3313
N	7.4185	6.3054	3.4179
N	3.3914	12.3014	14.4087
N	7.4185	12.3014	12.3313
N	3.3914	6.3054	5.4954
N	0.6357	6.0991	14.4087
N	4.6629	0.1031	3.4179
N	2.3258	1.4044	6.3862
N	6.3529	4.7978	11.4405
N	5.7284	7.6067	2.5271
N	1.7013	11.0001	15.2995
N	5.7284	11.0001	11.4405
N	1.7013	7.6067	6.3862
N	2.3258	4.7978	15.2995
N	6.3529	1.4044	2.5271
N	1.5604	11.9508	7.5521
N	5.5875	6.6559	10.2745
N	6.4939	5.7486	1.3612
N	2.4667	0.4537	16.4655
N	6.4939	0.4537	10.2745
N	2.4667	5.7486	7.5521
N	1.5604	6.6559	16.4655
N	5.5875	11.9508	1.3612
H	0.0815	11.6499	5.4812
H	4.1086	6.9568	12.3455
H	7.9727	5.4477	3.4321
H	3.9456	0.7546	14.3945
H	7.9727	0.7546	12.3455

H	3.9456	5.4477	5.4812
H	0.0815	6.9568	14.3945
H	4.1086	11.6499	3.4321
H	0.7494	0.5782	4.6046
H	4.7765	5.6241	13.2221
H	7.3049	6.7804	4.3088
H	3.2777	11.8263	13.5179
H	7.3049	11.8263	13.2221
H	3.2777	6.7804	4.6046
H	0.7494	5.6241	13.5179
H	4.7765	0.5782	4.3088
H	2.1426	2.1153	5.6760
H	6.1697	4.0869	12.1507
H	5.9116	8.3176	3.2373
H	1.8845	10.2892	14.5893
H	5.9116	10.2892	12.1507
H	1.8845	8.3176	5.6760
H	2.1426	4.0869	14.5893
H	6.1697	2.1153	3.2373
H	2.9914	1.6399	7.1211
H	7.0185	4.5624	10.7055
H	5.0628	7.8421	1.7922
H	1.0357	10.7646	16.0345
H	5.0628	10.7646	10.7055
H	1.0357	7.8421	7.1211
H	2.9914	4.5624	16.0345
H	7.0185	1.6399	1.7922
H	0.9299	11.1507	7.6395
H	4.9570	7.4561	10.1872
H	7.1243	4.9485	1.2738
H	3.0972	1.2538	16.5528
H	7.1243	1.2538	10.1872
H	3.0972	4.9485	7.6395
H	0.9299	7.4561	16.5528
H	4.9570	11.1507	1.2738
H	2.0869	12.2184	8.3839
H	6.1140	6.3884	9.4427
H	5.9673	6.0161	0.5294
H	1.9402	0.1861	17.2973
H	5.9673	0.1861	9.4427
H	1.9402	6.0161	8.3839
H	2.0869	6.3884	17.2973
H	6.1140	12.2184	0.5294

Table A2(b): The optimized geometric parameters of $GUASnBr_3$

ATOM	ATOMIC POSITIONS (Å)		
	X	Y	Z
Sn	6.1808	10.1096	6.8652
Sn	1.7724	9.4292	11.3589
Sn	2.6360	3.5966	2.2469
Sn	7.0444	2.9163	15.9772
Sn	2.6360	2.9163	11.3589
Sn	7.0444	3.5966	6.8652
Sn	6.1808	9.4292	15.9772
Sn	1.7724	10.1096	2.2469
Br	7.8159	10.2852	4.6759
Br	3.4075	9.2536	13.5483
Br	1.0009	3.7722	4.4362
Br	5.4093	2.7407	13.7879
Br	1.0009	2.7407	13.5483
Br	5.4093	3.7722	4.6759
Br	7.8159	9.2536	13.7879
Br	3.4075	10.2852	4.4362
Br	5.8741	12.7655	7.1559
Br	1.4657	6.7733	11.0682
Br	2.9427	6.2525	1.9561
Br	7.3511	0.2604	16.2680
Br	2.9427	0.2604	11.0682
Br	7.3511	6.2525	7.1559
Br	5.8741	6.7733	16.2680
Br	1.4657	12.7655	1.9561
Br	8.3867	9.9892	8.4976
Br	3.9783	9.5496	9.7265
Br	0.4301	3.4762	0.6144
Br	4.8385	3.0367	17.6097
Br	0.4301	3.0367	9.7265
Br	4.8385	3.4762	8.4976
Br	8.3867	9.5496	17.6097
Br	3.9783	9.9892	0.6144
C	1.6950	0.4087	6.6928
C	6.1034	6.1042	11.5313
C	7.1218	6.9216	2.4192
C	2.7134	12.6171	15.8049
C	7.1218	12.6171	11.5313
C	2.7134	6.9216	6.6928
C	1.6950	6.1042	15.8049
C	6.1034	0.4087	2.4192
N	0.7977	0.1627	5.7238
N	5.2061	6.3503	12.5003
N	8.0191	6.6756	3.3882
N	3.6107	12.8632	14.8359
N	8.0191	12.8632	12.5003
N	3.6107	6.6756	5.7238
N	0.7977	6.3503	14.8359
N	5.2061	0.1627	3.3882
N	2.5134	1.4627	6.5700
N	6.9218	5.0502	11.6541
N	6.3034	7.9756	2.5420
N	1.8950	11.5632	15.6821
N	6.3034	11.5632	11.6541
N	1.8950	7.9756	6.5700
N	2.5134	5.0502	15.6821
N	6.9218	1.4627	2.5420
N	1.7705	12.6321	7.7568
N	6.1789	6.9067	10.4673
N	7.0463	6.1192	1.3552
N	2.6379	0.3938	16.8689
N	7.0463	0.3938	10.4673
N	2.6379	6.1192	7.7568
N	1.7705	6.9067	16.8689
N	6.1789	12.6321	1.3552
H	0.2325	12.3402	5.7362
H	4.6409	7.1986	12.4880
H	8.5843	5.8273	3.3759
H	4.1759	0.6857	14.8482
H	8.5843	0.6857	12.4880
H	4.1759	5.8273	5.7362
H	0.2325	7.1986	14.8482
H	4.6409	12.3402	3.3759
H	0.8995	0.6146	4.8191
H	5.3079	5.8984	13.4050
H	7.9172	7.1275	4.2929
H	3.5089	12.4113	13.9312

H	7.9172	12.4113	13.4050
H	3.5089	7.1275	4.8191
H	0.8995	5.8984	13.9312
H	5.3079	0.6146	4.2929
H	2.2869	2.1921	5.8912
H	6.6952	4.3208	12.3329
H	6.5299	8.7051	3.2209
H	2.1215	10.8337	15.0032
H	6.5299	10.8337	12.3329
H	2.1215	8.7051	5.8912
H	2.2869	4.3208	15.0032
H	6.6952	2.1921	3.2209
H	3.1900	1.6993	7.2936
H	7.5984	4.8136	10.9305
H	5.6268	8.2123	1.8184
H	1.2184	11.3265	16.4057
H	5.6268	11.3265	10.9305
H	1.2184	8.2123	7.2936
H	3.1900	4.8136	16.4057
H	7.5984	1.6993	1.8184
H	1.1374	11.8346	7.8540
H	5.5458	7.7042	10.3701
H	7.6794	5.3217	1.2581
H	3.2710	1.1913	16.9660
H	7.6794	1.1913	10.3701
H	3.2710	5.3217	7.8540
H	1.1374	7.7042	16.9660
H	5.5458	11.8346	1.2581
H	2.2925	12.9098	8.5892
H	6.7009	6.6290	9.6349
H	6.5243	6.3969	0.5228
H	2.1159	0.1160	17.7013
H	6.5243	0.1160	9.6349
H	2.1159	6.3969	8.5892
H	2.2925	6.6290	17.7013
H	6.7009	12.9098	0.5228

Table A2(c): The optimized geometric parameters of $GUASnI_3$

ATOM	ATOMIC POSITIONS (Å)		
	X	Y	Z
Sn	6.3207	11.0161	7.1720
Sn	1.8418	10.2422	11.8484
Sn	2.6370	3.9300	2.3382
Sn	7.1158	3.1561	16.6822
Sn	2.6370	3.1561	11.8484
Sn	7.1158	3.9300	7.1720
Sn	6.3207	10.2422	16.6822
Sn	1.8418	11.0161	2.3382
I	8.1412	11.0451	4.7918
I	3.6623	10.2132	14.2286
I	0.8165	3.9590	4.7184
I	5.2953	3.1271	14.3021
I	0.8165	3.1271	14.2286
I	5.2953	3.9590	4.7918
I	8.1412	10.2132	14.3021
I	3.6623	11.0451	4.7184
I	6.0880	13.9014	7.4487
I	1.6092	7.3569	11.5717
I	2.8696	6.8153	2.0615
I	7.3484	0.2708	16.9590
I	2.8696	0.2708	11.5717
I	7.3484	6.8153	7.4487
I	6.0880	7.3569	16.9590
I	1.6092	13.9014	2.0615
I	8.6542	10.7687	9.0351
I	4.1754	10.4896	9.9853
I	0.3034	3.6826	0.4751
I	4.7822	3.4035	18.5454
I	0.3034	3.4035	9.9853
I	4.7822	3.6826	9.0351
I	8.6542	10.4896	18.5454
I	4.1754	10.7687	0.4751
C	1.7421	0.3537	6.9488
C	6.2209	6.7325	12.0717
C	7.2155	7.4398	2.5614
C	2.7367	13.8186	16.4590
C	7.2155	13.8186	12.0717
C	2.7367	7.4398	6.9488
C	1.7421	6.7325	16.4590
C	6.2209	0.3537	2.5614
N	0.9740	0.0185	5.9013
N	5.4528	7.0677	13.1192
N	7.9836	7.1046	3.6089
N	3.5048	14.1538	15.4115
N	7.9836	14.1538	13.1192
N	3.5048	7.1046	5.9013
N	0.9740	7.0677	15.4115
N	5.4528	0.0185	3.6089
N	2.4944	1.4601	6.8807
N	6.9732	5.6260	12.1398
N	6.4632	8.5463	2.6295
N	1.9844	12.7121	16.3909
N	6.4632	12.7121	12.1398
N	1.9844	8.5463	6.8807
N	2.4944	5.6260	16.3909
N	6.9732	1.4601	2.6295
N	1.7596	13.7600	8.0425
N	6.2384	7.4983	10.9780
N	7.1980	6.6739	1.4677
N	2.7192	0.4122	17.5527
N	7.1980	0.4122	10.9780
N	2.7192	6.6739	8.0425
N	1.7596	7.4983	17.5527
N	6.2384	13.7600	1.4677
H	0.4296	13.3292	5.9035
H	4.9084	7.9291	13.1169
H	8.5280	6.2431	3.6067
H	4.0492	0.8430	15.4138
H	8.5280	0.8430	13.1169
H	4.0492	6.2431	5.9035
H	0.4296	7.9291	15.4138
H	4.9084	13.3292	3.6067
H	1.1376	0.4392	4.9901
H	5.6164	6.6470	14.0304
H	7.8200	7.5253	4.5201
H	3.3412	13.7331	14.5003

H	7.8200	13.7331	14.0304
H	3.3412	7.5253	4.9901
H	1.1376	6.6470	14.5003
H	5.6164	0.4392	4.5201
H	2.2861	2.1692	6.1761
H	6.7649	4.9169	12.8443
H	6.6715	9.2553	3.3341
H	2.1927	12.0030	15.6863
H	6.6715	12.0030	12.8443
H	2.1927	9.2553	6.1761
H	2.2861	4.9169	15.6863
H	6.7649	2.1692	3.3341
H	3.0896	1.7464	7.6558
H	7.5684	5.3397	11.3647
H	5.8680	8.8325	1.8544
H	1.3892	12.4258	17.1660
H	5.8680	12.4258	11.3647
H	1.3892	8.8325	7.6558
H	3.0896	5.3397	17.1660
H	7.5684	1.7464	1.8544
H	1.2195	12.8951	8.0955
H	5.6983	8.3632	10.9250
H	7.7381	5.8090	1.4148
H	3.2593	1.2771	17.6057
H	7.7381	1.2771	10.9250
H	3.2593	5.8090	8.0955
H	1.2195	8.3632	17.6057
H	5.6983	12.8951	1.4148
H	2.1933	14.0836	8.9080
H	6.6721	7.1747	10.1125
H	6.7643	6.9975	0.6023
H	2.2855	0.0886	18.4182
H	6.7643	0.0886	10.1125
H	2.2855	6.9975	8.9080
H	2.1933	7.1747	18.4182
H	6.6721	14.0836	0.6023

Appendix 3: The optimized geometric parameters of MASnI$_3$/Cu$_2$O composite using PBE XC functional

ATOM	ATOMIC POSITIONS (Å)		
	X	Y	Z
Sn	0.0000	0.0000	0.0000
Sn	0.6494	−0.5184	11.0685
Sn	4.2516	0.0000	4.6050
Sn	4.2516	6.3696	4.6050
Sn	0.0000	6.3696	0.0000
Sn	0.7399	7.0224	11.2133
H	0.0095	4.0243	3.2534
H	4.2611	4.0243	1.3516
H	4.6893	8.6884	7.9227
H	4.7020	10.3631	7.9097
H	4.2611	2.3453	1.3516
H	0.0095	2.3453	3.2534
H	0.0946	8.6567	3.5315
H	4.5206	3.9720	8.3908
H	4.3462	8.6567	1.0735
H	4.3462	10.4519	1.0735
H	4.2037	2.4515	9.2780
H	0.0946	10.4519	3.5315
H	1.3463	3.1848	5.0914
H	2.9053	9.5543	0.4864
H	5.4566	3.5893	9.8691
H	1.3508	9.5543	5.4060
H	2.9008	3.1848	0.8010
H	5.9164	9.5243	8.7489
H	8.4085	2.2872	5.6785
H	8.4085	4.0824	5.6785
H	7.1569	9.5543	4.1186
H	4.1570	2.2872	28.1366
H	4.1570	4.0824	28.1366
H	5.5979	3.1848	28.7236
H	4.2251	8.6670	10.3244
H	2.9707	9.5252	9.3665
H	4.2003	10.4622	10.2720
H	8.4936	8.7148	5.9566
H	3.7275	5.1613	10.4096
H	4.2420	8.7148	27.8584
H	4.2420	10.3938	27.8584
H	3.3564	3.6860	11.2652
H	8.4936	10.3938	5.9566
H	7.1524	3.1848	3.8040
H	2.5205	4.2052	9.7950
H	5.6024	9.5543	28.4090
C	0.2544	3.1848	5.1603
C	3.9972	9.5543	0.5553
C	4.4750	3.5073	9.3823
C	8.2488	9.5543	4.0497
C	4.5059	3.1848	28.6547
C	4.0149	9.5454	9.7048
I	1.7030	0.2851	2.7009
I	5.9545	0.2851	1.9041
I	5.9545	6.0845	1.9041
I	2.8547	6.6502	7.2041
I	6.8364	6.5930	5.9166
I	1.7030	6.0845	2.7009
I	0.1375	4.6227	9.7706
I	3.9185	9.5543	4.4623
I	4.5847	3.1848	4.7477
I	0.3331	3.1848	29.0673
I	2.9191	12.5212	7.2455
I	8.1701	9.5543	0.1427
I	8.4502	9.5211	9.2844
I	6.8585	12.5098	5.8998
N	0.3111	9.5543	5.4332
N	3.9405	3.1848	0.8282
N	4.8939	9.5292	8.4997
N	8.1920	3.1848	3.7768
N	4.5627	9.5543	28.3818
N	3.4632	4.1837	10.2306
Cu	0.2838	0.0906	13.7063
Cu	0.0000	0.0000	17.8046
Cu	0.0422	4.1682	13.7645

Cu	0.0000	4.3046	17.8046
Cu	0.0950	8.4712	13.6680
Cu	0.0000	8.6092	17.8046
Cu	3.6164	0.0074	13.3686
Cu	4.3046	0.0000	17.8046
Cu	4.3657	4.1295	13.6641
Cu	4.3046	4.3046	17.8046
Cu	4.5646	8.2660	13.5897
Cu	4.3046	8.6092	17.8046
Cu	2.1239	2.2685	13.5343
Cu	2.1523	2.1523	17.8046
Cu	2.5269	6.3153	13.4824
Cu	2.1523	6.4569	17.8046
Cu	1.8668	10.7303	13.5314
Cu	2.1523	10.7615	17.8046
Cu	6.1810	2.0328	13.7720
Cu	6.4569	2.1523	17.8046
Cu	6.5170	6.3909	13.5250
Cu	6.4569	6.4569	17.8046
Cu	6.6024	10.6385	13.5702
Cu	6.4569	10.7615	17.8046
Cu	2.0781	0.1414	15.7344
Cu	2.1656	4.4077	15.7352
Cu	1.9886	8.8301	16.1947
Cu	6.1933	−0.0468	15.6791
Cu	6.3986	4.3869	15.8389
Cu	6.3906	8.6735	15.7430
Cu	0.1713	2.1635	15.7796
Cu	0.1481	6.4203	15.7226
Cu	0.0568	10.5997	15.7721
Cu	4.1980	1.9974	15.6810
Cu	4.3782	6.3961	15.8070
Cu	4.4762	10.5361	16.0641
O	1.0390	1.1220	14.5505
O	1.2011	5.4550	14.5130
O	1.0927	9.5031	14.6720
O	4.9766	0.7652	14.4737
O	5.4011	5.3562	14.6350
O	5.3214	9.6820	14.5671
O	3.2284	3.2284	16.7285
O	3.2284	7.5330	16.7285
O	3.2284	11.8376	16.7285
O	7.5330	3.2284	16.7285
O	7.5330	7.5330	16.7285
O	7.5330	11.8376	16.7285
O	7.5616	11.6897	12.3968
O	7.3656	3.0880	12.9963
O	7.5467	7.4295	12.4045
O	2.4449	11.8475	12.2077
O	3.3337	3.1567	12.5423
O	3.8048	7.0838	12.4843

Appendix 4: Processing of perovskite solar cell films

The processing of the halide perovskite films involves the reaction of an organic halide with a metal halide such as SnI_2 or $PbCl_2$. The crystallization process is followed by a series of colour changes from yellow to light brown and dark brown upon annealing indicating the formation of the perovskite as a final product (Fakharuddin *et al.*, 2016). In order to achieve highly crystalline films which are smooth and with the ability to absorb a large amount of incident light from the sun, crystallization should be sharply controlled and monitored. There are various synthesis routes for perovskite solar cells which are; single-step deposition, double step deposition, vacuum-assisted evaporation, as well as dual-source evaporation.

Single-Step Deposition Method

Single-step deposition (Fig. 35) is a low cost and the simplest way in processing high-performance halide perovskite solar cells. The deposition of the perovskite absorber is usually done from a solution of the metal halide and the organic halide in a solvent which is polar like DMSO (Conings *et al.*, 2014), DMF (Jeng *et al.*, 2013), or mixed solvents (Kim *et al.*, 2014). Slot die coating and blade have been demonstrated as the most suitable methods for large areas coating but for lab-scale, spin coating technique is mostly preferred (Razza *et al.*, 2015; Schmidt *et al.*, 2015; Yang *et al.*, 2016). The deposition process is usually followed by annealing at temperatures 70-110 °C to evaporate the solvent so as to crystallize the perovskite (Troughton *et al.*, 2016). The annealing process can also be accompanied by the incorporation of the hole and electron transport materials. Despite the simplicity of the single-step deposition method, the choice of solvents and the preparation of the precursors from the deposition to the annealing stage may cause a reduction in efficiency of the device as a result of reduction of absorption capability (Colella *et al.*, 2013; Eperon *et al.*, 2014; Wang *et al.*, 2015). In order to reduce these effects, the modified single-step deposition method is adopted by engineering the solvent by dripping or drop-casting as well as solvent-solvent extraction which help to control the crystallization of very uniform and dense perovskite solar cell films (Xiao *et al.*, 2014; Zhou *et al.*, 2016; Zhou *et al.*, 2015). This method has been widely used in the lab and was able to produce cells with efficiency greater than 18.8% (Saliba, Matsui, *et al.*, 2016).

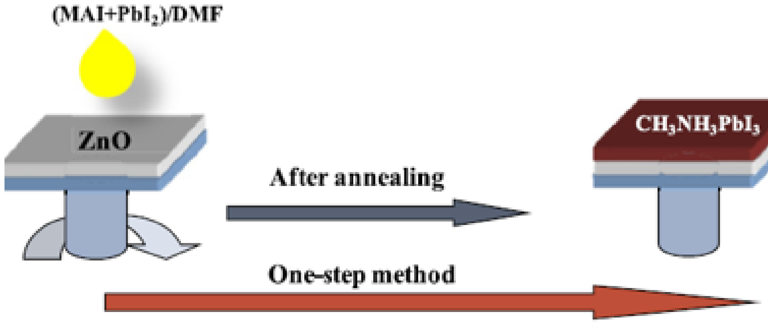

Figure 35: Schematic illustration of a single step deposition technique for lead perovskite thin films (Chaudhary *et al.*, 2020).

Double Step Deposition Method

The double step deposition method was introduced for mesoporous TiO_2 cells which involve the deposition of metal halide through the spin coating and then followed by the immersion into a solution of the organic halide and finally drying for 30 min at 70 °C (Burschka *et al.*, 2013). This method is better than the single-step deposition because the film morphology can be easily controlled and has better pore filling as the metal halide is instantaneously converted to the perovskite (Yantara *et al.*, 2015). The intermolecular exchange process is one of the effective double step deposition approaches where the DMSO can act as a solvent and a reactant for the metal halide at the same time which prevents non-controlled self-assembly crystallization between the metal halide and the organic halide (W. S. Yang *et al.*, 2015). Double step deposition has also presented some limitations like higher cost and additional steps than the single step. However, this method has been able to produce cells with efficiency greater than 20% (Kim *et al.*, 2018; W. S. Yang *et al.*, 2015; Yi *et al.*, 2016). Fig. 36 illustrates how the double step deposition method is carried out.

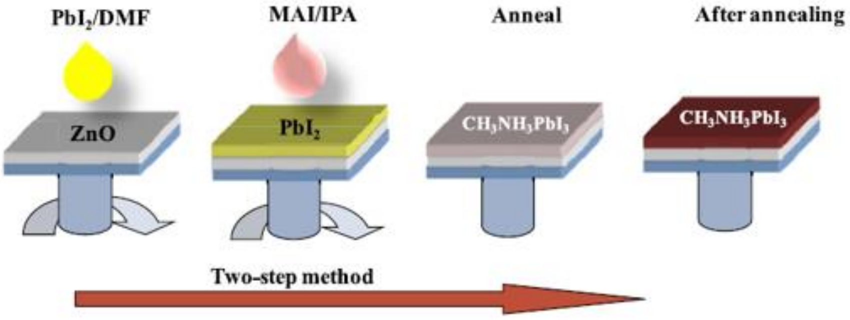

Figure 36: Schematic illustration of a double step deposition technique for lead perovskite thin films (Chaudhary *et al.*, 2020).

Advanced Three-step Method

The three-step advanced method (Fig. 37) was developed by Okamoto and co-workers after finding out that the organic halide PSCs prepared by the two-step method contains unreacted metal halide at the interface between the perovskite layer and the ETL (Okamoto *et al.*, 2018). The unreacted metal halide was then resolved by the addition of MAI/FAI through the spin coating on the two-step prepared PSC film. The PCE of the PSCs increased by the optimized addition of the FAI on top of the two-step prepared PSC through spin coating.

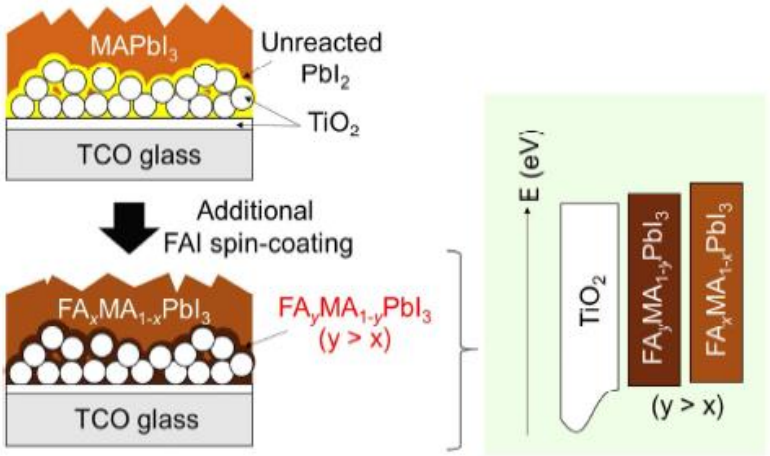

Figure 37: The advanced three-step method using FAI spin coating on a two-step prepared $MAPbI_3$ PSC film to produce a multiple band structure film (Okamoto *et al.*, 2018).

Appendix 5: Characterization of perovskite materials

Perovskite materials requires several equipment in their analysis depending on the specific property of interest. Here is a list of equipment required when characterizing these materials:

X-ray diffraction (XRD)

This is used to examine the crystal structures of the materials using Cu Kα radiation

Ultraviolet visible (UV-vis) spectrophotometer

The materials' absorption properties are evaluated using the UV-vis spectrophotometer to test the light absorption ability.

Fourier transform infrared (FTIR)

The material's spectra are collected with the FTIR to confirm the functional groups' existence due to engineering (doping).

Scanning electron microscopy (SEM)

Scanning electron microscopy equipped with energy-dispersive X-rays (EDX) and a focused ion beam SEM is used to assess the morphology and structure of the particles.

Transmission Electron Microscopy (TEM)

The crystal structure, stoichiometry, and size of perovskite particles can all be investigated using various transmission electron microscopy techniques. A Philips CM300 UT with a 300 kV acceleration voltage can be used to perform selected area electron diffraction (SAED).

Atomic force microscopy (AFM)

The data is acquired by using a mechanical probe to "feel" the surface. The scanning is made possible by piezoelectric devices, which permit tiny but exact and precise movements on (electronic) command. Electric potentials can also be scanned using conducting cantilevers, and currents can be sent through the tip to investigate the underlying surface's electrical conductivity or transport. According to Hooke's law, when the tip comes into contact with a sample surface, forces between the tip and the sample cause the cantilever to deflect. Mechanical contact force, van der Waals forces, capillary forces, chemical bonding, electrostatic forces, magnetic forces, Casimir forces, solvation forces, and other forces are measured in AFM depending on the scenario.

Electrochemical impedance spectroscopy (EIS)

Electrochemical impedance spectroscopy is used in the dark with frequencies ranging from 20 mHz to 200 kHz, a bias of 0 V, and a 20 mV amplitude.

Brunauer-Emmett-Teller (BET)

Nitrogen adsorption-desorption experiments based on Brunauer-Emmett-Teller (BET) theory, is performed on the Micromeritics ASAP 2020 device, to reveal the materials' specific surface area.

Solar simulator

To replicate solar irradiation, a sun simulator (Polaromix K201, Solar simulator LAB 50, McScience K3000) with an intensity of 100 mW cm^2 can be employed.

Appendix 6: Step by step computation of the materials properties using QE

1. Collection of crystallographic information (CIF) files from online database if available.
2. Preparation of the input files: opt.in, scf.in, band.in, bands.in, pw.in.
3. Optimization of the system by minimizing the energy, forces and pressure using the pw.x code.

Command: pw.x –in input file > output file.

4. Self-consistency calculation using the optimized coordinates to generate the charge density.

Command: pw.x –in scf.in > scf.out.

5. Computation of the band structure.

Command: pw.x –in band.in > band.out.

6. Extraction of the bands using the code bands.x.

Command: bands.x –in bands.in > bands.out.

7. Computation of the projected density of states using the code projwfc.x.

Command: projwfc.x –in pw.in > pw.out.

8. Extraction of the states (s, p, d, .) contribution from the total projected density of states using the code sumpdos.x.

Command: sumpdos.x –in pdos.dat.pdos_atm#

For example for Sn the contribution of s, p and d states are summed as:

```
sumpdos.x –in pdos.dat.pdos_atm#1\(Sn\)_wfc#1\(s\) dos.dat.pdos_atm#2\(Sn\)_wfc#1\(s\) pdos.dat.pdos_atm#3\(Sn\)_wfc#1\(s\) dos.dat.pdos _atm#4\(Sn\)_wfc#1\(s\) > Sn1s
sumpdos.x –in pdos.dat.pdos_atm#1\(Sn\)_wfc#2\(p\) pdos.dat.pdos_atm#2\(Sn\)_ wfc#2 \(p\) pdos.dat.pdos_atm#3\(Sn\)_wfc#2\(p\) pdos.dat.pdos_atm#4\(Sn\)_wfc#2\(p\) > Sn2p
sumpdos.x –in pdos.dat.pdos_atm#1\(Sn\)_wfc#3\(d\) pdos.dat.pdos_atm#2\(Sn\)_wfc#3 \(d\) pdos.dat.pdos_atm#3\(Sn\)_wfc#3\(d\) pdos.dat.pdos_atm#4\(Sn\)_wfc#3\(d\) > Sn3d
```

9. Calculation of the thermodynamic properties follows the decomposition routes listed for each system reported in this dissertation. The energies of the reacting species is obtained following step 1, 2 and 3 above and the enthalpy of reaction is calculated. After obtaining the reaction enthalpy, the enthalpy of formation of the perovskite can be calculated.

RESEARCH OUTPUTS

(i) Journal papers

Paschal, C., Pogrebnoi, A., Pogrebnaya, T., & Seriani, N. (2020). Methylammonium tin iodide perovskite: structural, electronic and thermodynamic properties by a DFT study with different exchange–correlation functionals. SN Applied Sciences, 2(4), 1-9.

Paschal, C., Pogrebnoi, A., & Pogrebnaya, T. (2021). Guanidinium tin halide perovskites: structural, electronic, and thermodynamic properties by quantum chemical study. Applied Physics A, 127(5), 1-12.

(ii) Poster presentation

Methylammonium Tin Iodide Perovskite: Structural, Electronic and Thermodynamic Properties by a DFT Study with Different Exchange Correlation Functionals